A Flame Sheet Model of Combustion and NO Formation in Diesel Engines

by

Omowoleola C. Akinyemi

B.Sc., Obafemi Awolowo University, Nigeria, 1989
S.M., Massachusetts Institute of Technology, 1993

Submitted to the Department of Mechanical Engineering
in partial fulfillment of the requirements for the degree of

Doctor of Science

at the

MASSACHUSETTS INSTITUTE OF TECHNOLOGY

June 1997

Author .....
Department of Mechanical Engineering
March 15th, 1997

Certified by .....
Professor John B. Heywood
Department of Mechanical Engineering
Thesis Supervisor

Certified by .....
Professor Wai K. Cheng
Department of Mechanical Engineering
Thesis Supervisor

Accepted by .....
Professor Ain A. Sonin
Chairman, Department Graduate Committee

(This page left intentionally blank)

A Flame Sheet Model of Combustion and NO Formation in Diesel Engines

by

Omowoleola C. Akinyemi

Submitted to the Department of Mechanical Engineering
on March 15th, 1997, in partial fulfillment of the
requirements for the degree of
Doctor of Science

Abstract

Whereas multidimensional modeling of diesel engine combustion provides information on the overall progress of combustion at length scales of the chosen grid spacing, certain important processes occurring on smaller scales cannot be resolved. In particular, subgrid non-uniformities in temperature could result as fuel and air are consumed on a molecular mixing scale much smaller than the computational cell size. A significant consequence of this is that the modeling of NO formation rates based on the cell averaged temperature could significantly underestimate the production.

A flame sheet model was developed in this study to capture the effects of the local elevated temperatures associated with fuel/air combustion on NO formation rates in diesel combustion. The model provides information on the temperature and species profiles within the flame sheet so that the production rates of NO in the flame sheet could be determined. This methodology also enables the decoupling of the modeling of chemistry from that of the mixing and flow processes via an appropriate library of species consumption and formation rates. The library is pre-compiled off-line from the multidimensional computation.

The flame sheet submodel was incorporated into an existing multidimensional computer program (the KIVAII code). The model performance was evaluated in comparison to experimental data obtained from a commercial engine. Comparisons were made of the model predictions of the progress of combustion and the exhaust concentrations of NO and the experimentally determined values. NO formation rates in the flame sheet were found to have an order of magnitude improvement over those resulting from using the cell averaged temperature and species concentrations alone. Thus, significantly better agreement between experiment and model results of NO concentrations was obtained with the added consideration of flame sheet contributions.

Thesis Supervisors: Professors John B. Heywood and Wai K. Cheng

Department of Mechanical Engineering

Contents

1 INTRODUCTION **11**

1.1 Preface 11

1.2 Modeling of Diesel Engine Combustion. 13

1.2.1 Diesel engine combustion processes 13

1.2.2 Models of the diesel combustion process 14

1.3 Scope of This Thesis 15

2 THE FLAME SHEET MODEL **20**

2.1 The Physical Model 21

2.1.1 Validity of the model 22

2.2 The Mathematical Model 25

2.2.1 The NO_x Model 28

2.2.2 Reference quantities 31

2.3 The Numerical Algorithm 31

2.4 Flame Sheet Results 35

3 DEVELOPMENT OF THE FLAME SHEET LIBRARY **42**

3.1 Variation of Burning Rate with Input Parameters 43

3.2 Variation of Excess NO Formation Rate with Input Parameters . . . 46

3.3 Flame Sheet Library 52

3.3.1 Characterization of fuel consumption rate. 52

3.3.2 Characterization of excess NO formation rate 54

4 IMPLEMENTATION AND TESTING OF THE FLAME SHEET LIBRARY **65**

4.1 Evaluation of the Flame Sheet Model 68

4.1.1 Experimental results and engine specifications 68

4.1.2 Modeling results 69

5 PARAMETRIC SIMULATIONS **82**

5.1 Effect of Parametric Variations on NO Formation 83

5.2 Comparison of Experimental And Computed NO Exhaust Concentrations 90

5.3 Possible Routes of Additional NO Formation 93

6 CONCLUSIONS **97**

A Determination of gas properties **100**

B Source Code Listing of the Flame Sheet Model **103**

List of Figures

1-1 Modeling Approach 17

2-1 The Flame Sheet Model 21
2-2 NO_x Modeling with the Flame Sheet Approach 29
2-3 Flowchart of Algorithm used in Computing Flame Sheet Structure . . 32
2-4 Example of Results of Flame Sheet Calculations 36
2-5 Convergence History of Sample Case 38
2-6 Investigation of Grid Dependency of Flame Sheet Calculations 40
2-7 Profiles of NO_{ex} Mole Fraction and Formation Rate 41

3-1 Variation of Burning Rate with Species Mass Fraction 44
3-2 Variation of Burning Rate with Temperature and Pressure 45
3-3 Variation of Burning Rate with Strain 46
3-4 Variation of NO_{ex} Formation Rate with Species Mass Fractions . . . 48
3-5 Variation of NO_{ex} Formation Rate with Temperature and Pressure . 50
3-6 Variation of NO_{ex} Formation Rate with Strain And Background NO 51
3-7 Comparison of Values of Fuel Consumption Rate Obtained From Burn-rate Fit and Individual Flame Sheet Calculations 55
3-8 Comparison of Values of Excess NO Forward Rate Obtained From the Forward Rate Fit and Individual Flame Sheet Calculations 57
3-9 Backward Excess NO Formation Rates vs Forward Rates 58
3-10 Comparison of Values of Excess NO Backward Rate Obtained From the Backward Rate Fit and Individual Flame Sheet Calculations . . 61

3-11 Comparison of Values of Excess NO Concentration Obtained From Flame Sheet NO Fit and Individual Flame Sheet Calculations 62
3-12 Comparison of Values of Flame Temperature Obtained From the Flame Temperature Fit and Individual Flame Sheet Calculations 64

4-1 Illustration of the Modeling of Combustion with the Finite Difference Approach 66
4-2 Summary of the Models that Constitute the Flame Sheet Library . . 67
4-3 The N14 Engine Piston Silhouette 70
4-4 Computational Grid Used in Modeling the N14 Engine 70
4-5 A comparison of Kiva and Experimental Results for the Base Case . . 72
4-6 Fuel Spray and Contours of Fuel Mass Fraction at Different Crank Angles for the Base Case 74
4-7 Velocity Vectors -Base Case 75
4-8 Contours of Flame Sheet Density (cm^{-1}) for different crank angles. -Base Case 76
4-9 Contours of Temperature for different crank angles. -Base Case . . . 78
4-10 Contours of Excess NO production rate ($mol/cm^3/sec$). -Base Case . 79
4-11 Contours of Bulk NO production rate ($mol/cm^3/sec$). -Base Case . . 80
4-12 Contours of Excess NO mole fraction (ppm). -Base Case 81

5-1 A comparison of Kiva and Experimental Results for Run2 84
5-2 A comparison of Kiva and Experimental Results for Run3 85
5-3 A comparison of Kiva and Experimental Results for Run4 86
5-4 Fuel Mass Fraction, Temperature and Excess NO mole fraction contours at a crank angle of 23.4 degrees -Run2. 87
5-5 Fuel Mass Fraction, Temperature and Excess NO mole fraction contours at a crank angle of 25.6 degrees -Run3. 88
5-6 Fuel Mass Fraction, Temperature and Excess NO mole fraction contours at a crank angle of 23 degrees -Run4. 89
5-7 Predicted vs Experimental Values of Exhaust NO Concentration . . . 91

5-8 Variation of Exhaust NO Concentrations with Parameter Variations . 92
5-9 Relative Contribution of Prompt NO Mechanism 94
5-10 Histogram of the Number of Computational Cells Having Different Product Species Mass Fractions for Different Crank Angle Degrees . . 96

List of Tables

3.1 Range of Inputs Used in the Determination of the Fuel Consumption and NO Formation Rates 42

3.2 Fuel Consumption Rate Coefficients 53

3.3 R^+ Coefficients 56

3.4 R^- Coefficients 59

3.5 Excess NO Concentration Coefficients 60

3.6 Flame Temperature Coefficients 63

4.1 Specifications of the Cummins N14 Engine 68

4.2 Operating Conditions 69

5.1 Operating Conditions of N14 Engine Experimental Data 82

5.2 Ratio of Predicted and Experimental Values of Exhaust NO concentration; Using (1)Cell Averaged Values Only and (2) Adding the Flame Sheet Contributions 91

Chapter 1

INTRODUCTION

1.1 Preface

Human health and environmental considerations have made the development of cleaner burning and more efficient diesel engines a continuous challenge facing the transportation industry. Significant improvements have been made in this regard in recent years. Examples are the reduction of pollutant emission levels by the use of ultra-high injection pressure fuel sprays and an appropriate strategy in injection timing. However, as emission standards grow increasingly stringent, the performance requirements of new engines will pose more of a challenge to the design engineer. To achieve the required goals, there will continue to be a growing need for information about the processes that occur during engine combustion and the effect of engine design and operation characteristics on these processes.

Of the emissions from diesel engines, the oxides of nitrogen are of significant concern because of their adverse effects on human health. Elevated concentrations of NO_x in the atmosphere results in acid rain. Also, the reaction of NO_x and unburned hydrocarbons leads to the formation of photochemical smog, while the photolysis of NO_2 yields tropospheric ozone which is a lung irritant.

The scope of engine characteristics that have the potential to significantly affect emission levels of NO_x is wide and varied. This is because of the many complex physical and chemical processes that participate and interact during the combustion

process. This makes the task of collating the necessary emissions data useful in engine development a daunting one. In addition to this, the challenge grows with the introduction of new technologies, which typically introduce new variables, whose effects on emissions need to be explored and quantified.

A significant difficulty in assessing the effect of engine variables on emissions is that typically, only the engine out emissions are measured. The details of the combustion process is lacking and the impact of the engine variables on the fundamental emission formation process cannot be deduced easily from the data. This consideration make computational models an attractive tool for the study of engine combustion. "Computational experiments" are generally easier and cheaper to perform than physical experiments. Also, they lend themselves to a greater range of versatility, even allowing for the testing of configurations and operating conditions that can not be accommodated in physical systems. Engine simulations allow for the quick testing and evaluation of new ideas, which could significantly aid the design process as the investment cost for each "experiment" is considerably reduced. In addition to these, while accessibility for the procurement of data in physical systems can be severely limited, there is virtually no limit in the computational system; all system variables can be accessed and measured by the experimenter at any time.

The difficulty in the use of computational models in the manner described above lies in their limited capacity to correctly predict the phenomena of interest over a wide range of operating conditions. Several computational models with varying levels of complexity have been developed and evaluated by different investigators[1][2][3][4]. While results from these investigations have shown varying degrees of success, there is a general consensus that computational models cannot as yet, be used as a tool for predicting engine performance. These models are essentially mathematical representations of the physical processes as they are understood to occur. Hence they are limited by the adequacy of the understanding of the physical processes.

A challenge thus lies in the development of computational models as a useful tool in the development of engines. Existing models have to be refined continually as more insight into the combustion process is developed. The models have to be evaluated to

assess their capacity to represent the fundamental processes and their departures from the real system should be investigated. Information derived from these investigations should in turn drive the development of better models that will evince the desired behavior and have a better capacity to predict phenomena. And finally, the bounds of reliability of the models developed in representing the evolution of variables for different engine operating parameters have to be established.

1.2 Modeling of Diesel Engine Combustion.

1.2.1 Diesel engine combustion processes

Diesel engine combustion involves a number of complex processes. A good overview of the diesel combustion process is provided by Lyn[5] and also by Heywood[6]. Kamimoto and Kobayashi[7] have also presented a review of some investigations which have provided information about the details of the several subprocesses involved in diesel combustion.

The diesel combustion process starts with the injection of fuel in the liquid phase into the engine cylinder. The liquid jets subsequently experience breakup, vaporization and mixing with the compressed air prior to the commencement of combustion. Chemical reactions are initiated as the fuel and air mix on a molecular level. The progress of these reactions is initially slow, but accelerates rapidly as reactive radicals multiply (ignition). Initially, combustion is limited to that portion of the fuel that was injected at earlier times and has had sufficient time to mix with the air to appropriate proportions on a molecular scale. This is called the "premixed portion" of the fuel. In this premixed portion, ignition occurs as local radical concentrations reach threshold values, and the charge is consumed by a combined process of homogeneous reaction and premixed flame propagation. The rest of the fuel, usually the larger portion, subsequently burns in a diffusion flame as fuel bearing and oxidant bearing eddies dissipate and mix on a molecular scale.

1.2.2 Models of the diesel combustion process

Several methods of characterizing the above processes are used in practice. There are thermodynamic models on one hand and fluid dynamic models on the other. Thermodynamic models are a broad categorization of those models in which the governing equations are based on energy and mass conservation principles; they are augmented by mathematical descriptions of different phenomena which are thought to contribute significantly to the objective of the study -and are hence referred to as phenomenological models. Ikegami and Shioji[4], for example, used a stochastic mixing model to account for non-uniformities in the charge in modeling DI diesel engine combustion. Mansouri and Heywood[1] employed a similar approach but applied their model to describe the full cycle processes in a divided-chamber diesel engine. Kamimoto etal[8] used experimental results to develop phenomenological models of air entrainment, mixing and combustion. They also used a pdf method to characterize the unmixedness of the fuel and air in the charge. As a final example, Xiaoping etal[2] in their study developed a multi-zone combustion model. In their formulation, the fuel spray was divided into several zones which were each homogeneous in temperature and fuel-air concentrations. Conservation laws were then used to predict the progress of combustion and evolution of soot in each zone. An important deficiency in these models, however is their inability to implement the effects of combustion character and injection geometry on combustion in a general way.

Fluid dynamic (or multidimensional) models have the added desirability (and complexity) in that the law of conservation of momentum is also considered in the modeling process. The general approach is the discretization of the conservation equations and the solution of those equations over a suitable difference grid. More elementary processes are used in the modeling process and hence this approach is more rigorous and is better suited than thermodynamic models for fundamental investigations. Several investigations of the combustion process and the evolution of NO_x and soot have been performed with the use of these models[9]. Reitz and Rutland[10] have given a review of the state of the art of the multidimensional models used in

diesel engine combustion modeling, chronicling significant improvements that have been achieved in recent years. There still remains, room for improvement to make these models truly predictive in nature. Existing multidimensional models are not entirely fundamental in their formulations because some of the subprocesses are too complex to be described in detail. For such subprocesses, recourse is made to phenomenological models which are incorporated as submodels in the multidimensional model. Thus, submodels have been used to describe the break up of liquid droplets, ignition delay and to characterize turbulent flow in the cylinder. These submodels, make the modeling task possible but are also a limitation to the predictive capacity of these codes. And the improvement of multidimensional models lies in the refinement of these submodels to more accurately describe the physical processes that they are intended to model. Reviews and evaluations of some of the submodels that are used in the KIVA code which is itself a state of the art multidimensional model have been performed by Gonzales et al[11] and Rutland et al[12].

1.3 Scope of This Thesis

This thesis is a record of the results of an investigation into the fundamentals of combustion and NO_x formation in diesel engines. The goals of this study included the formulation of a submodel of combustion and NO_x formation in diesel engines for use with the KIVAII code and the validation of this model. It was intended that with this model, explanations could be given for observed trends in the effect of turbulent mixing on the rate of progress of chemistry in diesel engines, with particular attention being paid to NO_x formation and destruction. This would in turn help to relate NO_x formation rates to engine characteristics and operating parameters.

To this end, a flame sheet model of combustion and NO_x formation in diesel flames was used. The flame sheet model[13][14] was originally developed for diffusion flames of high Damkohler number, and is based on the consideration that chemical reactions occur in flames sheets located at the interfaces of fuel and air eddies. If the thickness of the flame sheet is much smaller than the average eddy size, it can

be further assumed that the action of turbulence on the flame structure results in the distortion, stretching and convection of these sheets only, and that the coherent structure of the flame sheet is maintained. Turbulent flames can thus be analyzed as an ensemble of strained laminar diffusion flamelets, and the progress of reaction can be described locally by an accounting of the effective flame surface area and the local rate of consumption of species per unit flame surface area. Details of the flame sheet model are presented in Chapter 2. Examples of computations performed using the flame sheet model are presented by Cheng[15], Dillies etal[16], and Veynante et al[17]. A review of the different regimes of applicability of the flame sheet model is also presented by Bilger[18].

The flame sheet model was used as the combustion submodel in KIVAII in order to provide a means of including the effects of non-uniformities within each computational cell in the modeling of NO_x formation and destruction rates. In multidimensional computations, cell properties are averaged over the cell in the solution of the discretized equations, and cell non-uniformities are unaccounted for. NO_x formation rates are, however, highly sensitive to temperature; increasing by an order of magnitude for every 200K increase in temperature above the 1800K threshold. Thus, the effect of local extrema of temperature within a computational cell with the progress of combustion in the cell could be significant. One objective of this investigation was to quantify the relative contribution of such subgrid nonuniformities to the overall NO_x emission levels. Modeling of NO_x formation in engines using multidimensional codes have typically shown results that are significantly smaller than those experimentally obtained[19]. Some investigators have, hence, applied a mulitiplicative factor to improve agreement. Some others have been able to show improved agreement with the use of the RNG k-ϵ model with which sharper gradients in the temperature field were obtained[10]. However, in all these calculations, subgrid effects were not taken into consideration and the question of their relative contributions still remains unanswered.

The flame sheet combustion submodel is completed by a model of the evolution of the flame surface area density which is computed with other scalar variables in the multidimensional model. Figure 1-1 illustrates this modeling approach. As can be

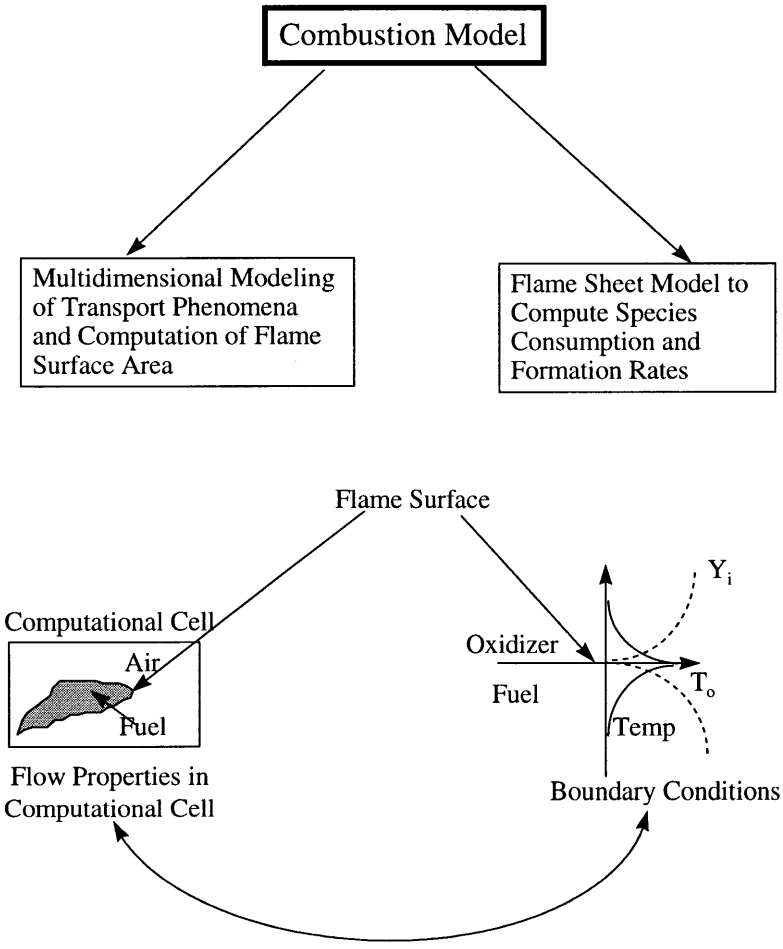

Figure 1-1: Modeling Approach

seen in this figure, the flame sheet model provides species consumption and formation rates per unit flame surface area for different boundary conditions. A relationship is determined between these boundary conditions and the flow properties in the computational cell of the multidimensional model. The coupling between the multidimensional model and the flame sheet model is completed by the local values of the flame surface area per unit volume. This modeling approach has the added advantage of allowing for a separation of the modeling of chemistry from the modeling of transport and flow phenomena. Thus, species consumption rates could be determined apriori for different values of pertinent flow properties and stored as a library to be used in the multidimensional model.

The flame sheet model as described above was developed as part of this investigation. The flame sheet structure in diesel flames was analyzed for different values of several flow variables. The data collated was then used to formulate a model of combustion and NO_x formation in diesel engines which included the effect of the elevated temperatures associated with the presence of the flame sheet, thus capturing the desired subgrid effects. This model was subsequently incorporated into the KIVAII code as a combustion submodel. An evaluation of the model was then performed to assess the benefits of the combustion submodel. The results of computations were compared to experimentally obtained engine-out data. Particular attention was paid to the contribution of cell property non-uniformities to the evolution of NO_x in the charge. The results of these computations, thus, helped to elucidate the significance of flame sheet contributions to overall NO_x formation rates.

Parametric numerical experiments were performed with the augmented version of the KIVAII code. These simulations were compared with data provided by the Cummins engine company. The data included NO_x measurements from an engine at different operating conditions of the engine. The KIVAII code was used to simulate the combustion process for these operating conditions in this engine. The results of the computations are compared to the experimental data in the body of this thesis. Points of departure of the combustion submodel from the physical system are highlighted and discussed. Also, the observed trends in NO_x emissions are analyzed in the light

of the results obtained from the multidimensional computations.

Chapter 2

THE FLAME SHEET MODEL

The combustion of fuel in diesel engines is largely controlled by the mixing of fuel and air species on a macroscopic level. Exceptions to this are the ignition and premixed combustion phases, during which the kinetics of the chemical reactions involved could have time scales equal to or greater than those associated with the mixing process. Edwards and co-workers[20] have presented photographic and pressure data that describe the ignition and combustion process in a constant volume chamber. Dillies et al[16], in discussing these results, have suggested that Damköhler numbers of the order of unity obtain during ignition, while Damköhler numbers are much greater than this at subsequent times.

Such considerations have led researchers to develop mixing-based models to describe the combustion in diesel engines and similar systems. Examples are computations based on the model presented by Magnussen and Hjertager[21]. Flame sheet models have also been used in other computations[22][16]. The flame sheet model allows for a complete decoupling of the modeling of the formation and destruction of species from the modeling of the flow and mixing processes. Thus, a more complete description of the physics of species formation and destruction can be included in its formulation. The drawback in computations performed with the use of the flame sheet model till date, however, is that a complete description of the structure of the flame sheet in diesel flames was not employed in that the effect of the flame sheet on the rates of formation and destruction of secondary species (for example NO_x) was

not taken into consideration. Also, constant species properties were assumed in their model to facilitate computations. The present formulation attempts to address some of these issues.

2.1 The Physical Model

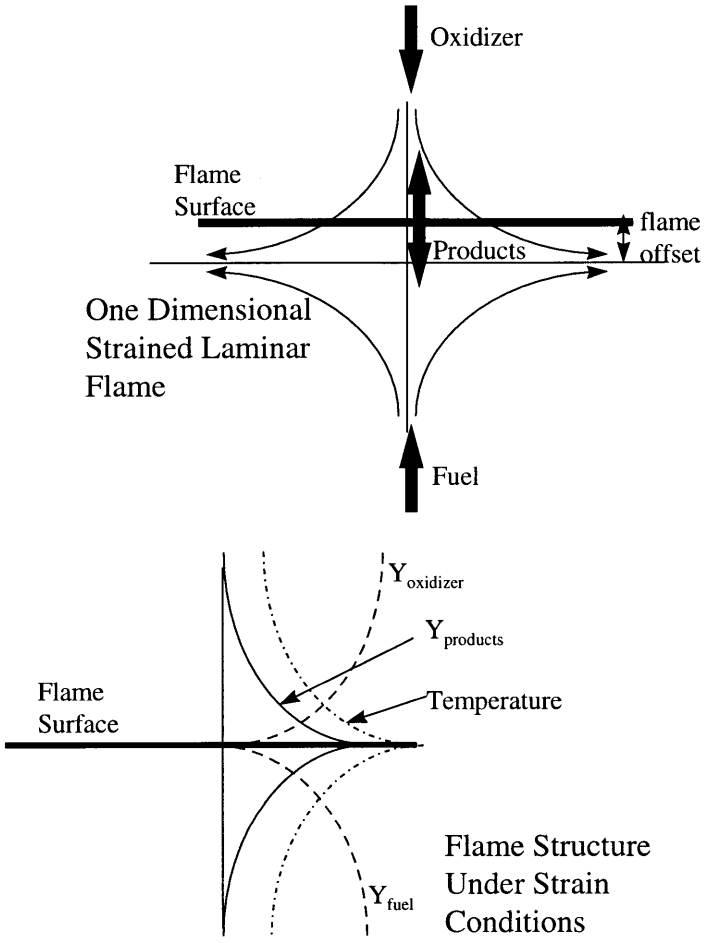

Figure 2-1: The Flame Sheet Model

The flame sheet model is illustrated in Figure 2-1. Based on the assumption of small Damköhler number, it is assumed that chemical reactions are confined to reaction sheets. It is further assumed that these sheets are of negligible thickness compared to length scales associated with the flow and mixing process. Thus, the

action of turbulence on these reaction sheets results in their transport, distortion and stretching; but the reaction sheets keep their original structure during these processes. Combustion rates are obtained by the product of the local rates associated with the flame sheet and the flame sheet surface area. The flame sheet surface area is itself modeled and calculated by conservation laws governing its transport, formation and destruction in the main flow field. These governing equations are discussed in Chapter 4.

Combustion proceeds in the flame sheets as fuel and air species diffuse into the reaction zone. The rate of progress of hydrocarbon oxidation within the sheets is assumed to be infinitely fast as compared to the diffusion process, and the fuel and air species are assumed to be consumed instantaneously to form products as they mix at the reaction surface. This precludes co-existence of fuel and air species at any location and, in particular, requires that the fuel is separated from the air mass by the reaction sheet as shown in the figure.

The flame sheets are kept in steady state by the stretching action of the turbulent eddies. Thus, the rates of generation of heat and product species at the surface of the flame are balanced by their rates of removal by flame stretch. The flame, in steady state, is also offset from the stagnation flow point to allow for stoichiometric diffusion of fuel and air species to the surface of the flame. Hence, the surface of the flame sheet moves in response to variations in the rate of diffusion of species to the flame surface which could result from changes in the mass fractions of air and fuel on either side of the reaction sheet.

2.1.1 Validity of the model

The limits of applicability of this model are as follows. Firstly, an infinite chemical reaction rate is assumed which holds true only when diffusion time scales are much larger than chemical time scales. Conversely then, the model fails when chemical rates of formation are of the same order as (or smaller than) diffusion rates; which could result from excessively high strain rates coupled with very slow reactions. In the main reaction zones of the engine, it is not likely that these conditions will hold, but they

could occur in regions of low temperature or excessive dilution of the reacting species by the products of combustion. In those instances, the flame sheet is extinguished by blow out at high levels of flame stretch.

In addition to the above, there are possibilities of departure from the assumption of steady state conditions when the flame sheet is subjected to rapid variations in strain rate. Such conditions could be realized in turbulent flame environments. Studies have been performed into the response of laminar diffusion flames to oscillating strains of different frequencies and amplitudes[23][24]. The results from these analysis show that for sufficiently slow or fast variations in strain rate, the conditions in the flame sheet are approximately steady at each instance of time. In addition, Ghoniem[24] in his study showed that when oscillatory strains were employed, the cycle averaged burning rate was close to the burning rate obtained using steady strain, provided the strains applied were within the quenching limits of the flame. At higher strain rates, flame extinction could occur. In the light of these results, it is expected that the steady state model will adequately represent flame sheet behavior for strain rates below the extinction limit. The phenomenon of extinction is not as yet incorporated into the model and the flame sheet is not valid in those regimes.

Finally, negligible thickness of the reaction sheet was assumed: that the thickness of the chemical reaction zone is much smaller than the laminar heat and mass transfer length scale in the strained flame. This can be written mathematically as

$$\frac{y'}{\sqrt{Dl'/u'}} \ll 1 \tag{2.1}$$

for an eddy length scale of l' and velocity scale of u'. y' is the reaction zone thickness and D is the laminar diffusivity. Arguments have been presented in a previous study to show that this condition is practical for turbulent combustion systems[15].

To illustrate the length and time scales involved, consider a typical diffusion flame system in a diesel combustion environment at a pressure of 80bar and an ambient temperature of 1000K. Typical values of strain rate e and flame sheet density Σ can be obtained from numerical simulations such as those in reference [10]. In the

combustion zone, the strain rate (e) is of the order of $1000s^{-1}$. The diffusivity D is of the order of $10^{-6}m^2/s$. Thus, the flame thickness is

$$\delta \sim \sqrt{\frac{D}{e}} \sim 30\mu m \tag{2.2}$$

The spacing L between flame sheets is

$$L \sim \frac{1}{\Sigma} \sim 100\mu m \tag{2.3}$$

Thus, the flame sheet occupies approximately 30% of the combustion volume.

Data on the extinction of a diffusion flame by the strain of the turbulent eddies at conditions prevalent during diesel combustion is not available. An estimate may, however, be made by using the values for pre-mixed flames at stoichiometric conditions. The critical strain rate is given by the critical Karlowitz number, K_c:

$$e_c = K_c \left(\frac{S_L}{\delta}\right) \tag{2.4}$$

$$= \left(K_c \frac{S_{Lo}}{\delta_o}\right) \left(\frac{S_L}{S_{Lo}}\right) \left(\frac{\delta_o}{\delta}\right) \quad = e_{c_o} \left(\frac{S_L}{S_{L_o}}\right) \left(\frac{\delta_o}{\delta}\right) \tag{2.5}$$

where e_{c_o} is the critical strain rate at atmospheric conditions which has been measured. Using the scaling[25]

$$S_L = T^{2.8} P^{-0.16} \tag{2.6}$$

and

$$\delta \sim \frac{D}{S_l} \sim \frac{1}{S_l} \frac{T^{1.5}}{P} \tag{2.7}$$

then

$$e_c = e_{c_o} \left(\frac{S_l}{S_{l_o}}\right)^2 \left(\frac{D_o}{D}\right) \tag{2.8}$$

$$= e_{c_o} \left(\frac{T}{T_o}\right)^{2.86} \left(\frac{P}{P_o}\right)^{0.68} \tag{2.9}$$

Using $e_{c_o} \sim 10^3 s^{-1}$ at $300K$ and $1bar$; then at $1000K$ and $60bar$

$$e_c \sim 5 \times 10^5 s^{-1} \tag{2.10}$$

It is unlikely that such a high strain is encountered during the combustion period.

2.2 The Mathematical Model

Refering to Figure 2-1, the governing equations of the one dimensional strained flame are as follows. Assuming the flame sheet surface lies on the x axis, offset from the stagnation flow point by s as shown, the strain rate is defined as

$$e = \frac{\partial u}{\partial x} \tag{2.11}$$

There are no other variations in the x direction. Thus, the continuity equation can be written as

$$\frac{d(\rho v)}{dy} = -\rho e \tag{2.12}$$

which upon integration gives

$$\rho v = -e(z + w) \tag{2.13}$$

z in the above equation is defined as

$$z = \int_0^y \rho dy \tag{2.14}$$

and w is the integration constant $\int_0^s \rho dy$. The species continuity equation can also be written as follows

$$\rho v \frac{dY_i}{dy} = -\frac{dJ_i}{dy}; \quad i = 1, 2 \tag{2.15}$$

where J_i is the mass diffusion flux given by

$$J_i = -\rho D_{i3} \frac{\partial Y_i}{\partial y}. \tag{2.16}$$

D_{i3} is the binary diffusion co-efficient of species i in the product species. The subscripts 1,2 and 3 in the above equations refer to fuel, oxidizer and product species respectively.

The energy conservation equation can also be written in a similar fashion

$$\rho v c_p \frac{dT}{dy} = \frac{d}{dy} \lambda \frac{dT}{dy} - \frac{d}{dy} \left[J_i \left(h_i - h_3 \right) \right] \tag{2.17}$$

where h_i is the sensible enthalpy of species i i.e

$$h_i = \int^T c_{pi} dT \tag{2.18}$$

and c_p is

$$c_p = \left(Y_i c_{pi} + Y_3 c_{p3} \right) \tag{2.19}$$

The differential equations (2.15) and (2.17) along with the auxiliary equations (2.13), (2.16), (2.18) and (2.19) define the laminar strained diffusion flame system completely for subsonic conditions.

These equations can be non-dimensionalized for convenience and to this end, the following set of non-dimensional and reference quantities were defined (reference quantities have the subscript "0"; non-dimensional quantities have the superscript "*"):

$$T = T_0 T^* \tag{2.20}$$

$$y = L_0 y^* \tag{2.21}$$

$$\rho = \rho_0 \rho^* \tag{2.22}$$

$$J_i = \rho_0 L_0 e J_i^* \tag{2.23}$$

$$M = M_0 M^*; \text{ (molecular weight)} \tag{2.24}$$

$$D_{i3} = D_0 D_{i3}^* \tag{2.25}$$

$$\lambda = \lambda_0 \lambda^* \tag{2.26}$$

$$c_p = c_{p0} c_p^* \tag{2.27}$$

$$v = L_0 e v^*; \text{ (velocity)} \tag{2.28}$$

The values picked as reference quantities are discussed later in this chapter. The non-dimensional equations transformed into z co-ordinates can then be written as follows (the superscript * is dropped for convenience)

$$(-z + w) \frac{dY_i}{dz} = -\frac{dJ_i}{dz} \tag{2.29}$$

$$J_i = -\rho^2 D_{i3} \left(\frac{dY_i}{dz} \right) \tag{2.30}$$

$$(-z + w) c_p \frac{dT}{dz} = \Lambda_0 \frac{d}{dz} \left[\rho \lambda \frac{dT}{dz} \right] - \frac{d}{dz} \left[J_i \left(h_i - h_3 \right) \right] \tag{2.31}$$

The term Λ_0 in the non-dimensionalized energy equation (equation (2.31)) is the Lewis number at reference conditions given by the expression

$$\Lambda_0 = \frac{\lambda_0 / (\rho_0 c_{p0})}{D_0} \tag{2.32}$$

and the density is related to the pressure by the non-dimensional form of the ideal gas law

$$\rho = \frac{PM}{T} \tag{2.33}$$

Finally, the boundary conditions of the above equations are as follows. The conditions at infinity are specified viz:

$$T = T(\infty) \quad Y = Y_1(\infty); \quad @z = \infty \tag{2.34}$$

$$T = T(-\infty) \quad Y = Y_2(-\infty); \quad @z = -\infty \tag{2.35}$$

and at the flame surface, the mass fractions of reactant species are required to go to zero giving

$$Y_1(0) = Y_2(0) = 0; \quad @z = 0 \tag{2.36}$$

In addition, the ratio of fuel mass flux to air mass flux at the reaction sheet surface is stoichiometric and the energy release at the flame surface is balanced by the transport of heat from the surface of the flame. This gives two additional conditions at the flame surface which can be expressed as follows

$$J_1(0-) + \phi J_2(0+) = 0 \tag{2.37}$$

$$\left[\rho\lambda\frac{dT}{dz}\right]_-^+ - \frac{1}{\Lambda_0}\left[J_i\left(h_i - h_3\right)\right]_-^+ + HJ_i(0-) = 0 \tag{2.38}$$

where H is the dimensionless heating value related to the lower heating value of diesel fuel (hv) by the expression

$$H = \left(\frac{hv}{c_{p0}T_0}\right)\frac{1}{\Lambda_0} \tag{2.39}$$

2.2.1 The NO_x Model

NO_x is modeled following the Zeldovich mechanism of NO_x formation represented by the following reactions[26][27]

$$O + N_2 = NO + N \tag{2.40}$$

$$N + O_2 = NO + O \tag{2.41}$$

$$N + OH = NO + H \tag{2.42}$$

Assuming the N atom concentration is in steady state, the rate of formation of NO in the above equations can be expressed as[28]

$$\frac{d[NO]}{dt} = 2k_1^+[O][N_2]\frac{1 - [NO]^2/(K[O_2][N_2])}{1 + k_1^-[NO]/(k_2^+[O_2] + k_3^+[OH])} \tag{2.43}$$

where k_1, k_2 and k_3 are rates of reactions (2.40), (2.41) and (2.42). From the solution of equations (2.29), (2.30) and (2.31), the profiles of species mass fractions and temperature for the flame sheet are known. NO formation rates can, hence, be resolved spatially in the flame sheet by solving equation (2.43) as a function of y, thus allowing the effect of the higher temperatures associated with the flame sheet to be captured in the determination of the formation rates. Figure 2-2 shows how this

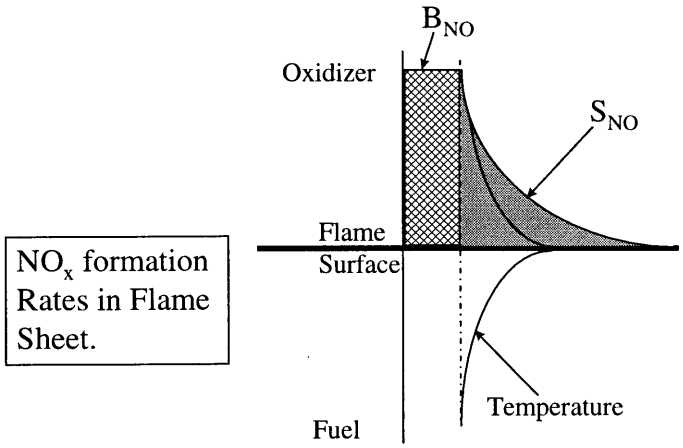

Figure 2-2: NO_x Modeling with the Flame Sheet Approach

was accomplished. First it is noted that NO is generated in the oxidizer portion of the flame sheet alone. The NO generation term associated with the flame sheet can be expressed as

$$NO_{generation} = S_{NO} \sum + B_{NO} \tag{2.44}$$

where B_{NO} represents the rate of NO generation at infinity on the oxidizer side of the flame sheet. $\sum$ is the flame sheet surface area and S_{NO} is the integral in the cross-wise direction of the rate of generation of NO in the flame sheet, over and above B_{NO},

per flame sheet surface area i.e

$$S_{NO} = \int_0^\infty M_{NO} \left[\left(\frac{d[NO]}{dt} \right)_y - \left(\frac{d[NO]}{dt} \right)_\infty \right] dy \tag{2.45}$$

To solve equation (2.45), profiles of the concentration of the radicals O and OH are needed and these were obtained by assuming that the product is in equilibrium at the local temperature $T(y)$. Local levels of NO concentration are also needed to determine the backward rates of the chemical reactions (2.40), (2.41) and (2.42). These were determined by solving the equation of conservation of "excess" NO (NO_{ex}) in the stretched laminar flame defined as the mole fraction of NO formed in the flame sheet over the background concentration. The conservation equation is given by the expression

$$\frac{\partial(\rho Y_{NOex})}{\partial t} + \rho v \frac{\partial Y_{NOex}}{\partial y} = \frac{\partial}{\partial y} \rho D \frac{\partial Y_{NOex}}{\partial y} + \dot{r}_{NOex} \tag{2.46}$$

where $\dot{r}_{NOex}$ is defined as

$$\dot{r}_{NOex} = M_{NO} \left[\left(\frac{d[NO]}{dt} \right)_y - \left(\frac{d[NO]}{dt} \right)_\infty \right] \tag{2.47}$$

Equation (2.46) was also non-dimensionalized and transformed into z co-ordinates. In addition, mass fractions were converted into mole fractions and the resulting expression is

$$\frac{\partial n}{\partial t} - (z - w) \frac{\partial n}{\partial z} = \frac{\partial}{\partial z} \rho^2 D \frac{\partial n}{\partial z} + \frac{\dot{r}^*_{NOex} M}{\rho} \tag{2.48}$$

where n is the mole fraction of NO_{ex} and $\dot{w}^*_{NOex}$ is the non-dimensional formation rate of NO_{ex} related to $\dot{w}_{NOex}$ as follows

$$\dot{r}^*_{NOex} = \frac{\dot{r}_{NOex}}{\rho_0 e} \tag{2.49}$$

The boundary conditions for equation (2.48) are given by

$$n(-\infty) = n(\infty) = 0; \quad @z = \pm\infty \tag{2.50}$$

and the initial condition is

$$n = 0; \quad @t = 0 \tag{2.51}$$

Equation (2.48) was solved in time until steady state conditions were realized. At each time step the NO concentration profile was updated by summing the contributions from the excess and background NO mass fractions and the new NO formation rate was computed. More details of the solution procedure employed are given in section 2.3.

2.2.2 Reference quantities

The flame-sheet model is completed by the choice of reference quantities used in scaling the variables of the system. Reference values of temperature, pressure, density, specific heat and thermal conductivity were chosen to correspond to the property of air at atmospheric conditions. D_0 was set equal to the diffusivity of fuel in products at atmospheric conditions. Dimensions of length were scaled by

$$L_0 = \sqrt{\frac{D_0}{e}} \tag{2.52}$$

and the reference molecular weight was obtained from the expression

$$M_0 = \frac{\rho_0 R T_0}{P_0} \tag{2.53}$$

2.3 The Numerical Algorithm

Salient features of the algorithm used in computing the profiles of species concentration and temperature in the flame sheet are shown in Figure 2-3.

The governing equations were discretized over a uniform one-dimensional grid. The discretized form of the diffusion equation (equation(2.29)) can be written as

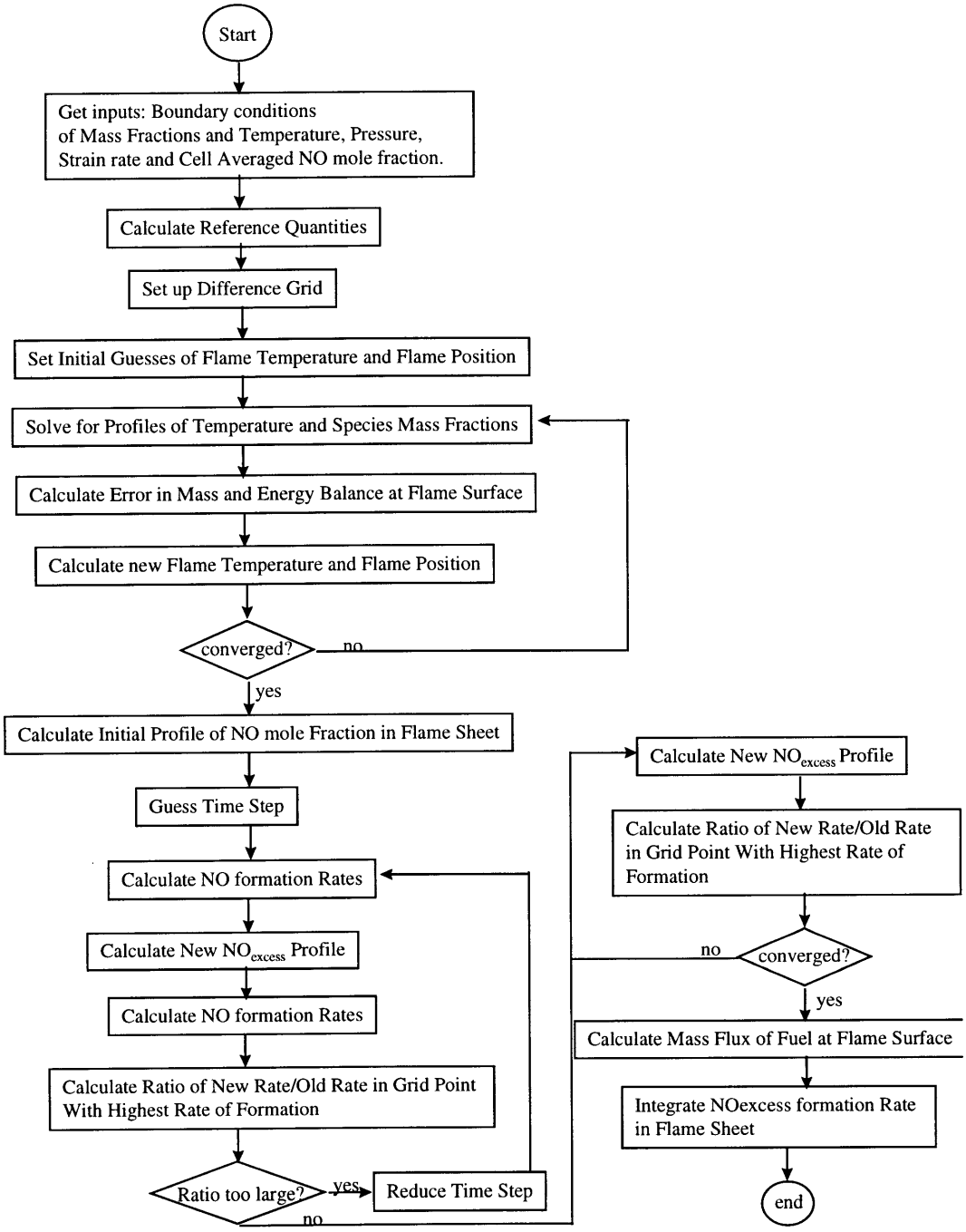

Figure 2-3: Flowchart of Algorithm used in Computing Flame Sheet Structure

follows:

$$\begin{aligned}\delta z(-z^k + w)(Y_i^{k+1} - Y_i^{k-1}) - \left[(\rho^2 D_i)^k + (\rho^2 D_i)^{k+1}\right] Y_i^{k+1} \\ - \left[(\rho^2 D_i)^k + (\rho^2 D_i)^{k-1}\right] Y_i^{k-1} \\ + \left[(\rho^2 D_i)^{k+1} + (\rho^2 D_i)^{k-1} + 2(\rho^2 D_i)^k\right] Y_i^k = 0\end{aligned} \tag{2.54}$$

and the discretized energy equation is

$$\begin{aligned}T^{k+1}\left[c_p^k \delta z(-z^k + w) - \Lambda_0\left[(\rho\lambda)^k + (\rho\lambda)^{k+1}\right]\right] + \\ T^k\left[\Lambda_0\left((\rho\lambda)^{k+1} + 2(\rho\lambda)^k + (\rho\lambda)^{k-1}\right)\right] + \\ T^{k-1}\left[-c_p^k \delta z(-z^k + w) - \Lambda_0\left[(\rho\lambda)^k + (\rho\lambda)^{k-1}\right]\right] + \\ \zeta^{k+1}\left[y^{k+1} - y^k\right] + \zeta^k\left[y^{k+1} - 2y^k + y^{k-1}\right] + \\ \zeta^{k-1}\left[y^{k-1} - y^k\right] = 0\end{aligned} \tag{2.55}$$

where ζ^k is defined as

$$\zeta^k = \left[\rho^2 D_i[h_i - h_3]\right] \tag{2.56}$$

The k superscript in the above equations refers to the grid point. ζ^k and other gas properties were calculated using temperatures obtained in the previous iteration step and hence they are assumed to be known quantities in equations (2.54) and (2.55). This introduces little error in the computation if the solution of the flame sheet asymptotically approaches the converged solution as is expected. The determination of the gas properties used in the solution of the system equations is discussed in Appendix A

The terms in equations (2.54) and (2.55) were rearranged to form a tri-diagonal system of equations and the solution to this was obtained using Thomas algorithm [29]. To begin the calculations, initial profiles of species mass fractions and temperature were created for the determination of properties at each grid point. Guesses of flame temperature(T_0) and flame position(w) were then used to obtain an initial solution to the system equations. This solution was refined in subsequent iterations by

an attempt to choose w and T_0 such that the error in matching the flux conditions at the flame surface was minimized. To this end, the following error matrix was defined

$$E = \begin{pmatrix} J_1(0-) + \phi J_2(0+) \\ \left[\rho\lambda\frac{dT}{dz}\right]_-^+ - \frac{1}{\Lambda_0}\left[J_i(h_1 - h_3)\right]_-^+ + HJ_i(0-) \end{pmatrix} \tag{2.57}$$

and w and T_0 were obtained for the $(n+1)^{\text{th}}$ iteration step according to the following law:

$$\begin{bmatrix} w \\ T_0 \end{bmatrix}^{n+1} = \begin{bmatrix} w \\ T_0 \end{bmatrix}^{n} - \left[\frac{\partial E}{\partial(w, T_0)}\right]^{-1} (E)^n \tag{2.58}$$

Calculating the partial derivative of the error matrix with respect to w and T_0 respectively in equation(2.58) requires evaluation of the variation in E with one variable while the other remains constant. This was performed by solving the system equations at each iteration step with three sets of values of flame position and flame temperature: $(w^n, {T_0}^n)$, $(w^{n-1}, {T_0}^n)$ and $(w^n, {T_0}^{n-1})$. The derivative of the error term with respect to each variable was then calculated by backward difference; for example,

$$\frac{\partial E_1}{\partial w} = \frac{E_1(w^n) - E_1(w^{n-1})}{w^n - w^{n-1}} \tag{2.59}$$

The second part of the flame sheet calculations involves the determination of NO formation rates in the flame sheet. Equation(2.48) was discretized to give the following expression (the superscript is the time step while the subscript refers to the grid point):

$$\begin{aligned} &(2\delta z^2)(n_k^{t+1} - n_k^t) + (-z_k + w)(n_{k+1}^{t+1} - n_{k-1}^{t+1})\delta z\,\delta t = \\ &\quad \delta t\left[\left((\rho^2 D)_{k+1} + (\rho^2 D)_k\right) n_{k+1}^{n+1} + \right. \\ &\quad \left((\rho^2 D)_{k+1} + 2(\rho^2 D)_k + (\rho^2 D)_{k-1}\right) n_k + \\ &\quad \left.\left((\rho^2 D)_k + (\rho^2 D)_{k-1}\right) n_{k-1}^{n+1}\right] + \frac{\dot{r}^* M}{\rho}(2\delta z^2)\delta t \end{aligned} \tag{2.60}$$

Again, Thomas algorithm was used to obtain the profile at each time step. The initial

time step δt_i was chosen so that

$$\frac{\dot{r}_{hi}^{t+1} - \dot{r}_{hi}^{t}}{\dot{r}_{hi}^{t}} < \theta \tag{2.61}$$

where the subscript hi refers to the grid point with the highest rates of formation. A value of θ of about 0.8 was found to give good stability characteristics for the cases that were run.

Time stepping was performed using Jameson's method[30] and at each time step, the formation rates of NO were updated. The time step was controlled by evaluating the stability law expressed in equation(2.61) and applying necessary adjustments to the time step. This allowed larger time steps to be used as the solution approached steady state thus speeding up the calculation process.

As the objective of the calculations was the determination of NO formation rates, the calculations were terminated after unappreciable changes in formation rates occurred from one time step to the next. The formation rates were then integrated with respect to z to yield S_{NO} (equation(2.44)) using Simpson's rule.

2.4 Flame Sheet Results

Typical results of flame sheet computations are shown in Figure 2-4 in which the profiles of temperature and species mass fractions are plotted against the non-dimensional variable z. The boundary conditions for this case were as follows:

ambient temperature:	$1600K$
fuel mass fraction:	0.353
air mass fraction:	0.522
strain:	$1000s^{-1}$
pressure:	100 atm
background NO:	2000ppm

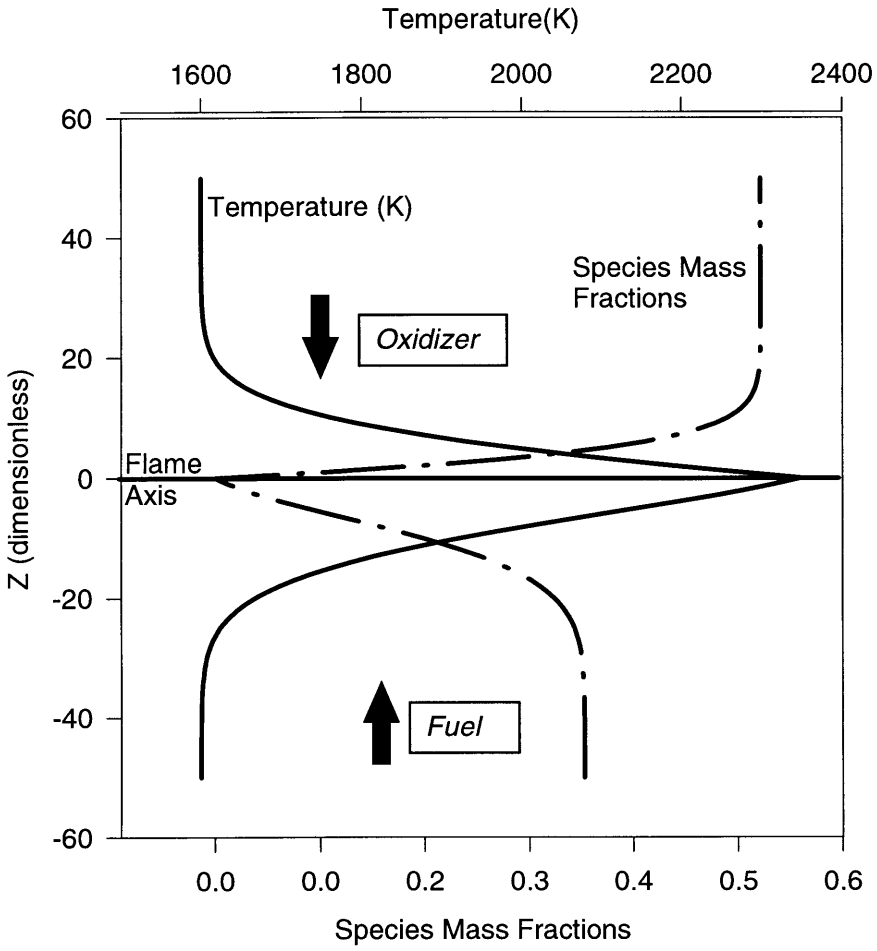

Figure 2-4: Example of Results of Flame Sheet Calculations

In the figure, the fuel side of the flame is the negative z portion of the plot while the oxidizer is on the positive side. It should be borne in mind that z is a density weighted spatial dimension. Thus, values of z on the fuel side represent smaller distances than corresponding values on the oxidizer side of the flame since the molecular weight of the fuel species is higher than the molecular weight of air. At convergence of the system equations, the profile of the mass fraction of air typically has a significantly sharper gradient than that of the fuel mass fraction because of the high fuel to air mass diffusion ratio at the reaction surface.

The computed flame temperature for the case shown is $2348K$; approximately $730K$ higher than the ambient conditions. The flame temperature is dependent on the fuel consumption rate at the surface of the flame which is itself a function of the rates of mass transport to the flame surface by stretch and also of the local concentration of fuel in the vicinity of the flame. The species mass fractions decrease in the same plot from their boundary values to zero at the flame surface. The diffusion thickness of the flame is about 40 non-dimensional units of z which corresponds approximately to a distance of 200μm.

Values of the error matrix (E), flame position and non-dimensional flame temperature are plotted against the iteration number in Figure 2-5. w converges to a value of -8.96 in this case. The flame offset position is a function both of the stoichiometric fuel to air ratio and the mass ratio of fuel and air in the flame sheet system. Both values of E_1 and E_2 (corresponding to the continuity and energy equations respectively) are less than 1×10^{-5} at convergence. The strong coupling between the energy and continuity equations does not allow for a strictly monotonic decrease in the error values; nevertheless, as can be seen in the plot, the system is relatively well behaved and reaches convergence in less than 30 iterations.

Issues that needed to be addressed in performing these calculations include the domain size and grid spacing. To improve accuracy, it is necessary that the solution domain is larger than the diffusion length scales of the flame so that variables approach their boundary values with zero gradient. A domain of $-50 < z < 50$ was found to satisfy this criterion for the reference quantities and range of input conditions

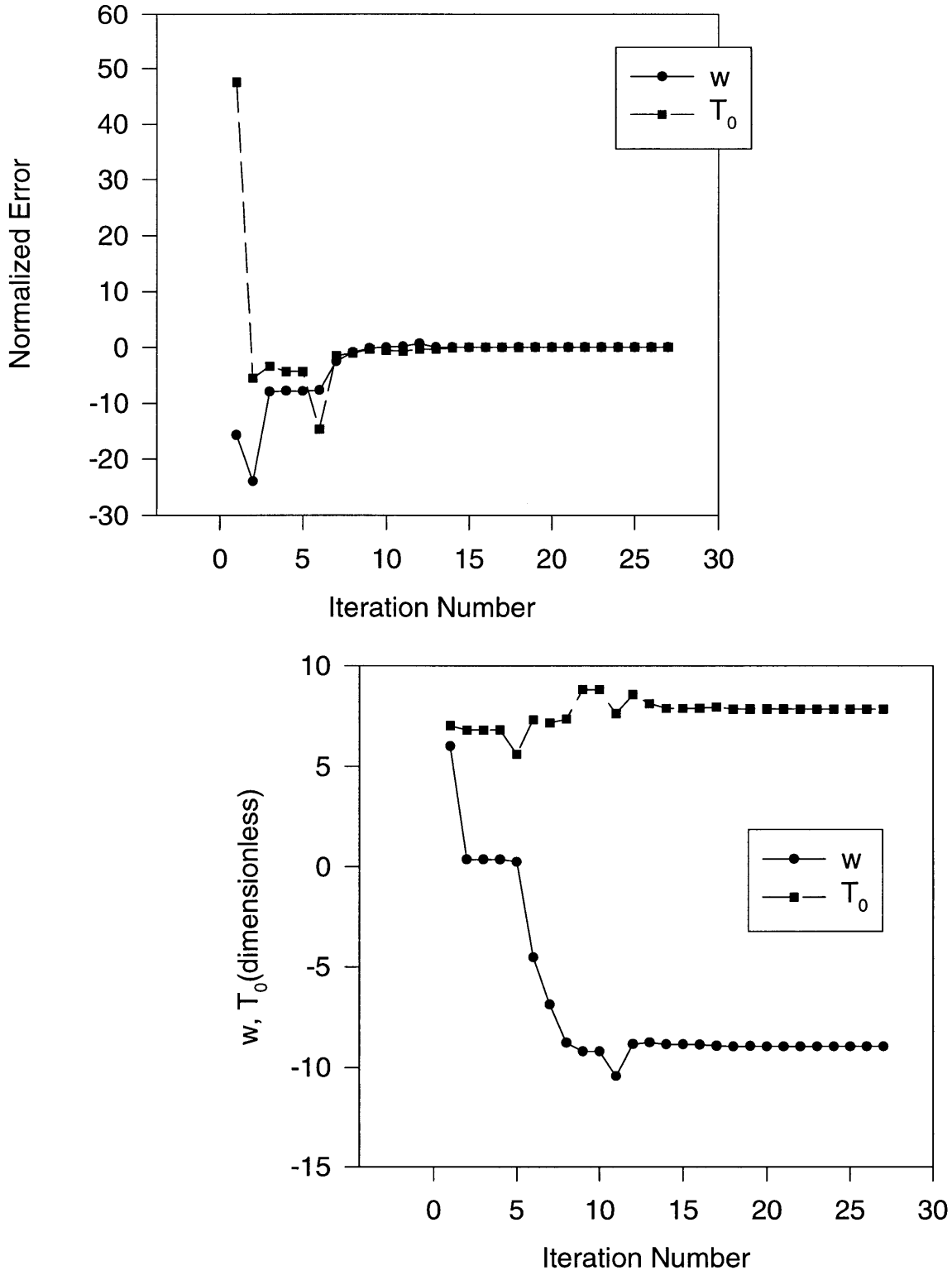

Figure 2-5: Convergence History of Sample Case

chosen. The effect of the choice of grid spacing on the computation results is shown in Figure 2-6 in which profiles of temperature and species mass fractions for different grid densities with the same input conditions are plotted. The results with 21 grid points differ significantly from the other plots, but there is little grid dependency when more than 100 grid points are used.

NO_{ex} mole fractions and formation rates for the same case are plotted against non-dimensional values of z in Figure 2-7. Final values of mole fractions of excess NO reach a maximum of 3.7×10^{-5} -or 37ppm- for this case. The concentration of NO in the flame sheet is essentially a result of a balance between the formation rates and the transport processes of convection and diffusion. Thus, the higher the strain rates applied on the flame sheet, the smaller the accumulation of NO that results.

The profile of NO_{ex} mole fraction is slightly skewed from the flame axis so that the peak lies in the oxidizer portion of the flame sheet. The formation rate was obtained for each grid point on the basis of the local concentration of species and temperature. Profiles of the mass fraction of fuel and oxidizer species and temperature have already been shown in Figure 2-4. Radical species concentrations were obtained for each point by assuming chemical equilibrium at the local temperature, pressure and species concentrations. It should be noted that there is no NO formation in the fuel side of the flame sheet because of the zero values of the concentration of air in this region. Furthermore, for these calculations, NO formation rates for temperatures less than $1700K$ were neglected. The maximum production rate for this case was 1.6×10^{-4} molcm^{-3}s^{-1} occuring near the flame surface. The integral term, S_{NO}, is represented by the area under the profile of the formation rate.

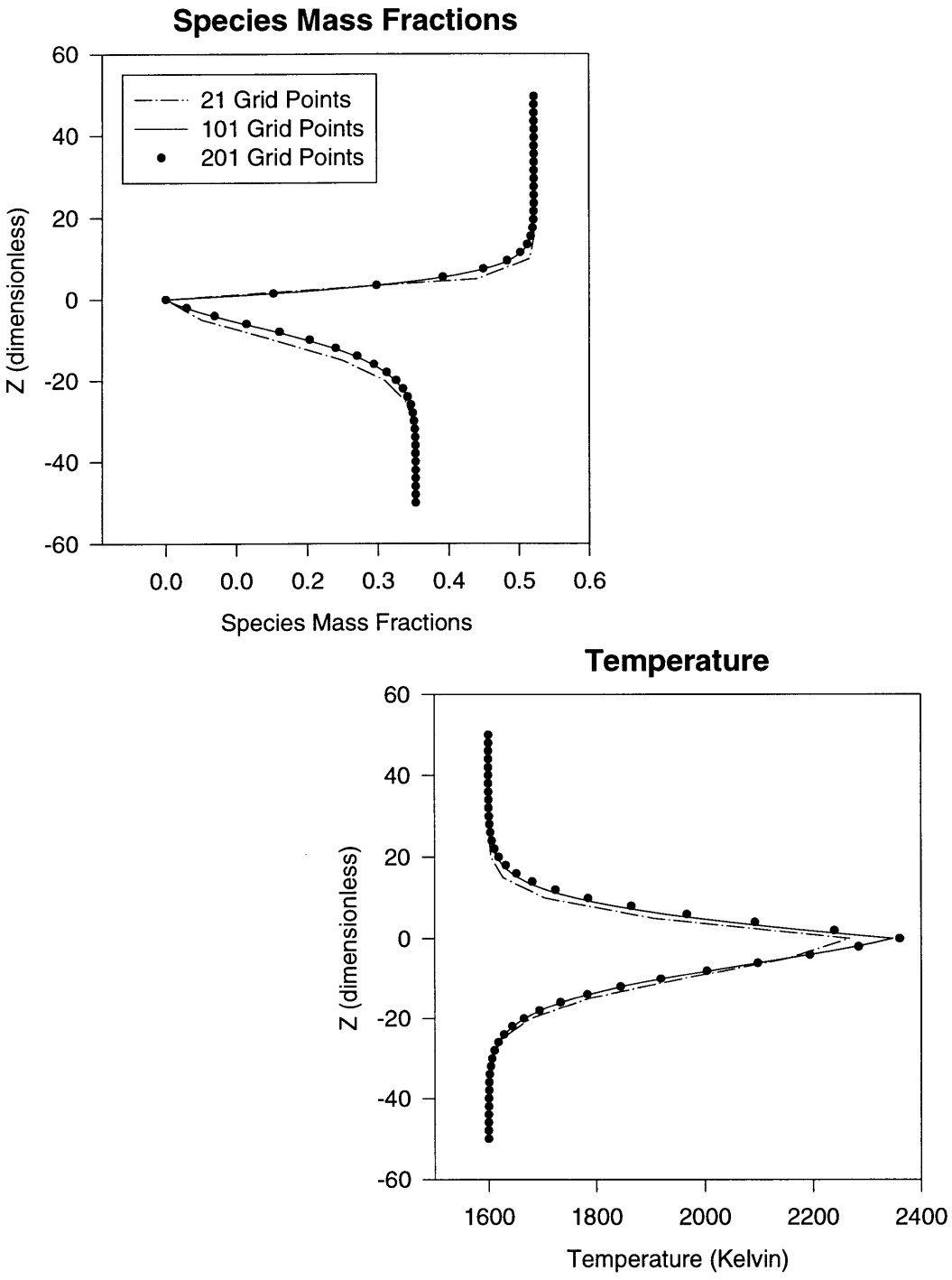

Figure 2-6: Investigation of Grid Dependency of Flame Sheet Calculations

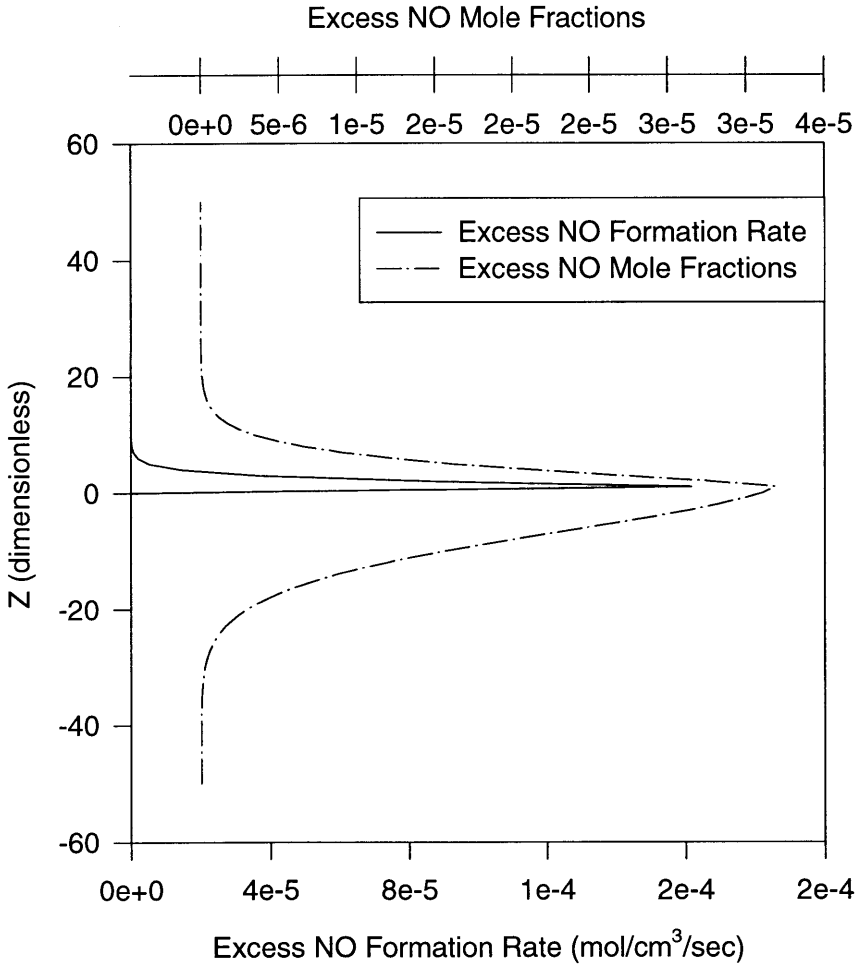

Figure 2-7: Profiles of NO_{ex} Mole Fraction and Formation Rate

Chapter 3

DEVELOPMENT OF THE FLAME SHEET LIBRARY

The end objective in this study of performing flame sheet calculations is in the determination of fuel consumption and excess NO formation rates and the creation of a database of this information for use in the multidimensional model. To accomplish this, a matrix of calculations were performed for several input conditions, chosen to span the range of operating conditions that are known to obtain during diesel combustion. The fuel consumption and excess NO formation rates were determined for each set of inputs used. The range of inputs used in the calculations are summarized in Table 3.1. With the results obtained from these calculations, the behavior of fuel

Variable	Range	Av. step size
Y_{fuel} $(-\infty)$	0 to 1	0.2
Y_{air} (∞):	0 to 1	0.2
Temperature $(\pm\infty)$:	1200 to 2000K	200K
Strain rate:	100 to $10000s^{-1}$	$1000s^{-1}$
Pressure:	60 to 200atm	30atm
Background NO:	100 to 2000ppm	633.33ppm

Table 3.1: Range of Inputs Used in the Determination of the Fuel Consumption and NO Formation Rates

consumption and NO_{ex} formation rates with the variation of the input parameters

was established. The understanding developed led to the creation of an appropriate flame sheet library for use with the multidimensional code.

3.1 Variation of Burning Rate with Input Parameters

The fuel flux at the reaction surface is given by equation(2.16) and is a strong function both of the boundary value of fuel mass fraction and of the fuel equivalence ratio of the system upon which the flame position depends. The plots in Figure 3-1 show the variation of fuel consumption rate with increase in the boundary values of fuel and air mass fractions for different temperatures and pressures. As can be seen in the upper half of this figure, fuel consumption increases with increasing values of $Y_{fuel}(-\infty)$; the gradients being significantly steeper at smaller values of fuel mass fraction. The variation with the $Y_{air}(\infty)$ on the other hand shows less marked differences in rates of change. This figure also indicates that fuel consumption increases with pressure but decreases with increasing temperature and this is a result of the effect that these parameters have on the density and diffusivity of the species. The relationship between temperature and pressure on the fuel consumption rate is shown more explicitly in Figure 3-2 in which it can be seen that fuel consumption decreases slightly with temperature but increases with increasing pressure. The results shown in the upper half of Figure 3-2 were obtained for different values of $Y_{air}(\infty)$ and $Y_{fuel}(-\infty)$ and thus their relative effects on the fuel consumption rate is made evident. Similar comparisons can be made of the relative effect of temperature and strain rate increases in the lower half of the figure; the former variable leading to a small reduction in consumption rate while the latter results in an increase. The effect of strain rate was also examined directly and the results are plotted in Figure 3-3. The rate of strain is related to the diffusion length scale by the expression

$$l_0 = \sqrt{\frac{D_0}{e}} \tag{3.1}$$

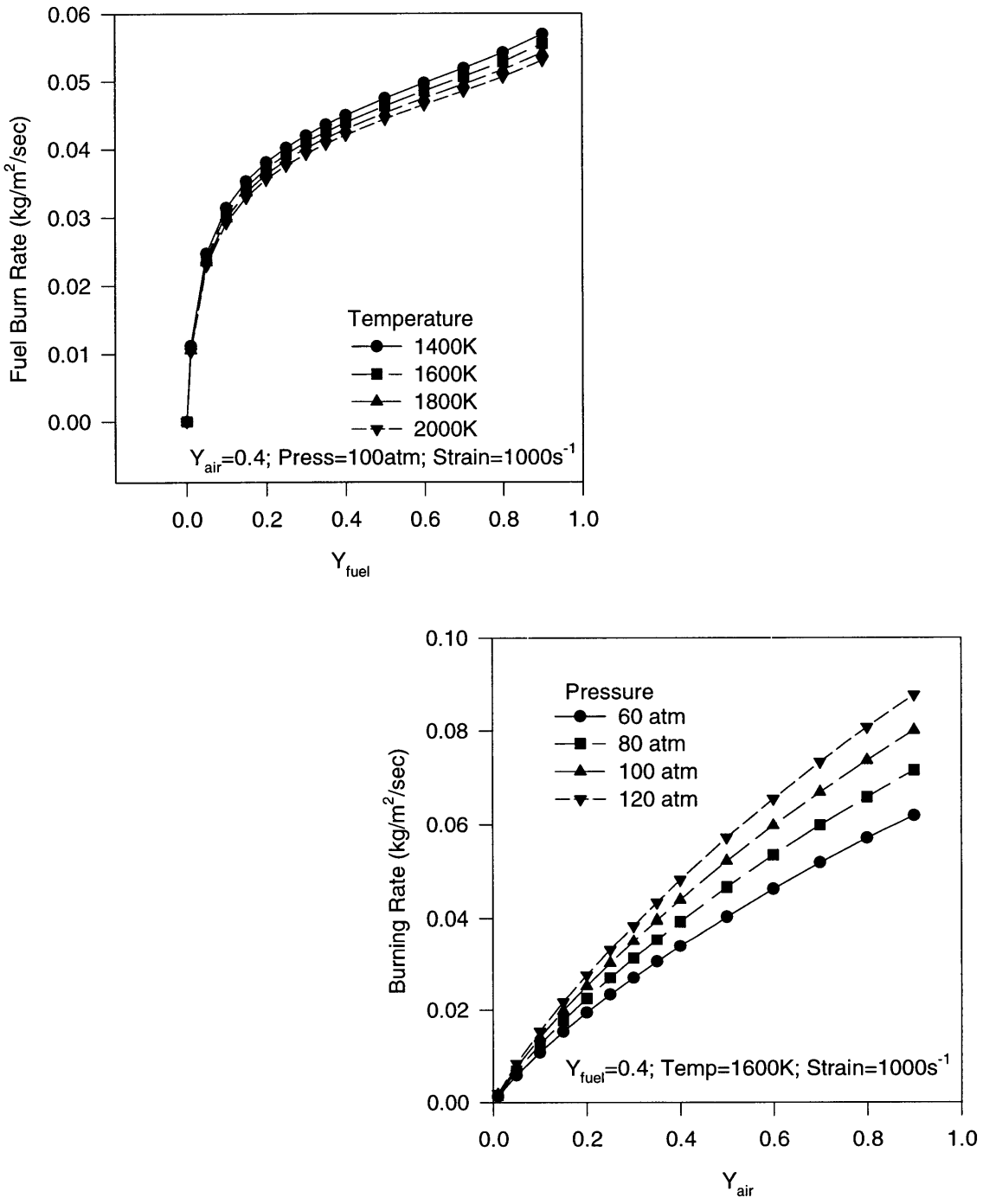

Figure 3-1: Variation of Burning Rate with Species Mass Fraction

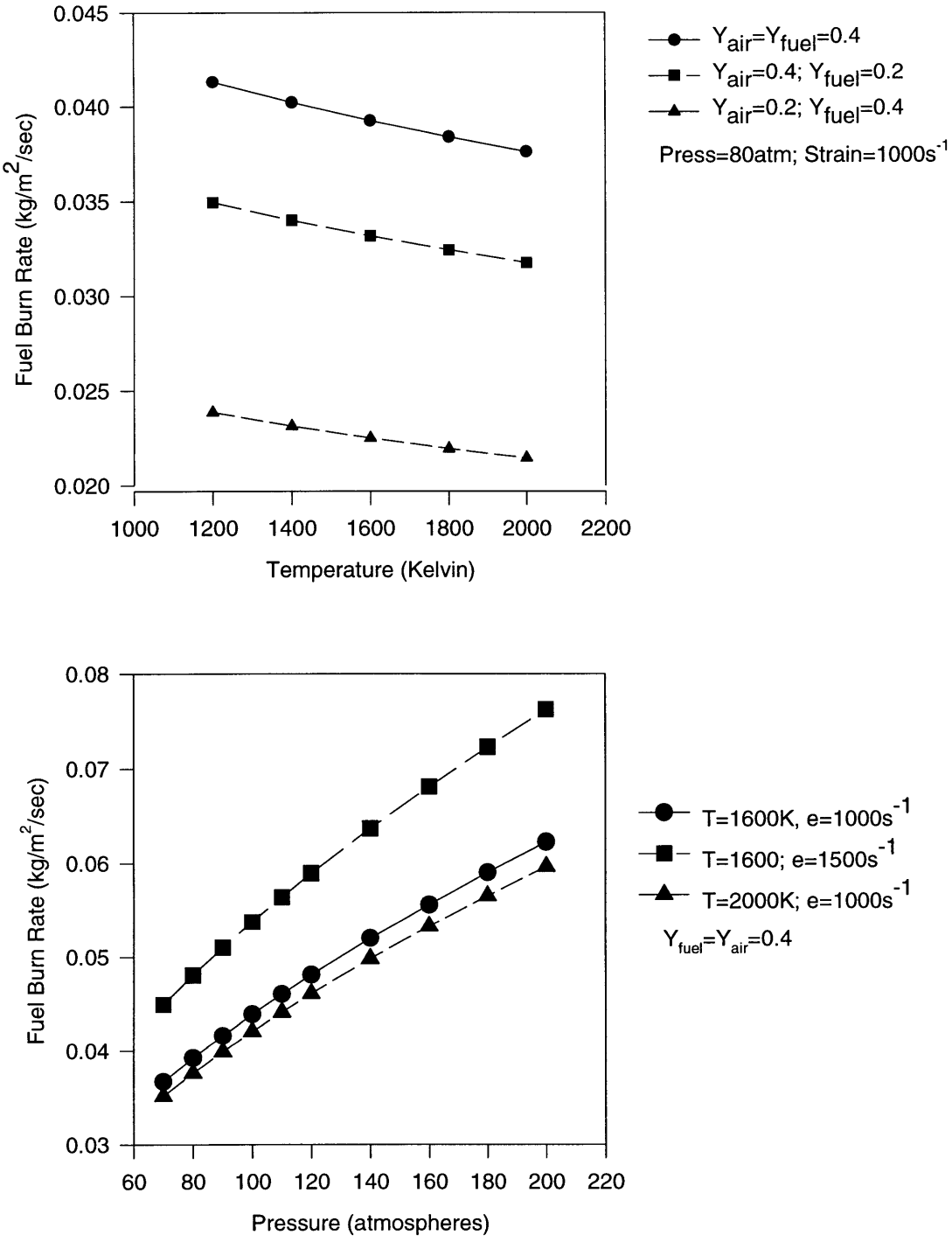

Figure 3-2: Variation of Burning Rate with Temperature and Pressure

and hence, the width of the flame sheet decreases with increasing strain. This in turn causes the fuel consumption rate to increase with the square root of the strain rate as is seen in this plot.

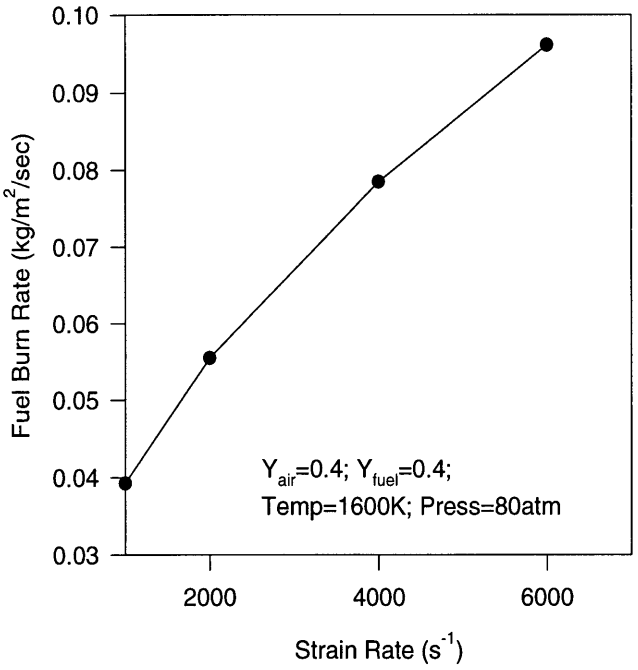

Figure 3-3: Variation of Burning Rate with Strain

3.2 Variation of Excess NO Formation Rate with Input Parameters

The variation of NO_{ex} formation rate with the different input parameters is illustrated in the next three figures. The excess NO formation rate is given by equations (2.45)

and (2.43). Because this is a rather involved expression, some simplification was found necessary in order to clearly demonstrate the dependence of the formation rate on the input parameters. Thus, forward (R^+) and backward (R^-) rates of NO_{ex} formation were defined as follows:

$$R^+ = \int_{-\infty}^{\infty} \left(\left(\frac{d[NO]}{dt} \right)_y^{pos} - \left(\frac{d[NO]}{dt} \right)_{\infty}^{pos} \right) dy \tag{3.2}$$

$$R^- = \int_{-\infty}^{\infty} \left(\left(\frac{d[NO]}{dt} \right)_y^{neg} - \left(\frac{d[NO]}{dt} \right)_{\infty}^{neg} \right) dy \tag{3.3}$$

where

$$\left(\frac{d[NO]}{dt} \right)^{pos} = \frac{2k_1^+[O][N_2]}{\frac{1 + k_1^-[NO]}{k_2^+[O_2] + k_3^+[OH]}} \tag{3.4}$$

and

$$\left(\frac{d[NO]}{dt} \right)^{neg} = 2k_1^+[O][N_2] \frac{\frac{[NO]^2}{K[O_2][N_2]}}{\frac{1 + k_1^-[NO]}{k_2^+[O_2] + k_3^+[OH]}} \tag{3.5}$$

(R^+) and (R^-) are plotted on the left and right of Figures 3-4 through 3-6 respectively. The rates are plotted against species mass fractions for different background NO concentrations in Figure 3-4. Higher values of background NO concentration causes a reduction in the forward rate and an increase in the backward rate as is expected; but the effect of the background concentration is, significantly reduced at higher rates of formation. This is because background NO levels become less significant when compared to the accumulation of excess NO in the flame sheet at higher rates of formation. Increasing fuel and air mass fractions result in higher flame temperatures and hence higher values of R^+ and R^-. The formation rates are, however, more sensitive to variations in the air mass fraction because of the greater effect that this parameter has on the fuel consumption rate, and hence on the flame temperature. The relation between NO_{ex} formation rates and temperature is shown more directly in the upper half of Figure 3-5. Increasing the ambient temperature leads to a commensurate increase in the flame temperature if other parameters remain con-

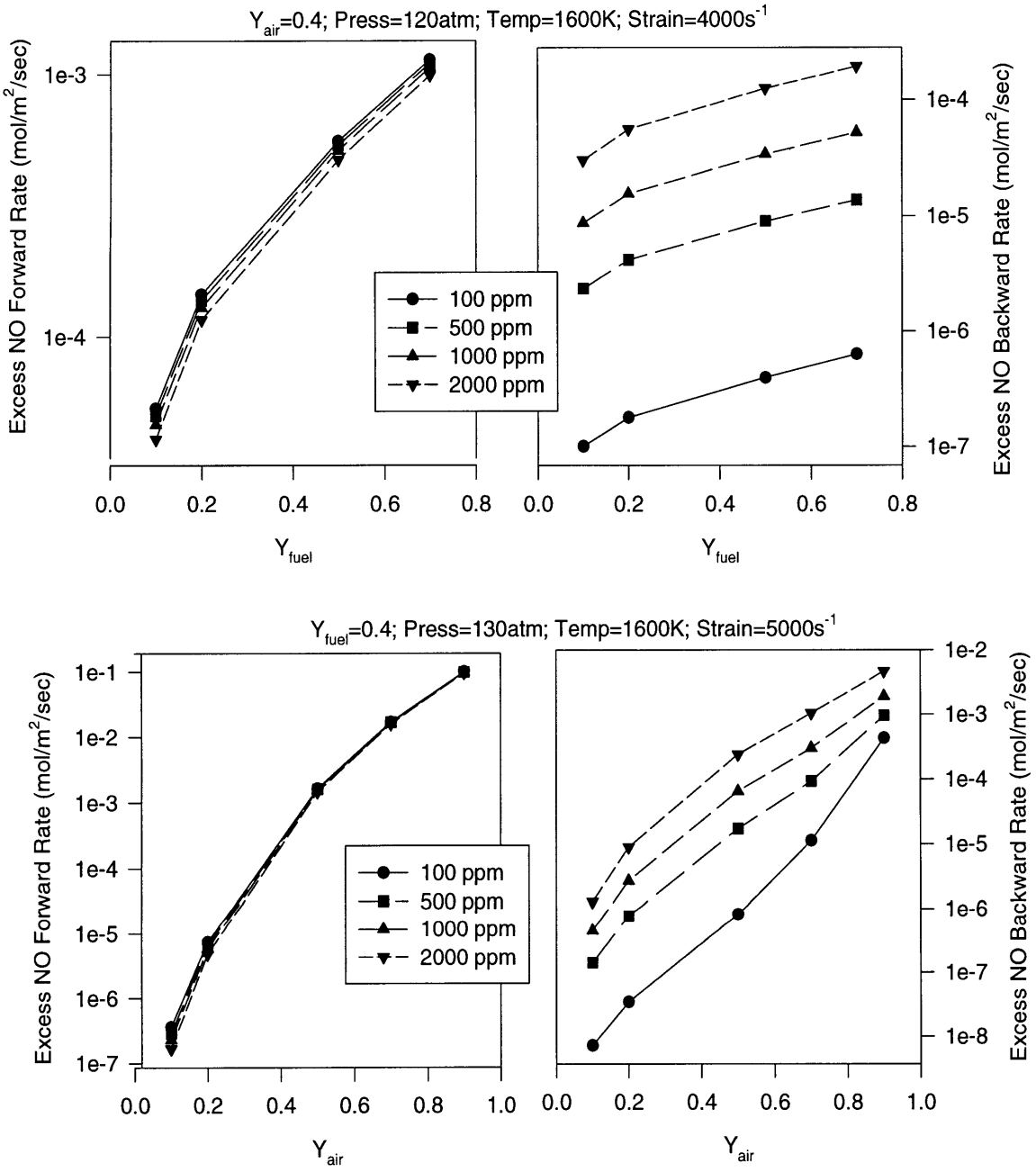

Figure 3-4: Variation of NO_{ex} Formation Rate with Species Mass Fractions

stant. Thus, in these plots, both forward and backward rates are seen to increase exponentially with the ambient temperature.

The effect of the variation in pressure is shown in the lower half of the same figure. The pressure dependence of the formation rates comes from resulting changes in species concentration in the flame sheet with changes in pressure and, for this reason, both forward and backward rates of formation increase with increasing pressure.

Figure 3-6 show the results obtained when strain rates and background concentrations of NO were varied. The width of the flame sheet is inversely proportional to the square root of the rate of strain as discussed in section 3.1 and hence both forward and backward excess NO formation rates decrease with increasing strain. In addition to this, there is a secondary effect of increasing strain on the backward formation rate in that the accumulation of excess NO in the flame sheet is reduced as the strain rate increases.

As the background NO concentration is increased, the R^+ is reduced while R^- increases. The rate of increase of the backward formation rate is initially large but decreases as the total formation rate ($R^+ - R^-$) decreases. This results from decreasing excess NO concentrations in the flame sheet with decreasing total formation rates.

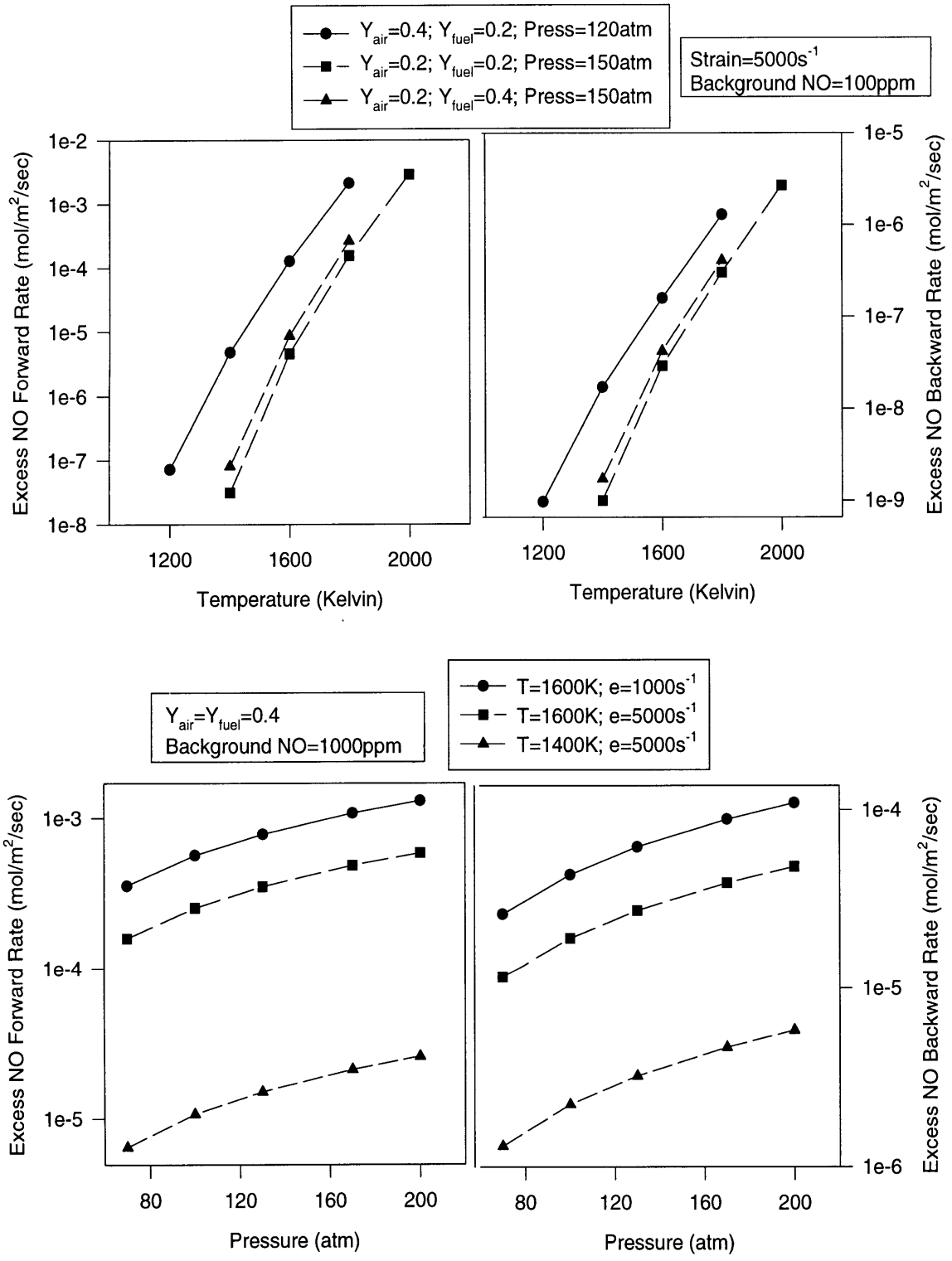

Figure 3-5: Variation of NO_{ex} Formation Rate with Temperature and Pressure

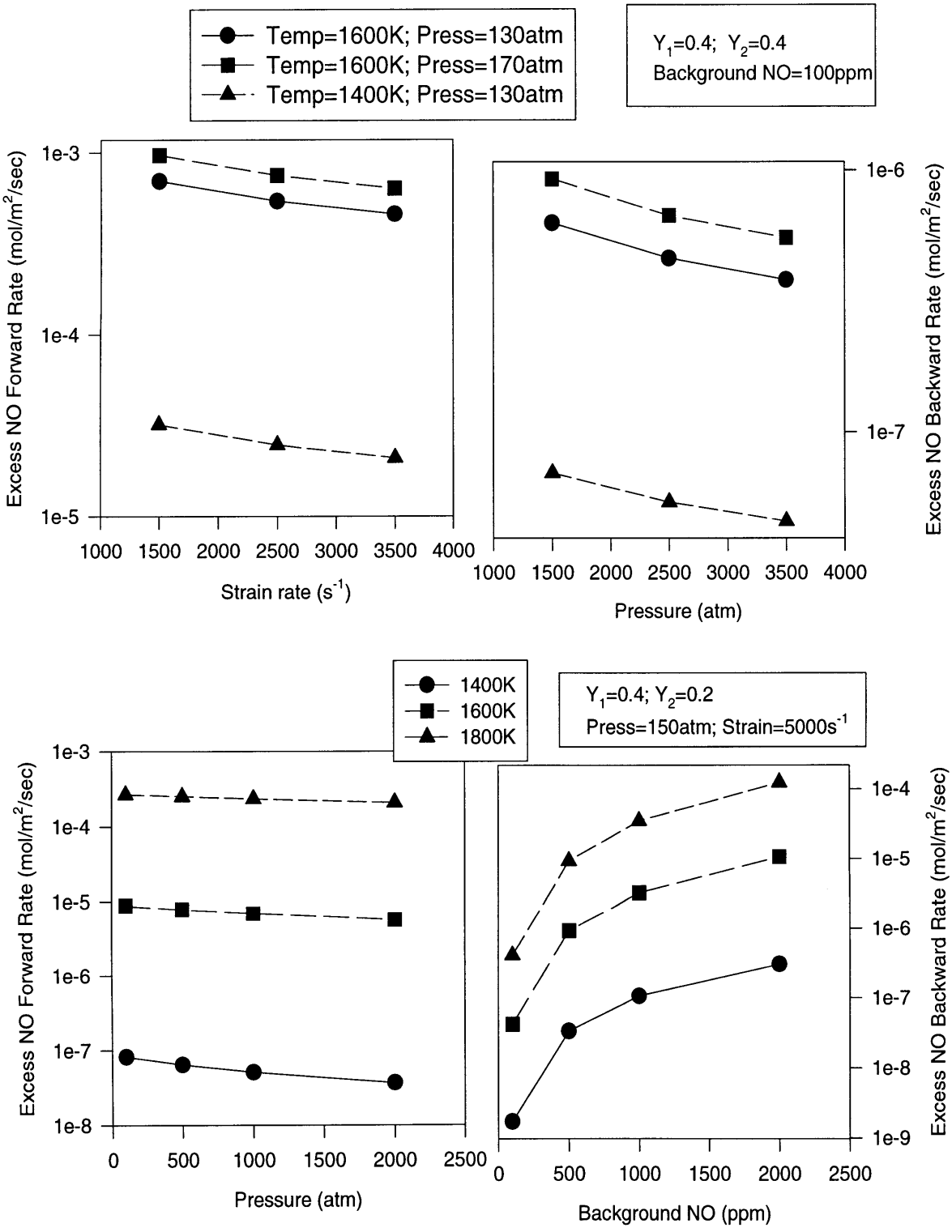

Figure 3-6: Variation of NO_{ex} Formation Rate with Strain And Background NO

3.3 Flame Sheet Library

While the data presented in the preceding sections contains the necessary information on fuel consumption and NO formation rates in the flame sheet, an appropriate means of interfacing these results with the multidimensional code is also necessary for the data to be useful. Linear interpolation of values with five or more parameters could be arduous, and, for this reason, the preferred means of determining functional relations between the formation rates and the different input parameters was employed.

3.3.1 Characterization of fuel consumption rate.

The fuel consumption rate is governed by the following expression (written again for convenience)

$$J_1 = -\rho D \frac{\partial Y_1}{\partial y}. \tag{3.6}$$

The subscripts 1 and 2 refer to the fuel and oxidizer species respectively. The density and diffusivity at the flame surface can be related to local values of temperature and pressure (see Appendix A). The gradient of fuel mass fraction at the flame surface is a function of the width of the flame sheet, the fuel mass fraction of fuel at ambient conditions and the position of the flame sheet relative to the stagnation point. The flame sheet position is itself a function of the overall stoichiometry of the flame sheet system. From these considerations, it is expected that the fuel consumption rate and input parameters will satisfy a functional relation of the form

$$J_1 = k_1 Y_1^{k_2} T^{k_3} P^{K_4} e^{k_5} f\left(\frac{Y_1}{Y_2}\right) \tag{3.7}$$

where $f\left(\frac{Y_1}{Y_2}\right)$ incorporates the effect of the flame sheet position on the fuel consumption rate. From dimensional arguments (see equation(3.10)) the fuel consumption rate is expected to have a square root dependence on the rate of strain. This was demonstrated previously in Figure 3-3. For the remaining variables, the data obtained could be used to determine their corresponding co-efficients and also to test the validity of equation(3.7) as a fuel consumption model. Equation(3.7) can be rewritten

in logarithmic form to obtain

$$\ln\left(\frac{J_1}{\sqrt{e}}\right) = \ln k_1 + k_2 \ln Y_1 + k_3 \ln T + k_4 ln P + k_5 \ln\left(\frac{Y_1}{Y_2}\right) + k_6 \ln\left(\frac{Y_1}{Y_2}\right)^2 \qquad (3.8)$$

where it has been further assumed that the effect of the flame sheet position can be approximated by the sum of the last two terms.

The data obtained from the flame sheet calculations thus represent the following overdetermined system of equations

$$\ln\begin{bmatrix} \frac{J_{1_1}}{\sqrt{e}} \\ \vdots \\ \frac{J_{1_n}}{\sqrt{e}} \end{bmatrix} = \begin{bmatrix} 1 & \ln Y_{1_1} & \ln T_1 & \ln P_1 & \ln\left(\frac{Y_{1_1}}{Y_{2_1}}\right) & \ln\left(\frac{Y_{1_1}}{Y_{2_1}}\right)^2 \\ \vdots & \vdots & \vdots & \vdots & \vdots & \vdots \\ 1 & \ln Y_{1_n} & \ln T_n & \ln P_n & \ln\left(\frac{Y_{1_n}}{Y_{2_n}}\right) & \ln\left(\frac{Y_{1_n}}{Y_{2_n}}\right)^2 \end{bmatrix} \times \begin{bmatrix} k_1 \\ k_2 \\ k_3 \\ k_4 \\ k_5 \\ k_6 \end{bmatrix} \qquad (3.9)$$

which was solved using the least squares method. The values obtained for the constants k_1 through k_6 are given in Table 3.2.

k_1:	-6.6044
k_2:	1.0212
k_3:	0.7642
k_4:	-0.0305
k_5:	-0.1839
k_6:	0.5045

Table 3.2: Fuel Consumption Rate Coefficients

Values of J_1 are in $kg/m^2/sec$. Temperature and pressure are expressed in Kelvin and atmospheres respectively and the strain rate is in sec^{-1}. Equation(3.8) and the above constants thus constitute the fuel consumption rate model that was incorporated into the flame sheet library.

The question of the validity of this model needs to be addressed. The non-

dimensional form of the fuel consumption rate obeys the following relation [15]:

$$J_{fuel} = \rho_0 \sqrt{D_0 e} \tag{3.10}$$

Since density and diffusivity scale with temperature and pressure as shown below (see Appendix A):

$$\rho \sim 1/T; P$$
$$D \sim T^{\frac{3}{2}}; P^{-1}$$

it follows that k_5 and k_6 are expected to have values of -0.25 and 0.5 respectively if other species properties are constant. (It should be noted that the specific heats and thermal conductivities, however, did vary with temperature in the flame sheet model). The values obtained for k_5 and k_6 are close to the expected values and this lends credence to equation(3.8) as being truly representative of the relation of the fuel consumption rate to the different input variables. This is further confirmed by the plot shown in Figure 3-7 in which the data obtained from the flame sheet calculations is plotted against corresponding values obtained using equation(3.8) as a fuel consumption model. As can be seen, agreement is excellent for the values of input variables considered.

3.3.2 Characterization of excess NO formation rate

Upon consideration of equations(3.4) and (3.2), the forward rate of excess NO formation (R^+) is expected to obey a functional expression of the form:

$$\ln(R^+\sqrt{e}) \sim c_1 + c_2 T_f + c_3 \ln Y_2 + c_4 \ln Y_1 + c_5 \ln T_f + c_6 \ln P \tag{3.11}$$

R^+ is multiplied by $\sqrt{e}$ in the above equation to account for the variation of the diffusion length scale of the flame sheet with strain. The formation rate is expected to scale exponentially with T_f which is the temperature at the reaction sheet surface.

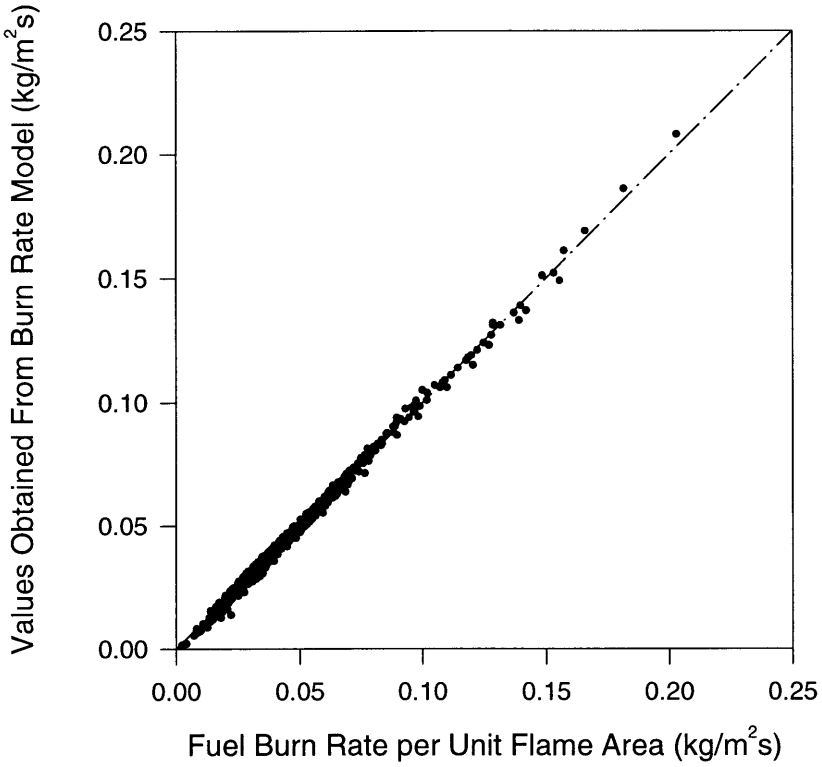

Figure 3-7: Comparison of Values of Fuel Consumption Rate Obtained From Burnrate Fit and Individual Flame Sheet Calculations

(An expression for obtaining T_f is given later in this chapter). The remaining terms on the right hand side of equation (3.11) model the effect of the concentration of reacting species in the flame sheet on R^+. The air mass fraction at the reaction surface is a function of the air and fuel mass fractions at the boundaries of the flame sheet since the diffusion of fuel and air into the reaction zone is in stoichiometric proportions. The overall density and concentrations in the flame sheet also scale with the pressure and temperature.

Rewriting the data obtained from the flame sheet calculations in the form of equation(3.9) and performing a least squares fit to the data, the following values were obtained for the co-efficients c_1 through c_6:

c_1:	-5.24×10^2
c_2:	-1.64×10^{-2}
c_3:	-6.069×10^{-1}
c_4:	-6.678×10^{-1}
c_5:	7.144×10^1
c_6:	1.0556

Table 3.3: R^+ Coefficients

Temperature, pressure and strain rate were expressed in units of Kelvin, atmospheres and sec^1 respectively. The excess NO formation rate was expressed in $mol/m^2/sec$. With the values in Table 3.3, excess NO forward rates were calculated using equation(3.4) for the input conditions used in the flame sheet calculations. The results obtained are compared with data from the flame sheet computations in Figure(3-8) and as can be seen, agreement is quite good.

R^- is plotted against R^+ in Figure 3-9. From equations(3.4) and (3.5), the ratio of the forward and backward rates is proportional to the square of the concentration of NO in the flame sheet. From Figure 3-9 it can be seen that there is a strong dependence of the backward rate on the background concentration of NO at lower values of R^+. This dependence is reduced as the forward rate increases and the excess NO formed in the flame sheet dominates over the background NO concentration. Furthermore, it can be seen from this figure that the rate of increase of R^- with R^+

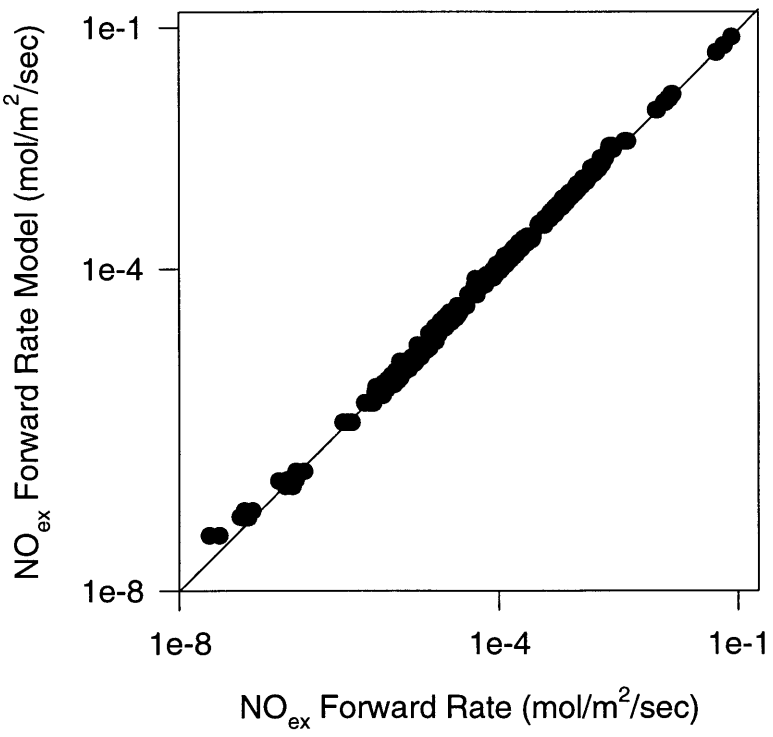

Figure 3-8: Comparison of Values of Excess *NO* Forward Rate Obtained From the Forward Rate Fit and Individual Flame Sheet Calculations

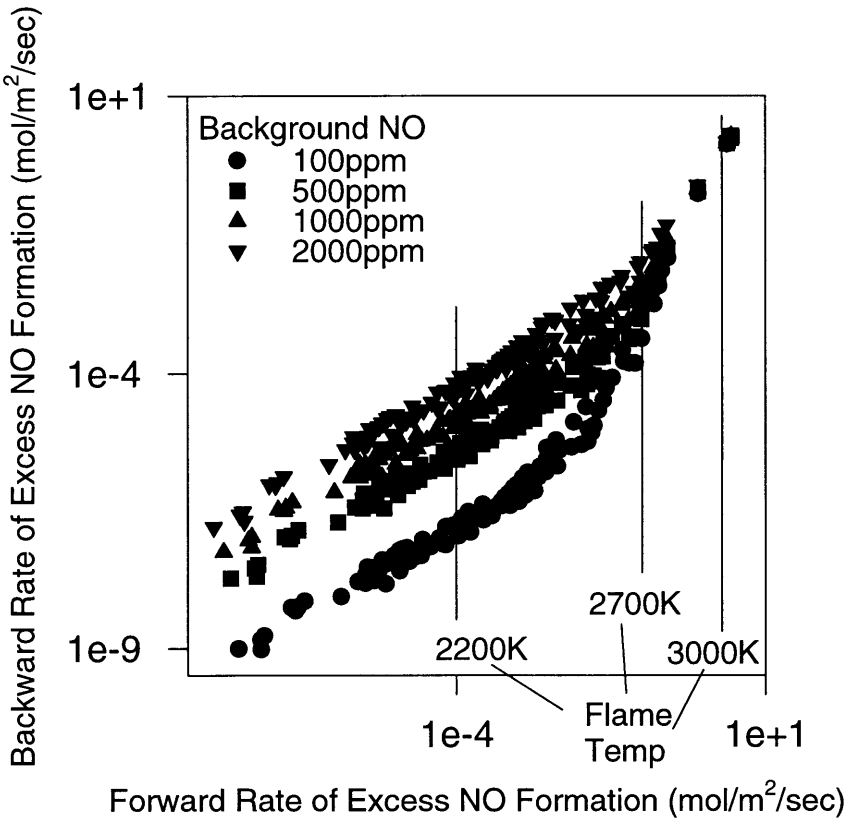

Figure 3-9: Backward Excess *NO* Formation Rates vs Forward Rates

is markedly higher at higher levels of R^+. Again, this follows from the predominance of excess NO over the background concentration as the forward rate increases, so that the backward rates depend more strongly on the rates of NO formation in the flame sheet. In this regime, the backward rate increases faster than the forward rate until equilibrium is almost attained in the flame sheet (at flame temperatures of approximately $3000K$ for the rates of strain that were used in the computations). Past this point, R^- is approximately equal to R^+.

The preceding arguments and consideration of equation(3.5) and (3.3) lead to the supposition that for the regime where R^+ and R^- are not in equilibrium, the behavior of R^- can be adequately expressed by a relation of the form:

$$R^- = a_1[NO]^2 \left(R^+\right)^{a_2} + a_3 \left(R^+\right)^{a_4} \tag{3.12}$$

The first term on the right hand side of equation(3.12) models the backward rates at lower values of R^+ at which the background concentration is the dominant term while the second term will dominate at higher values of the forward rate.

Assuming an expression of this form, the data was used to determine the values of the constants and the results obtained are given in Table 3.4.

a_1:	2.8×10^{-8}
a_2:	6.67×10^{-1}
a_3:	2.33
a_4:	2.0

Table 3.4: R^- Coefficients

The units of R^- is $mol/m^2/sec$. The model was evaluated by comparing the values of R^- obtained using the model and those obtained from the flame sheet calculations; this comparison is presented in Figure 3-10. Agreement between the fit and the flame sheet computations is typically within a factor of 3. Also, it should be noted that for lower values of the backward rate, R^+ is significantly greater than R^- and the backward rate of formation can be neglected. The backward rate becomes significant

only as equilibrium conditions are approached and for these values of R^-, agreement between the model presented above and the results of the flame sheet computations is excellent.

The rate of mixing-in of excess NO formed in the flame sheet with the rest of the charge as flame sheets are destroyed constitutes an additional formation rate which is given by the following equation:

$$R_{mix} = FS_{NO} \times \left(\frac{d\Sigma}{dt}\right)^- \tag{3.13}$$

where FS_{NO} is the integral of excess NO concentration in the flame sheet in the cross wise direction and $\left(\frac{d\Sigma}{dt}\right)^-$ is the rate of destruction of flame sheet. For this to be implemented, the variation of NO concentration in the flame sheet with the input parameters needs to be known and from equation(2.46), the expected dependence of FS_{NO} $(mol/m^2/sec)$ on the input variables is as follows:

$$\ln FS_{NO} = b_1 + b_2 \ln \frac{(R^+ - R^-)}{e} + b_3 \ln P + b_4 \ln T \tag{3.14}$$

As with the previous cases, a least squares fit of the available data yielded values for the constants b_1 through b_4 which are given in Table 3.5 below.

b_1:	-3.4189
b_2:	0.989
b_3:	0.0797
b_4:	0.4978

Table 3.5: Excess NO Concentration Coefficients

A comparison of the values obtained using equation(3.14) and those from the flame sheet calculations are shown in Figure 3-11 below. The results obtained are the same for both cases.

Finally, in the formulation of a model for R^+ (equation 3.11), the flame temperature T_f was used as an input parameter and thus must be available for the model to be implemented. The flame temperature itself can be written in terms of the inputs

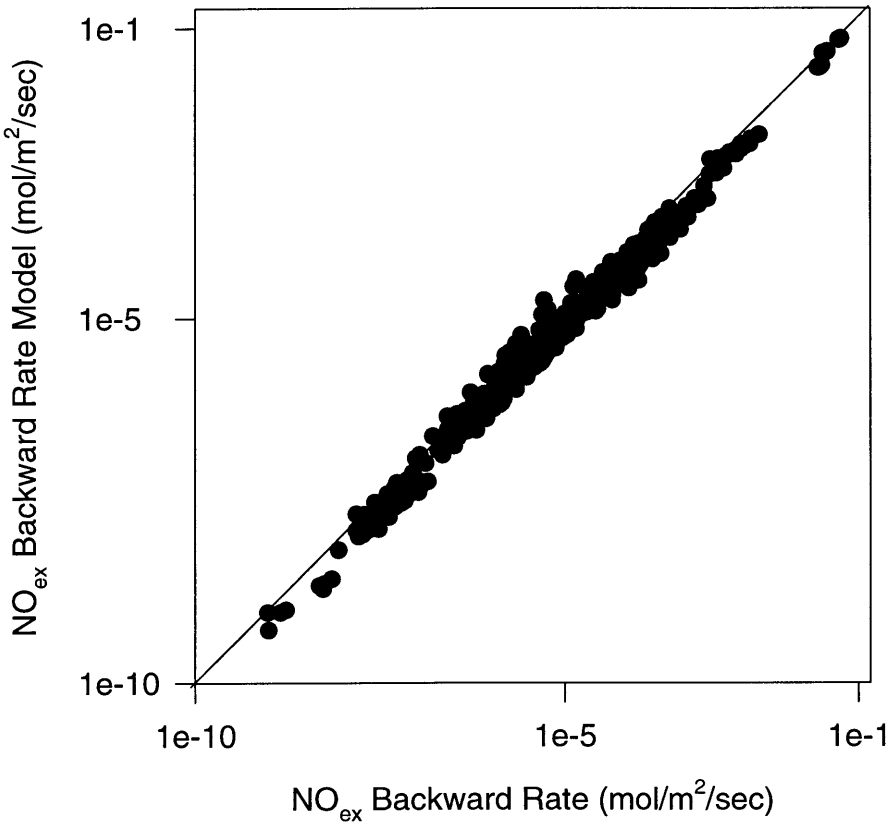

Figure 3-10: Comparison of Values of Excess *NO* Backward Rate Obtained From the Backward Rate Fit and Individual Flame Sheet Calculations

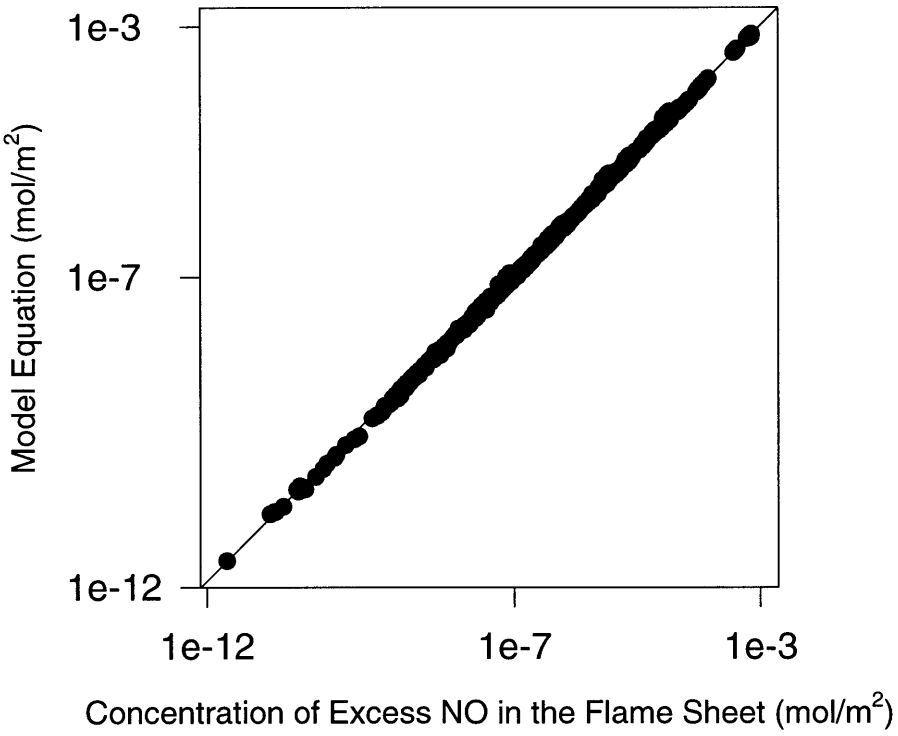

Figure 3-11: Comparison of Values of Excess NO Concentration Obtained From Flame Sheet NO Fit and Individual Flame Sheet Calculations

by recognizing that the gradient of temperature in the reaction zone is a function of the rate of energy release at the reaction surface, the diffusion length scale of the flame sheet and the species properties in the reaction zone. This can be written mathematically as follows:

$$\ln T_{diff} = d_1 + d_2 \ln J_f + d_3 \ln P + d_4 \ln e + d_5 \ln T \tag{3.15}$$

where J_f is the rate of fuel consumption in the flame sheet and T_{diff} is the difference between the flame sheet temperature and T_∞. The values of the co-efficients obtained by performing a least squares fit to the data are shown in Table 3.6 and a comparison between the original data and the model equation are shown in Figure 3-12. The agreement between this model and the original computations is also good in this case.

d_1:	14.8233
d_2:	0.9383
d_3:	-0.4749
d_4:	-0.4715
d_5:	0.0079

Table 3.6: Flame Temperature Coefficients

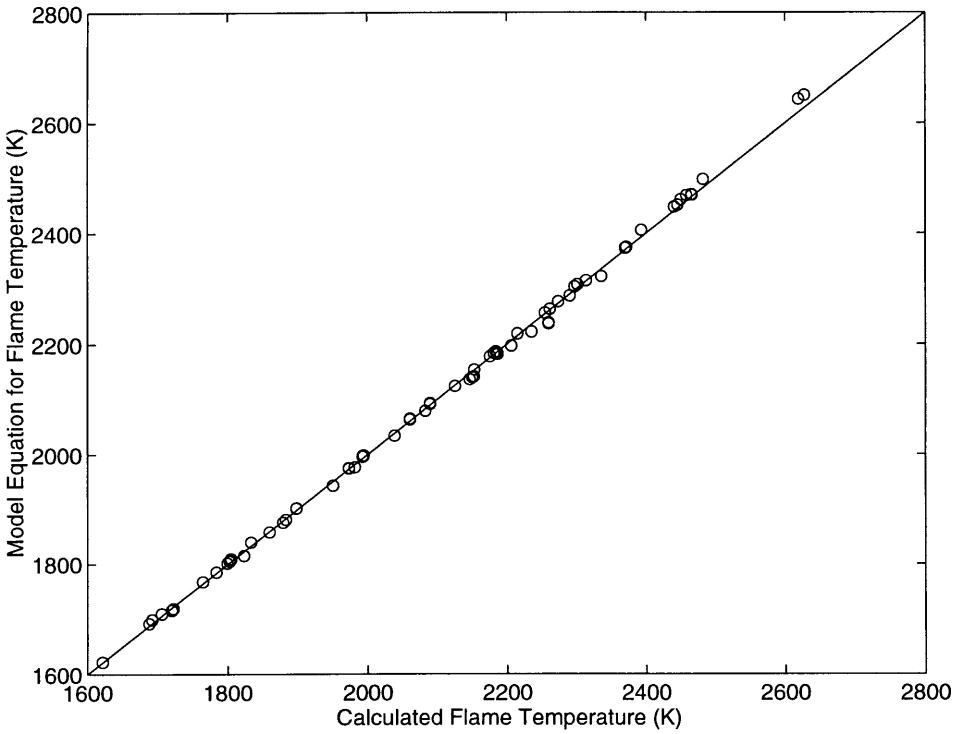

Figure 3-12: Comparison of Values of Flame Temperature Obtained From the Flame Temperature Fit and Individual Flame Sheet Calculations

Chapter 4

IMPLEMENTATION AND TESTING OF THE FLAME SHEET LIBRARY

The flame sheet library described in the preceding chapter was incorporated into the KIVAII code as a combustion submodel. KIVAII was developed for modeling engine combustion and is a multidimensional code based on a finite difference representation of the governing equations[31]. The discretized system of equations are solved in time over a suitable computational grid.

With this modeling approach, each computational cell can be regarded as individual subsystems with its associated scalar and vector variables as illustrated in Figure 4-1. The purpose of the flame sheet library then, is to supply information on the rates of hydrocarbon oxidation and NO formation in each cell and for each time step, based on the properties of species in the computational cell. The different models in the library are summarized in Figure 4-2 for the readers convenience. The flame sheet submodel returns values for the fuel consumption rate and excess NO production rate based on the boundary conditions of the reaction sheet. Thus, for the implementation of the library to be effected, the relationship between the flame sheet boundary conditions and the species properties in the cell have to be established.

The strain rate in the flame sheet is computed from the ratio of the turbulent

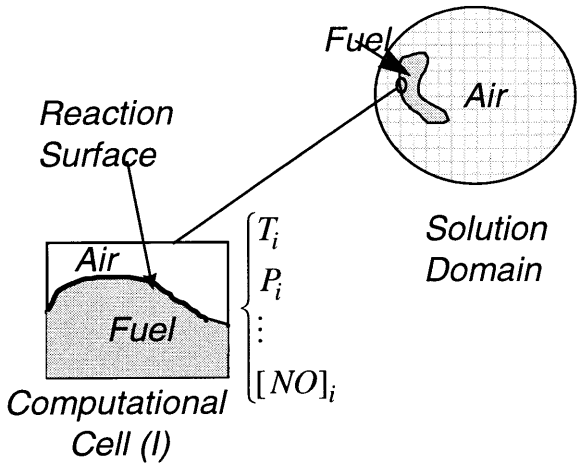

Figure 4-1: Illustration of the Modeling of Combustion with the Finite Difference Approach

kinetic energy in the cell and its dissipation rate, i.e

$$e = c_e \frac{k}{\epsilon} \tag{4.1}$$

where c_e is a model constant. Pressure and boundary conditions of temperature in the flame sheet correspond to the temperature and pressure in the computational cell. Also, assuming the product species is uniformly mixed over the volume of the cell, the species mass fractions at the boundaries of the flame sheet are given by the following expression:

$$Y_1(\infty) = Y_2(-\infty) = \bar{Y_1} + \bar{Y_2} \tag{4.2}$$

where $\bar{Y_1}$ and $\bar{Y_2}$ are the fuel and air mass fractions in the computational cell respectively.

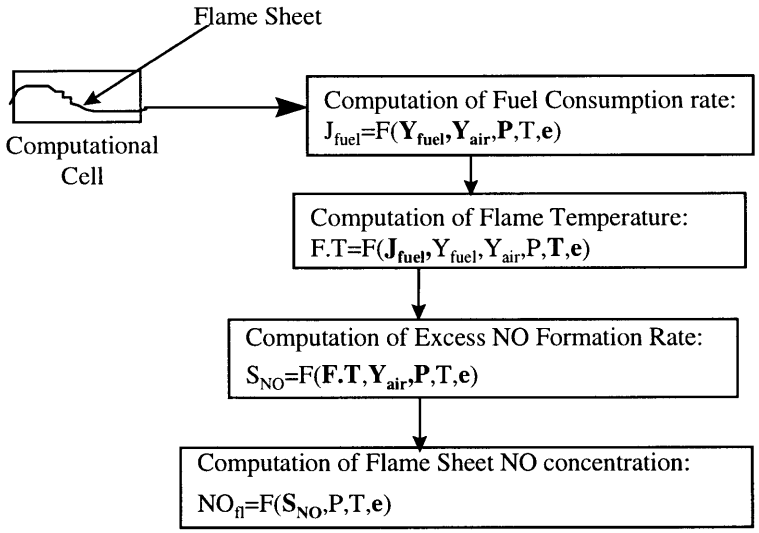

Figure 4-2: Summary of the Models that Constitute the Flame Sheet Library

This model of species formation and destruction rates in the computational cell is completed by the determination of the flame sheet surface area per unit volume (Σ) and this is obtained by solving the following transport equation:

$$\frac{\partial \Sigma}{\partial t} + \frac{\partial u_j \Sigma}{\partial x_j} = \frac{\partial}{\partial x_J}\left(\frac{\nu_t}{\sigma_\Sigma}\frac{\partial \Sigma}{\partial x_j}\right) + \alpha \epsilon_s \Sigma - \beta\left(\frac{\dot{Y}_1}{\bar{Y}_1} + \frac{\dot{Y}_2}{\bar{Y}_2}\right)\Sigma^2 \tag{4.3}$$

The evolution of Σ according to the above equation is computed along with the other variables associated with the bulk flow in the KIVAII code.

The significance of the terms in equation(4.3) have been extensively discussed in previous studies[15][22][16] and for this reason, only a brief synopsis is presented here. The second term on the left accounts for the convective transport of flame sheet by the bulk gas flow. The first term on the right accounts for turbulent diffusion; ν_t is the turbulent viscosity and σ_Σ is the turbulent schmidt number for the flame surface density. A value of unity for σ_Σ was used in the computations. The two other terms on the right hand side of equation(4.3) model the production and destruction rates of the flame sheet density by the flow and combustion processes. The generation rate is proportional to the product of the rate of strain and the flame sheet density. Also,

the ratio

$$\frac{\dot{Y}_k}{\bar{Y}_k};\ k = 1, 2 \tag{4.4}$$

is the speed at which the reactants are consumed. Hence, recognizing that Σ is equivalent to the average separation distance between adjacent flame sheets, the rate of destruction of Σ is given by the last term on the right hand side of equation(4.3). The constants α, β and c_e were determined by calibrating the model to match experimental results.

4.1 Evaluation of the Flame Sheet Model

4.1.1 Experimental results and engine specifications

Evaluation of the flame sheet model was performed by comparison of modeling results with experimental results obtained from a Cummins N14 engine. The specifications of the engine are given in Table 4.1 and the operating conditions at which the data was obtained are given in Table 4.2. The terms PIP and SOI stand for the peak injection pressure and start of injection respectively while A/F is the air-fuel ratio.

Compression Ratio	15.5
Bore	13.97cm
Stroke	15.24cm
Con. Rod Length	30.48cm
No. of Injector Orifices	8

Table 4.1: Specifications of the Cummins N14 Engine

The data available on the performance characteristics of this engine included cylinder pressure traces, heat release rates, fuel injection rates and exhaust concentrations of NO.

Rpm	1800
PIP(ksi)	25.5
SOI	356.8
EGR(%)	0
A/F	24.9

Table 4.2: Operating Conditions

The piston silhouette is shown in Figure 4-3. The squish regions and piston bowl constitute the solution domain for the modeling of the combustion and flow processes. The computational grid created for this purpose is shown in Figure 4-4. The grid was created for a 45 degree sector of the engine, taking advantage of its symmetry and is made up of 26 cells in the radial direction, 10 in the azimuthal and up to 35 cells in the axial direction.

4.1.2 Modeling results

While the focus in this study is on the modeling of NO formation during combustion, the strong sensitivity of NO formation rates to temperature makes an accurate determination of the heat release rate also important. A measure of the closeness of the predicted heat release rate to those obtained in the physical system can be realized by a comparison of the experimental cylinder pressure traces to those computed by KIVAII. Such a comparison is shown for the baseline case in Figure 4-5. Also shown in the same figure is the predicted fuel burnout fraction and cylinder averaged NO concentration and a comparison of the predicted and experimental heat release rates. The experimental heat release is the apparent heat release rate deduced from the pressure curve while the predicted values are the net heat release rates obtained using KIVAII (i.e after heat losses to the cylinder walls have been accounted for). It can be seen from this figure that there is a reasonable matching of the experimental and computed pressure and heat release rate curve. Thus, it is expected that the bulk cylinder temperatures are also closely predicted. It should be borne in mind, however, that the actual distribution of temperature within the charge is equally vital

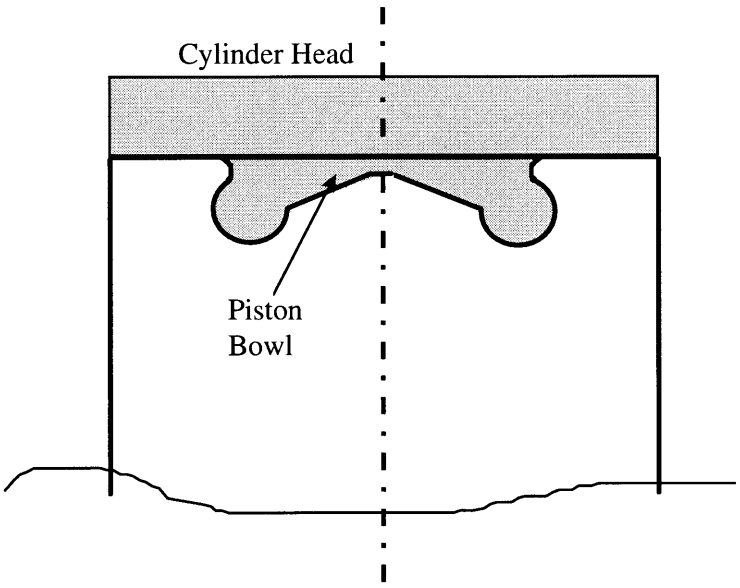

Figure 4-3: The N14 Engine Piston Silhouette

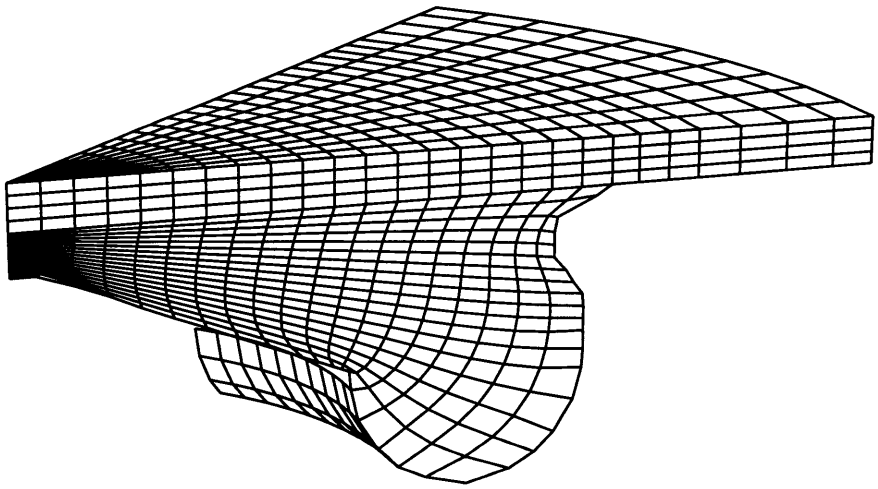

Figure 4-4: Computational Grid Used in Modeling the N14 Engine

for the accurate modeling of NO and experimental data is lacking for the verification of the predictions of these values.

The flame sheet model was calibrated by adjusting the model constants α, β and c_e to match the heat release rate in the baseline case, but the same values for these constants were used in subsequent cases (Chapter 5). In addition to the constants, there is a strong dependence of the rate of heat release on the dynamics of the fuel spray since the latter is largely responsible for the creation and maintenance of the mixing patterns in the charge. Unfortunately, the representation of the jet dynamics by KIVAII is questionable at best and it was found necessary, in this study, to make adjustments to the model to improve both the penetration of the jet and the exchange of momentum between the jet and the charge. Specifically, smaller injection orifices were used (the area was decreased by 10%) and the co-efficient of drag was modified according to the following law:

$$c_d = c_d \quad x < a \tag{4.5}$$

$$c_d = c_d(1 + b(x - a)) \quad x > a \tag{4.6}$$

where x is the radial distance from the axis in cm. The above modification was adopted because of the increase in cell size with increasing radial distance from the center of the engine. This in effect means an increase in the mass of gas with which the spray has a direct exchange of momentum and a smaller impact on the velocity of the charge as the cell sizes increase. The linear increase in the co-efficient of drag corrects this effect to some extent. Values of $2.65cm$ and $3.03cm$ were determined for a and b by trial and error.

From Figures 4-5 it can be seen that the heat release rate is characterized by a relatively short premixed burn followed by a period of diffusion controlled combustion lasting approximately 60 crank angle degrees. The premixed burn fraction is small because the high manifold pressure and the high load of operation lead to high pre-ignition temperatures and a small ignition delay. Figures 4-6 through 4-12 are plots of the model predictions of the progress of combustion for the baseline case at

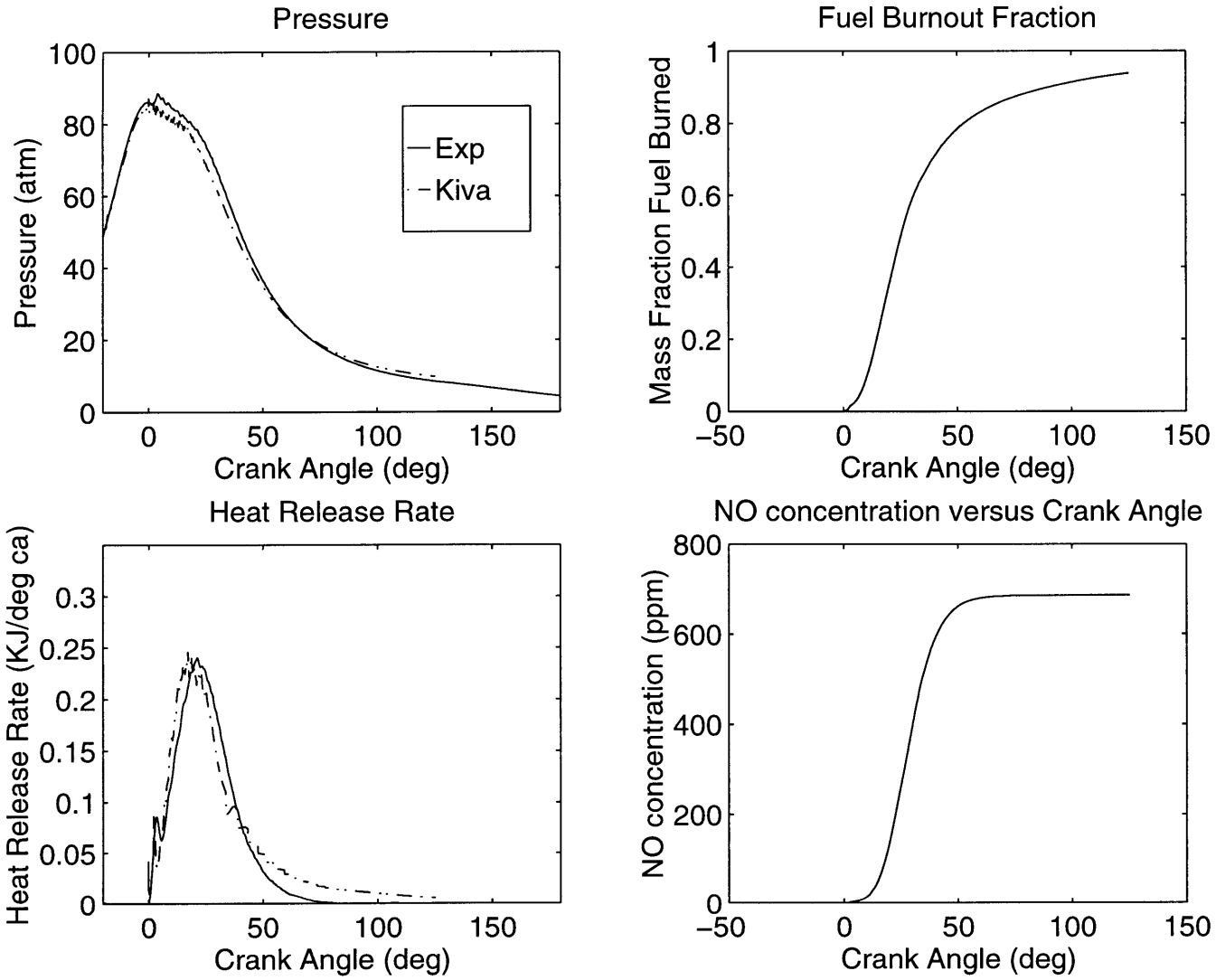

Figure 4-5: A comparison of Kiva and Experimental Results for the Base Case

different crank angles. Each frame is a cross section along the center line of the computational grid which also corresponds to the axis of the fuel jet. Figure 4-6 shows the development of the fuel jet and the diffusion of the fuel into the surrounding air as individual fuel droplets vaporize. The injection duration in the baseline case was from -3.2 to 26.6 degrees ATDC. The role of the jet in promoting the mixing of the fuel and air species is clearly seen in Figure 4-7 in which vector plots of the velocities of the charge are shown. Gas velocities are high in the vicinity of the spray and two recirculation zones are seen on either side of the fuel spray. The larger of these recirculation zones extends into the piston bowl and enhances the mixing of fuel with the air in the bowl as can be seen in the bottom plot of Figure 4-6.

Combustion was initiated at -0.25 degrees ATDC in cells having adequate fuel vapor concentrations. The limits used in these runs were air-fuel ratios of 0.1 and 10 times the stoichiometric value, and these values were chosen in an attempt to match the premixed burn fraction in the base case. This is only an approximate representation of premixed combustion process, obviously, and a more detailed model is still needed which will account for the physics of the ignition delay period. However, little error is expected to result from this simplified model in these runs as the premixed burn fraction was small in each case.

Flame sheets were initialized in those cells having appropriate stoichiometry with values of Σ such that the production and destruction terms (see equation(4.3)) were in equilibrium. This prescription is arbitrary but this is of little consequence as the high rates of strain prevalent in the charge requires that Σ approaches quasi-equilibrium values quickly. Plots of the contours of predicted flame sheet density at different crank angles (Figure 4-8) show the effect of the generation and transport of Σ by the strain generated by the fuel spray. Peak values of flame sheet density of 150cm^{-1} indicate a separation distance of 6.7×10^{-3}cm between flame sheets.

Local values of Σ and the fuel consumption rate per unit flame surface area provide the rate of fuel consumption and hence the rate of energy release in each computational cell. This value is in turn used as a source term in the energy equation. Figure 4-9 shows contours of predicted temperature in the charge at different crank

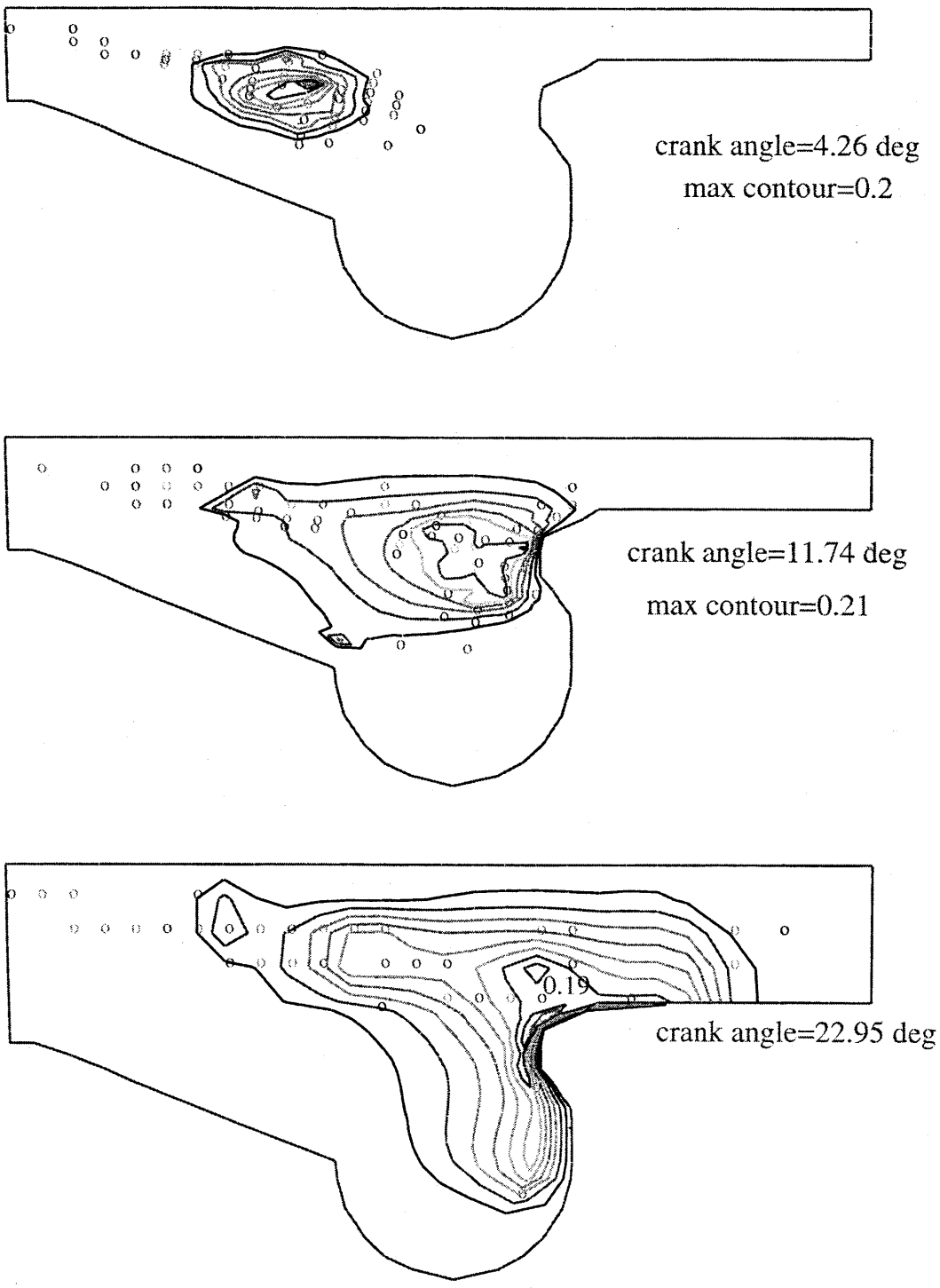

Figure 4-6: Fuel Spray and Contours of Fuel Mass Fraction at Different Crank Angles for the Base Case

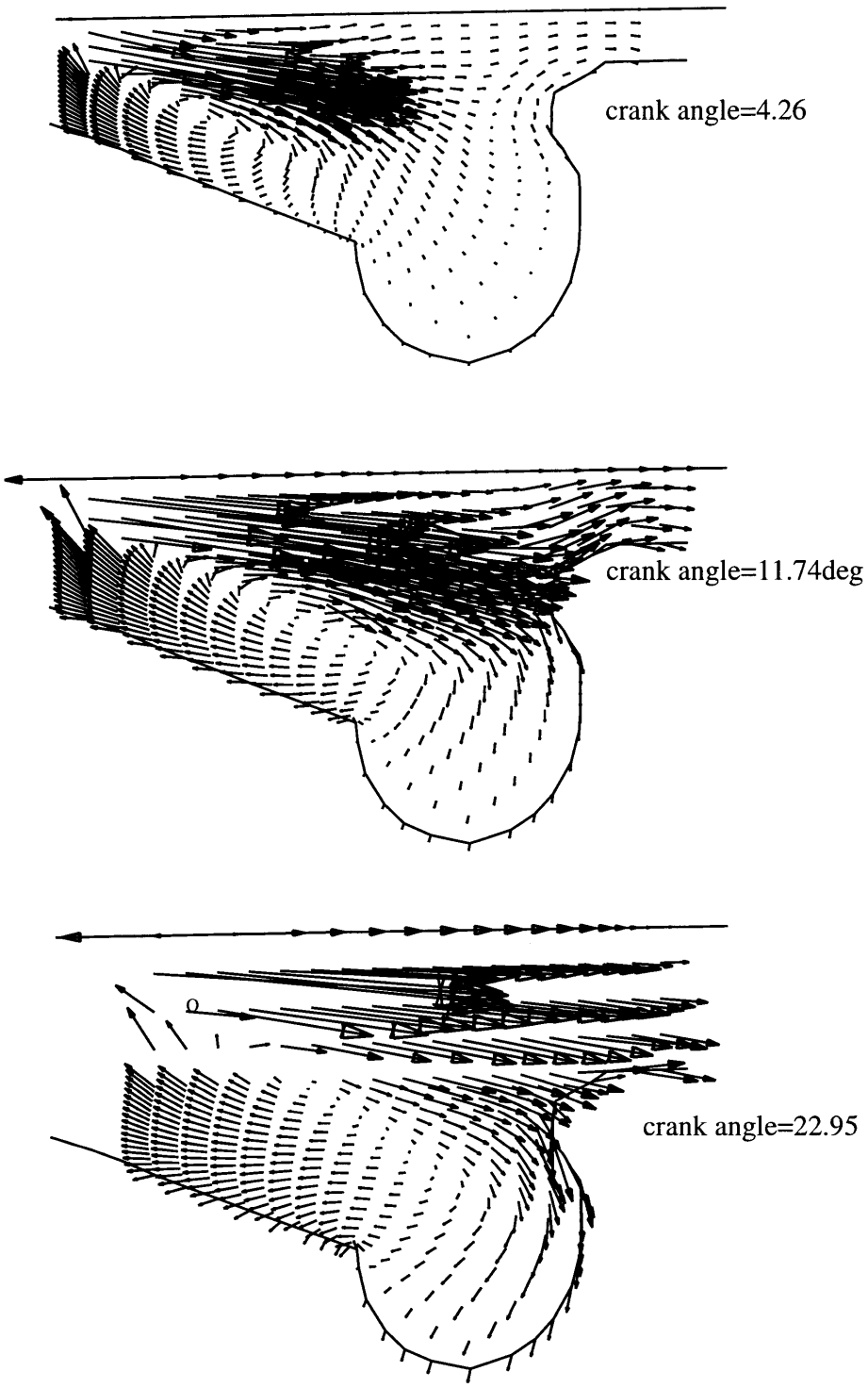

Figure 4-7: Velocity Vectors -Base Case

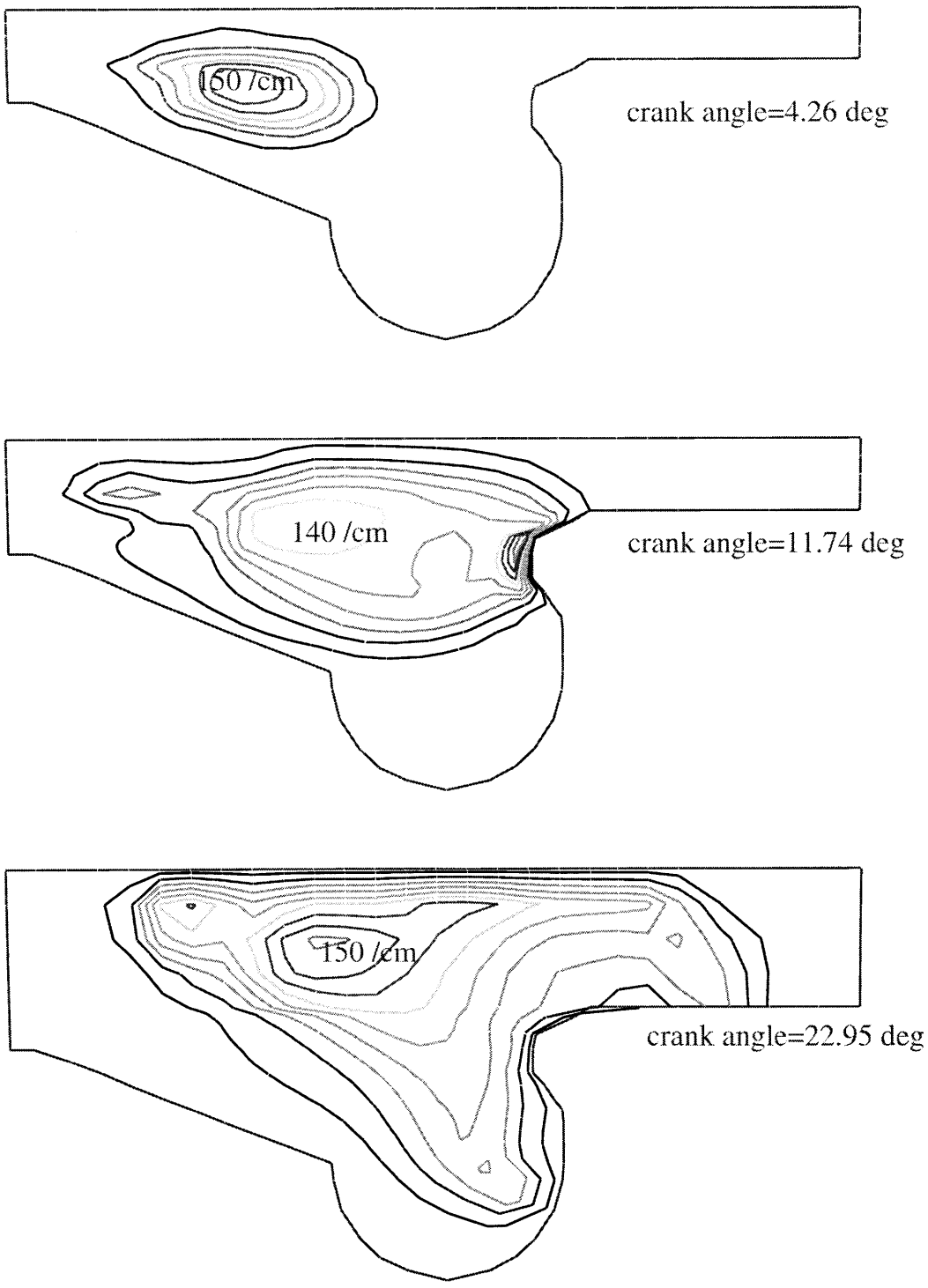

Figure 4-8: Contours of Flame Sheet Density (cm^{-1}) for different crank angles. -Base Case

angles. Maximum temperatures occur on either side of the fuel spray where the mixing of fuel and air species is most effective.

Predicted values of excess and bulk NO formation rates are shown in the next two figures. Contour plots in both figures closely follow the temperature distribution as is expected, but excess rates of formation are at least an order of magnitude higher than the bulk rates.The concentration of Excess NO in the charge are shown for the different crank angles in Figure 4-12.

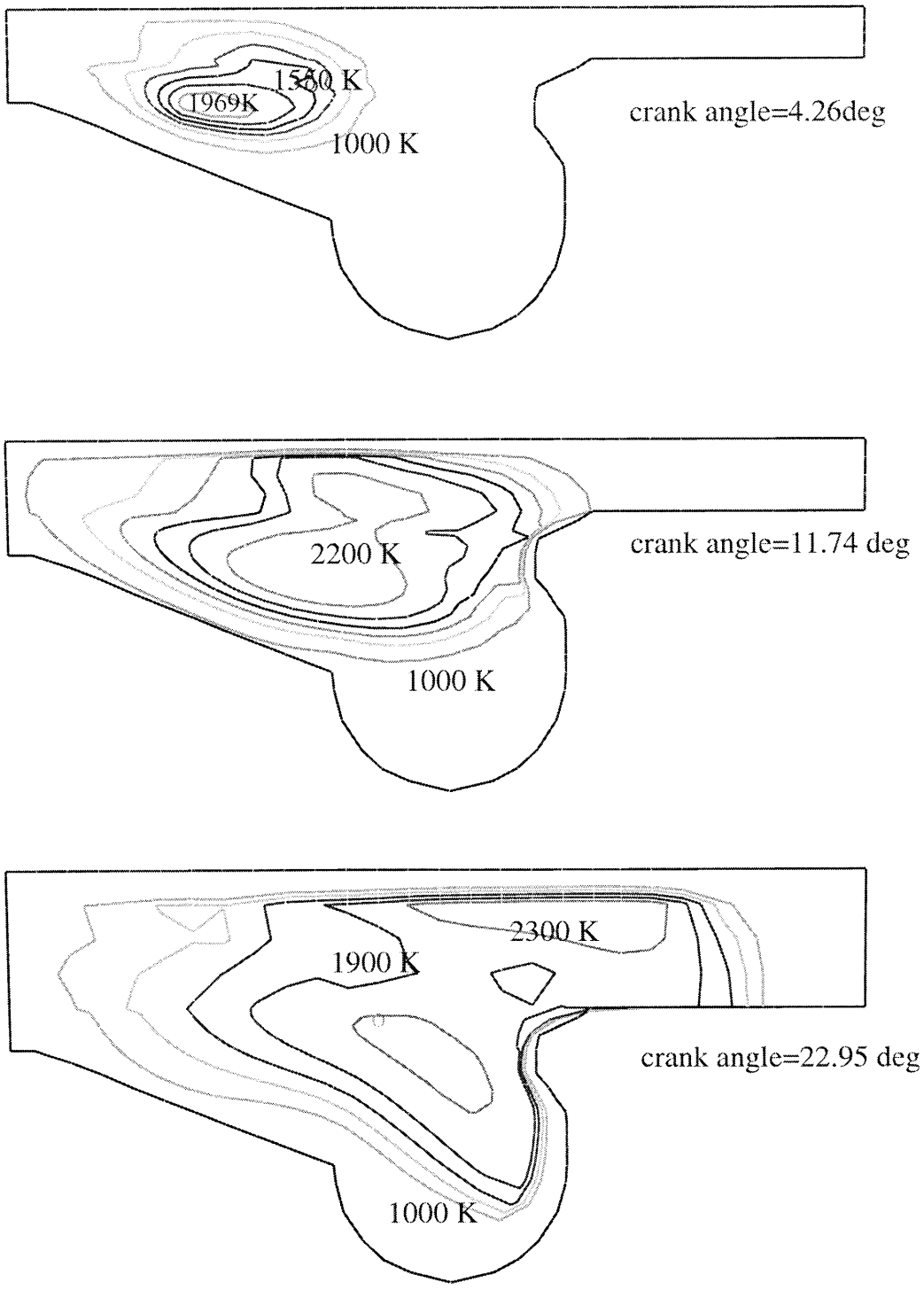

Figure 4-9: Contours of Temperature for different crank angles. -Base Case

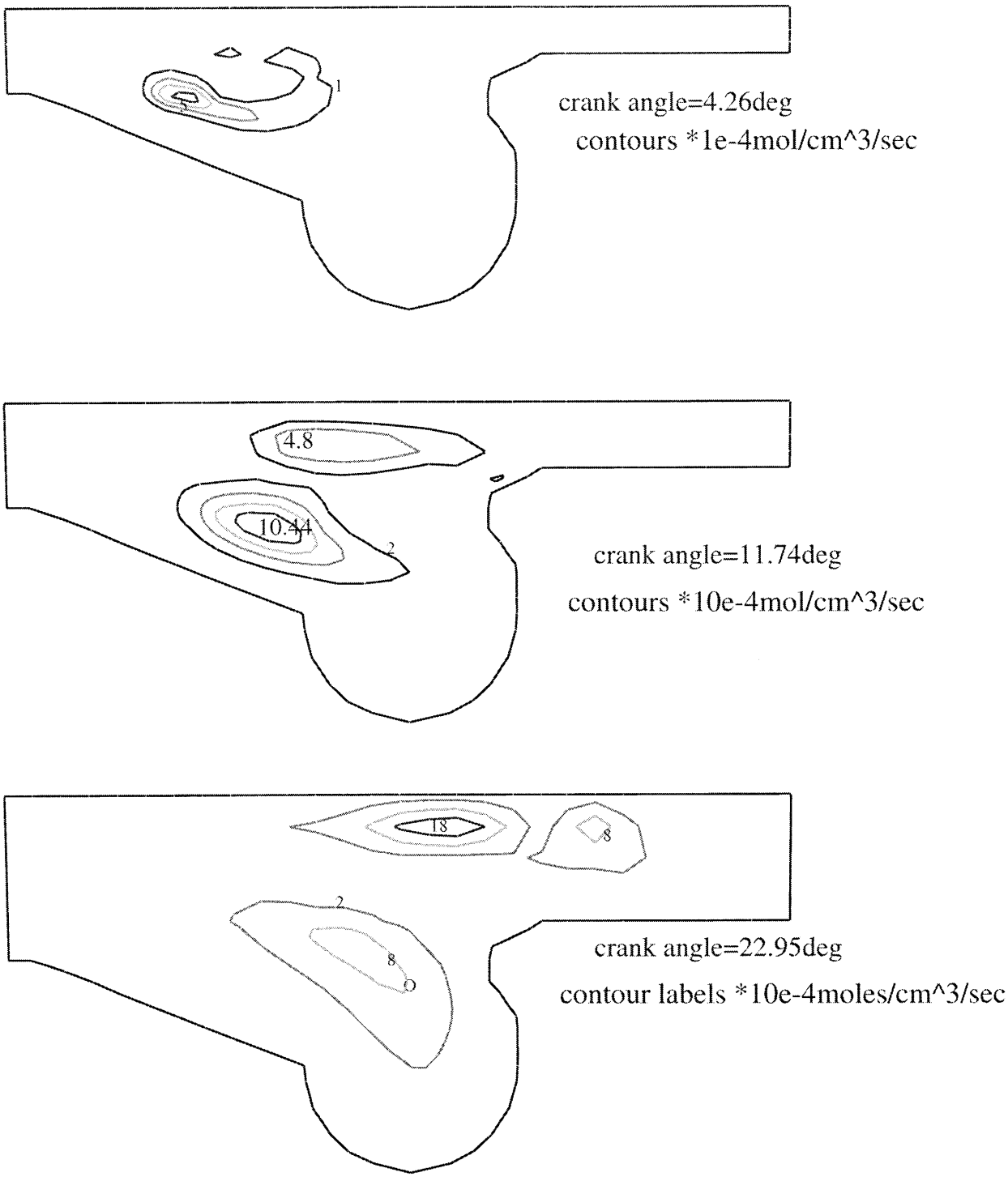

Figure 4-10: Contours of Excess NO production rate ($mol/cm^3/sec$). -Base Case

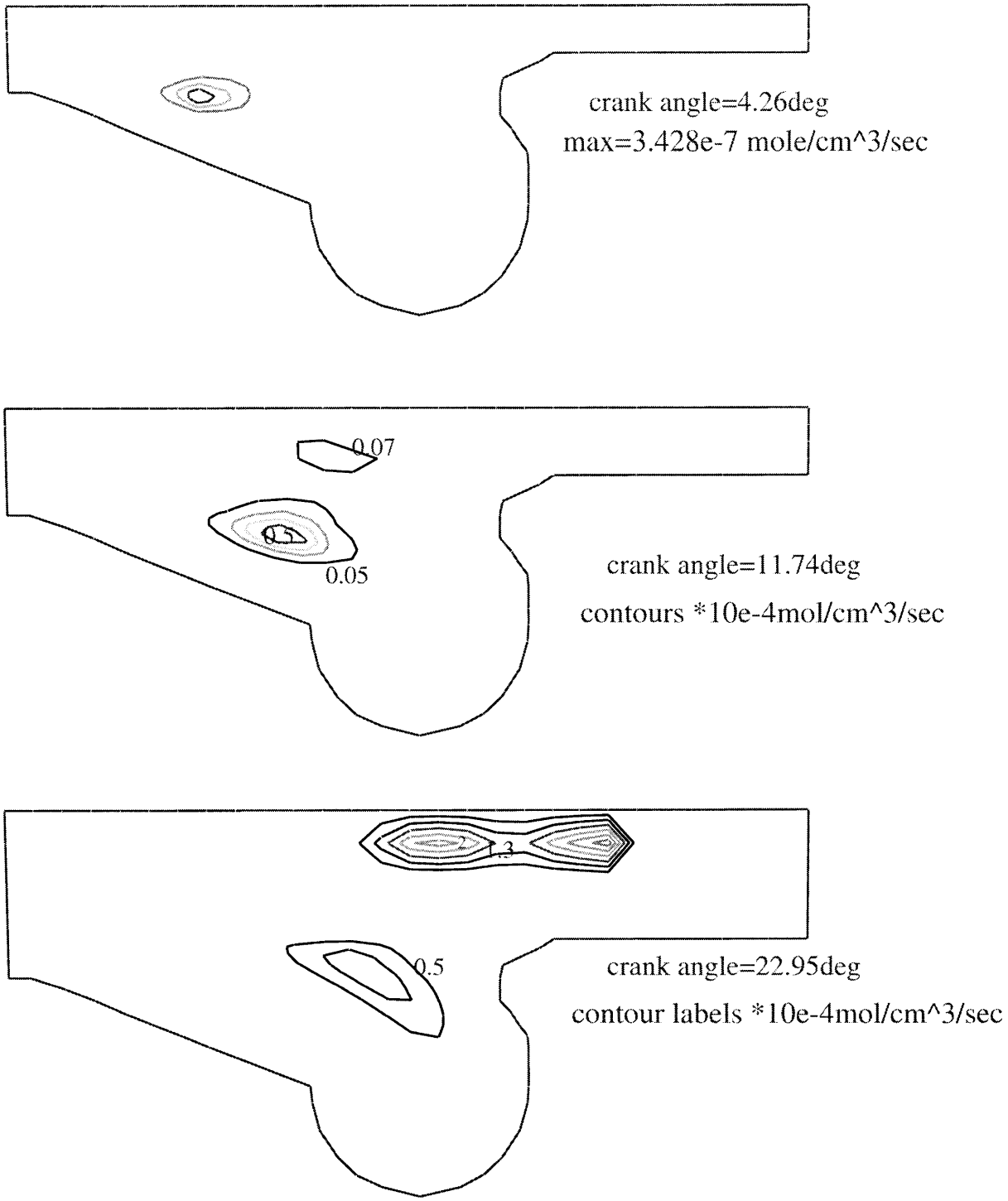

Figure 4-11: Contours of Bulk NO production rate ($mol/cm^3/sec$). -Base Case

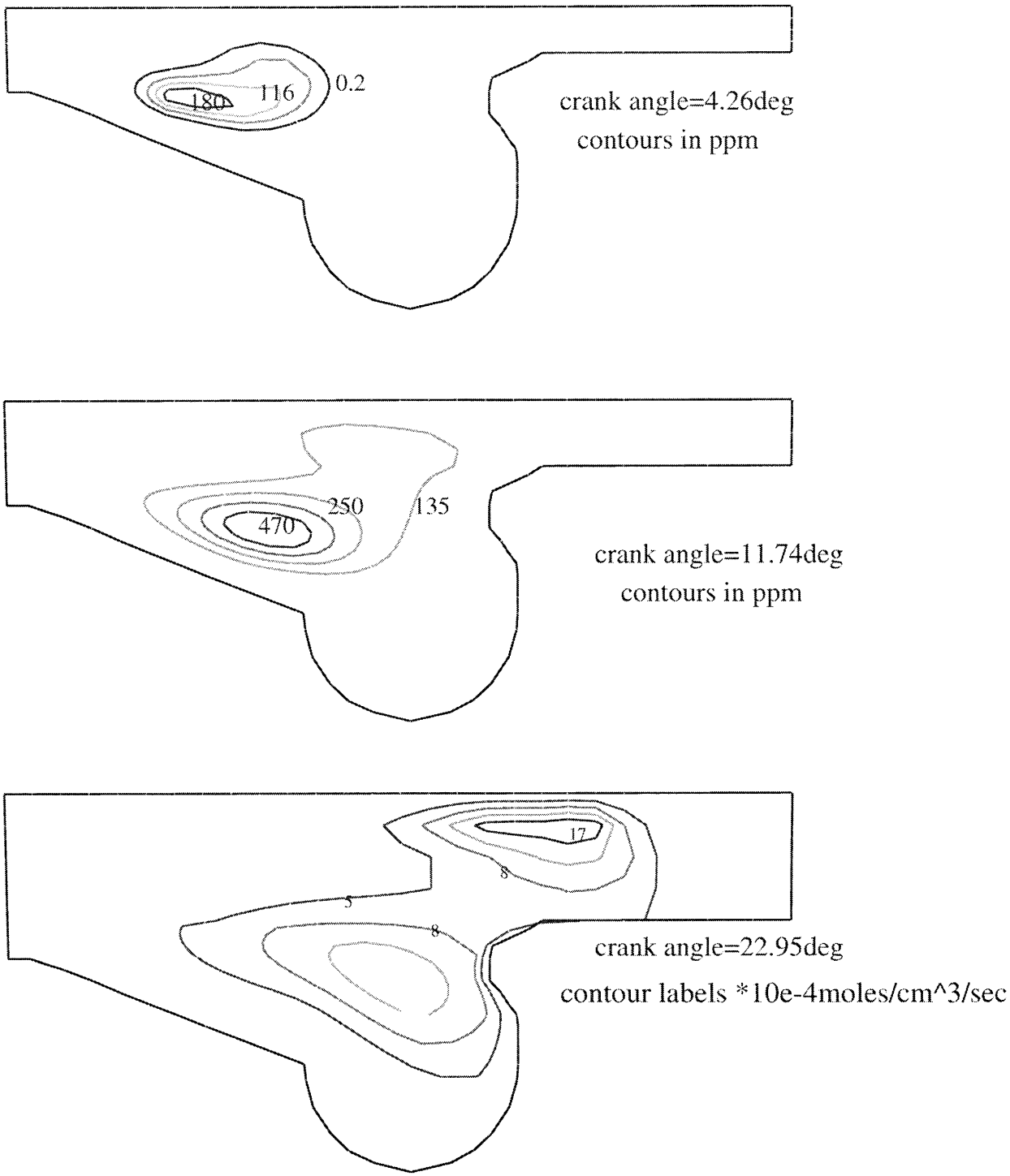

Figure 4-12: Contours of Excess NO mole fraction (*ppm*). -Base Case

Chapter 5

PARAMETRIC SIMULATIONS

Additional experimental data obtained from the N14 engine described in the preceding chapter provides information on the effect of the variations in operating parameters on the concentration of NO in the exhaust. Changes were made in three operating variables; engine speed, injection timing and the fraction of exhaust gas recirculated. The operating conditions used in these runs are shown in Table 5.1. The baseline conditions are also included in the same table for the purpose of comparison.

Parameter	Baseline	Case2 RPM var	Case3 SOI var	Case4 EGR var
Rpm	1800	1200	1800	1800
PIP(ksi)	25.5	15.8	23.7	25.7
SOI	356.8	361.5	364	356.8
EGR(%)	0	0	0	10
A/F	24.9	24.9	24.7	22.7
IMT(K)	320	315	320	322

Table 5.1: Operating Conditions of N14 Engine Experimental Data

The KIVAII model with the incorporated flamesheet submodel was used to obtain predictions of the progress of combustion and NO formation at these operating conditions. Figures 5-1 through 5-3 show comparisons of the predicted and experimental pressure traces and heat release rate curves along with the predicted fuel burnout

fraction and NO concentration in the charge. There is a close match between the predicted and experimental rates of heat release in each case. The reader might note that all three plots indicate that the peak heat release rate is slightly underpredicted for these cases, whereas, the results obtained for the baseline case (Figure 4-5) showed a slight overshoot of the predicted rate over the experimental results. The reason for the difference in the model behavior for the different runs is difficult to ascertain. This is because the differences are small and typically within the bounds of acceptable error. Also, the dataset is small and the information that is available is limited.

5.1 Effect of Parametric Variations on NO Formation

The influence that changes in the engine operating characteristics have on the exhaust concentrations of NO lies in their effect on the gas temperatures and also on the residence time of fuel-lean mixtures in the high temperature zones. Figures 5-4, 5-5 and 5-6 show contours of fuel mass fraction, temperature and NO mole fraction in the charge for the three cases studied. These results were obtained in the latter part of the fuel injection event in each case. As in the preceding chapter, each frame is a cross section along the center line of the computational grid.

Reducing the engine speed (Run 2) causes an increase in the residence time and hence an increase in exhaust NO concentrations. As can be seen in Figure 5-4, fuel concentration and temperature profiles at this crank angle are similar to those obtained in the base case (see Figures 4-6 and 4-9) but the NO concentration profiles are slightly higher. The results obtained in Cases 3 and 4 (Figures 5-5 and 5-6 respectively) show how retarded timing and exhaust gas recirculation causes reduced gas temperatures and hence, resulted in a reduction in NO formation rates.

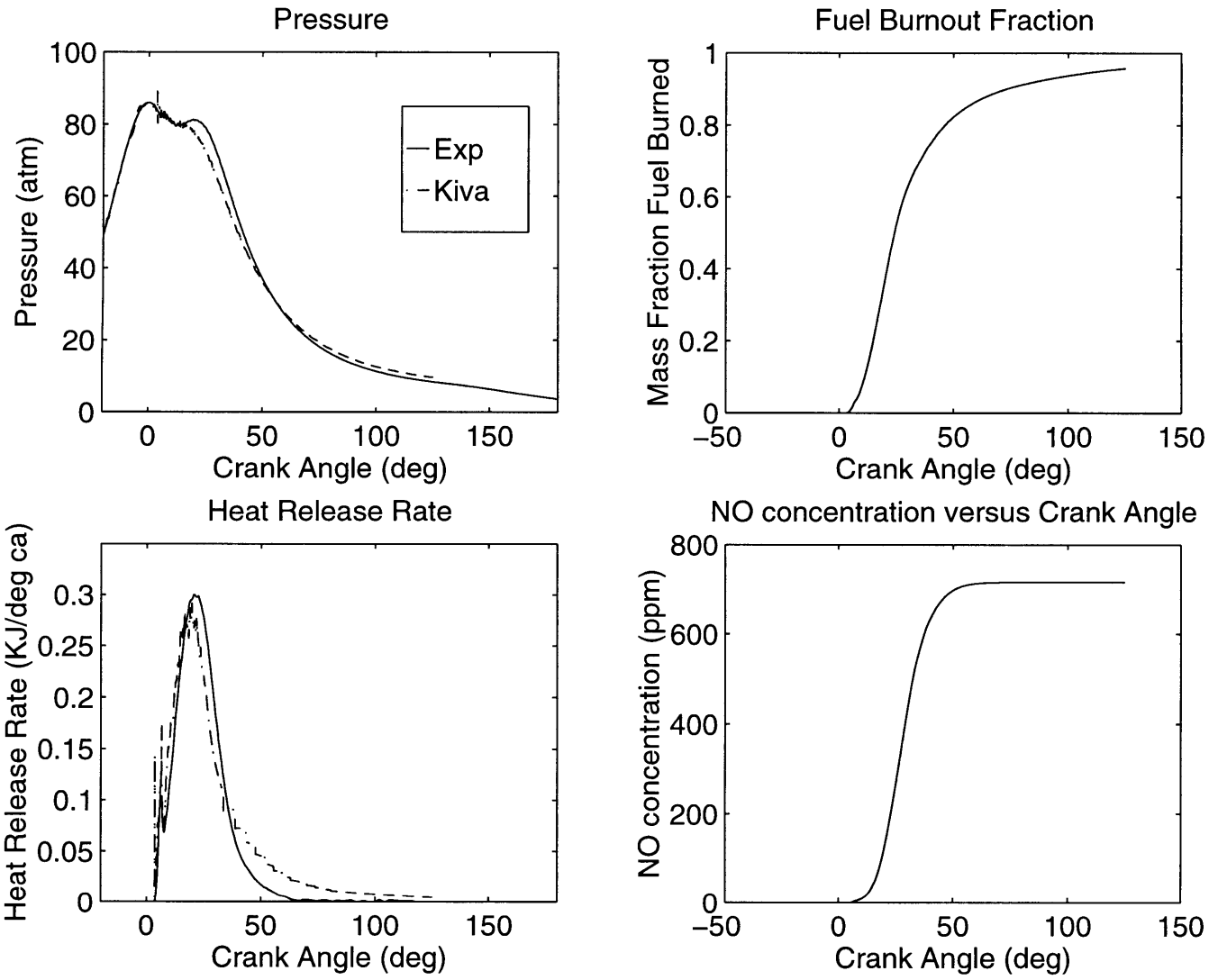

Figure 5-1: A comparison of Kiva and Experimental Results for Run2

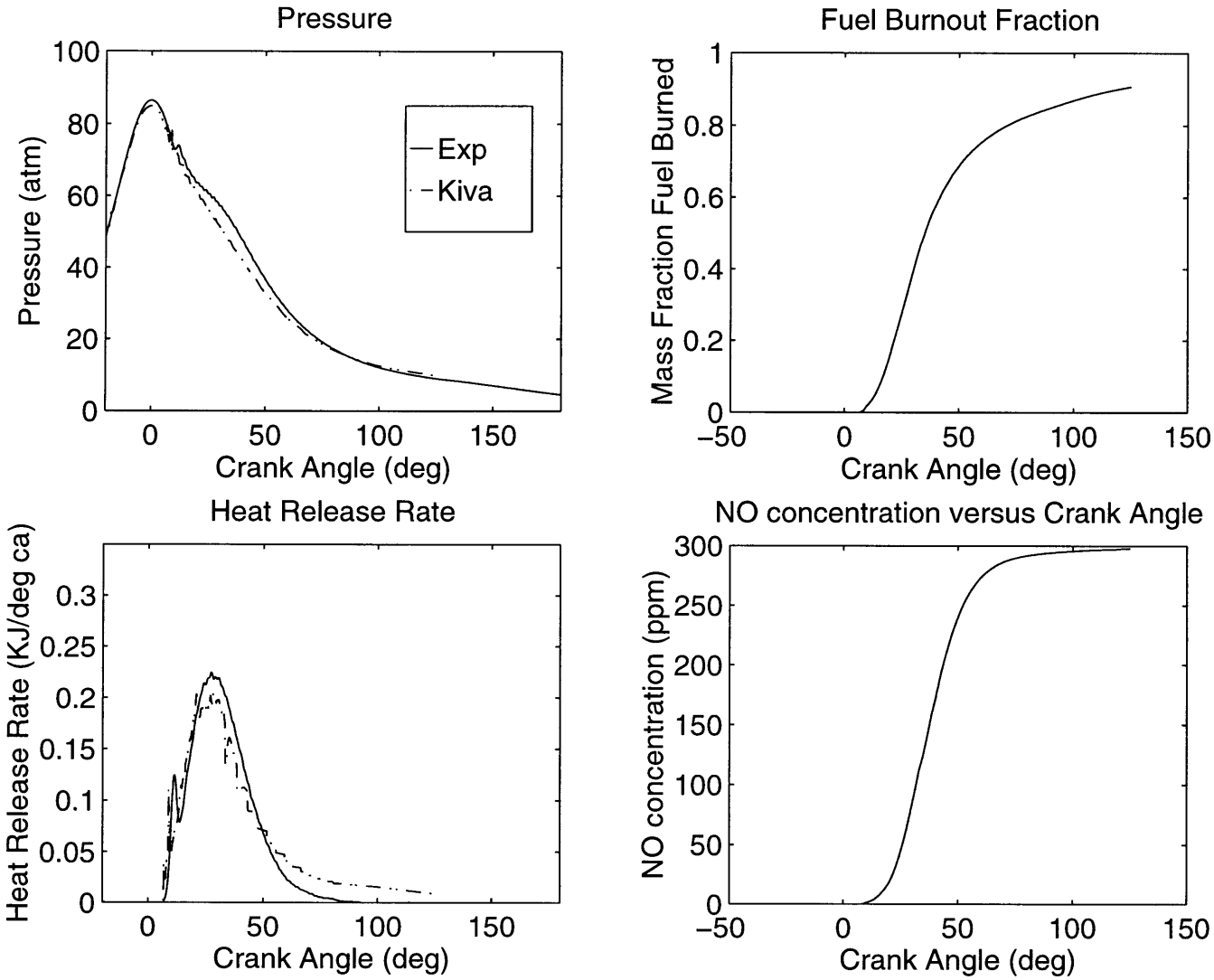

Figure 5-2: A comparison of Kiva and Experimental Results for Run3

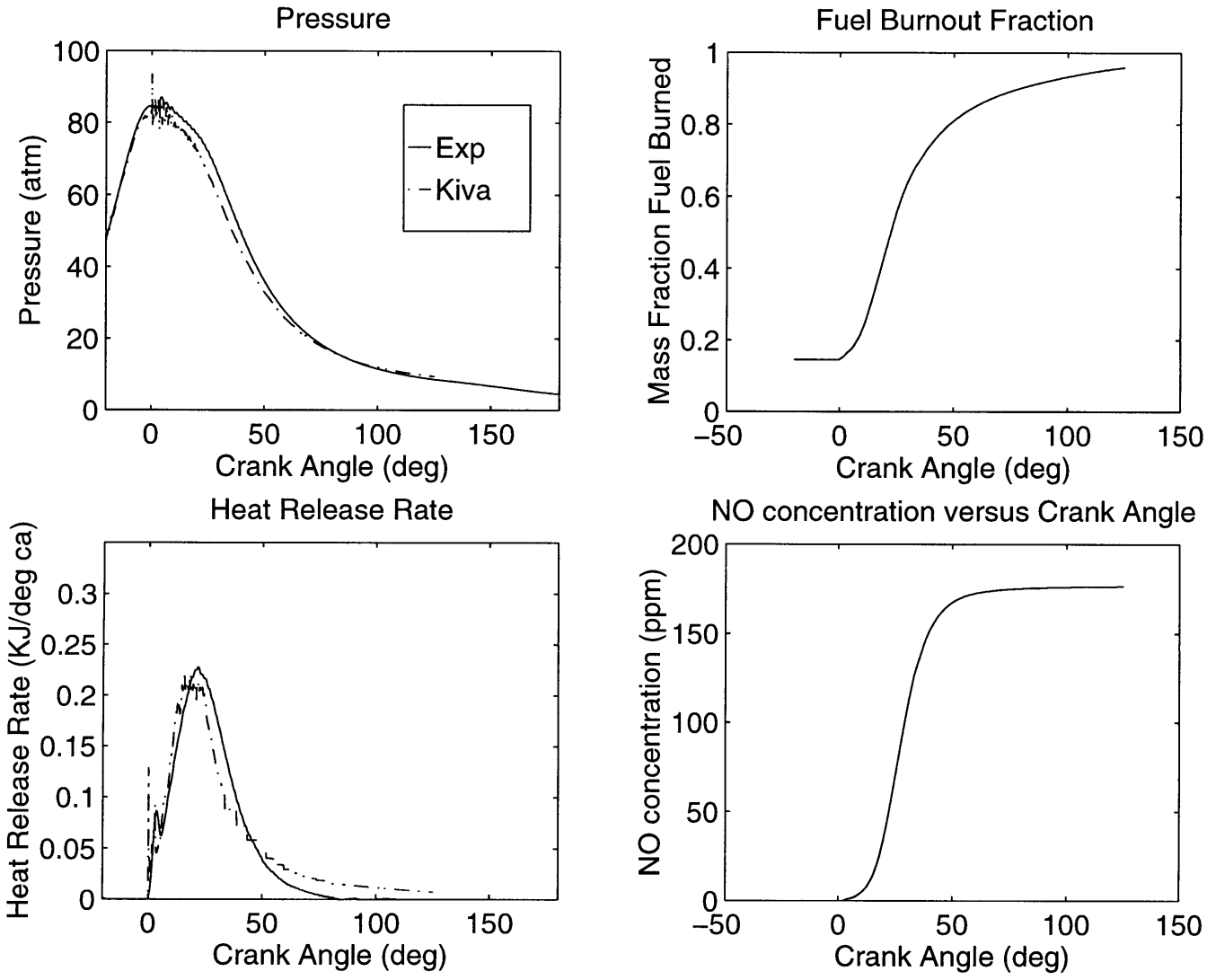

Figure 5-3: A comparison of Kiva and Experimental Results for Run4

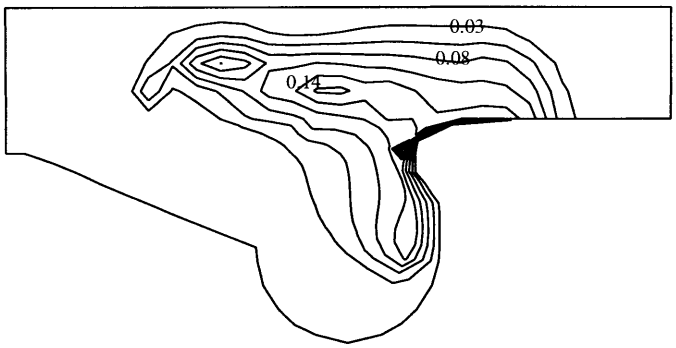

Contours of Fuel Mass Fraction

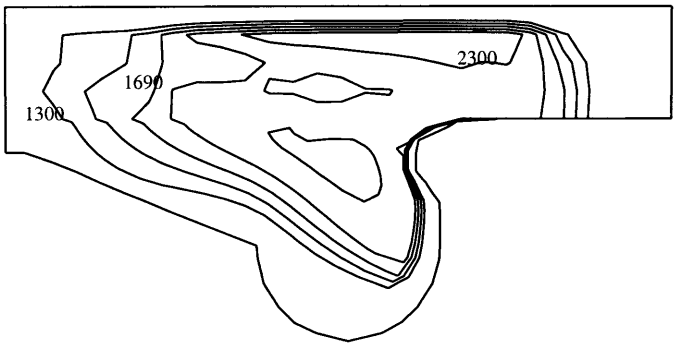

Contours of Temperature (Kelvin)

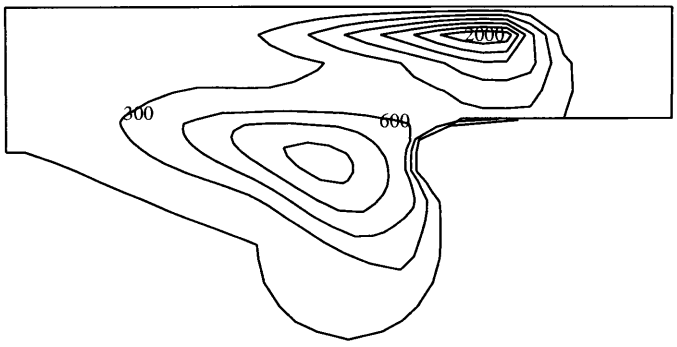

Contours of Excess NO mole fraction (ppm)

Figure 5-4: Fuel Mass Fraction, Temperature and Excess NO mole fraction contours at a crank angle of 23.4 degrees -Run2.

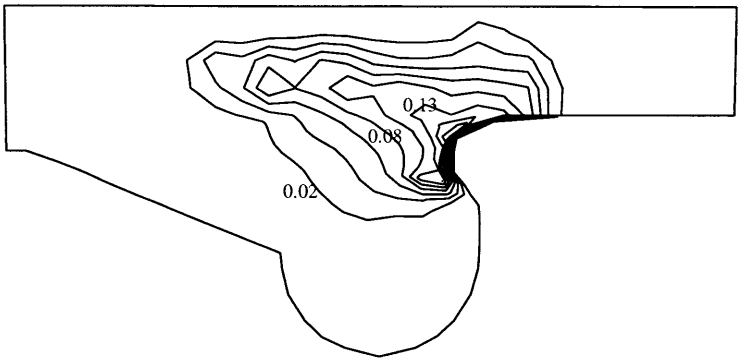

Contours of Fuel Mass Fraction

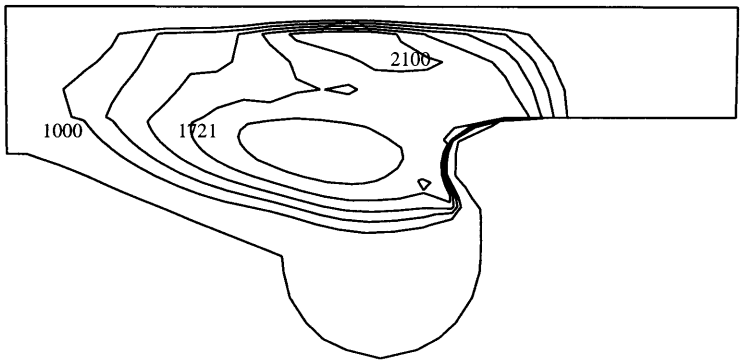

Contours of Fuel Mass Fraction

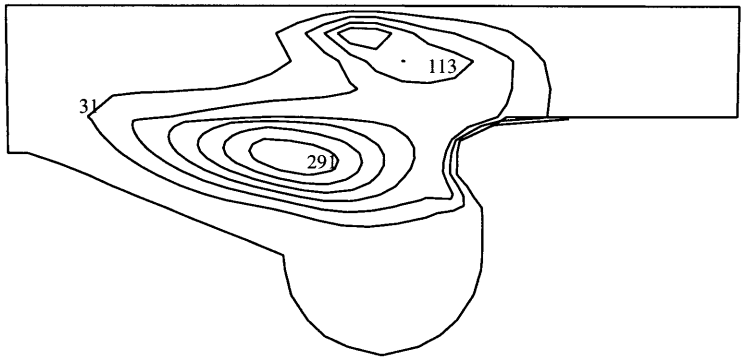

Contours of excess NO mole fraction (ppm)

Figure 5-5: Fuel Mass Fraction, Temperature and Excess NO mole fraction contours at a crank angle of 25.6 degrees -Run3.

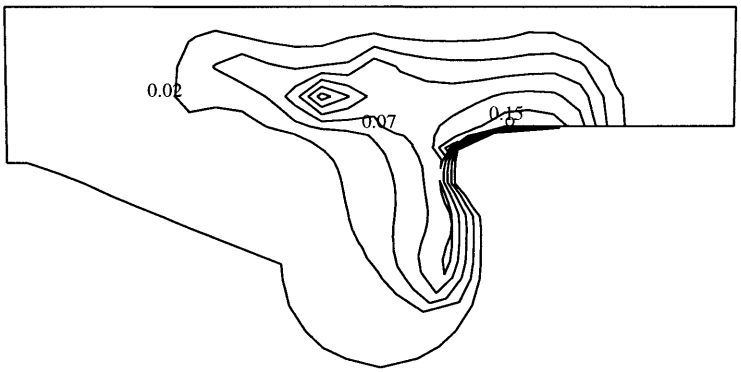

Contours of fuel mass fraction

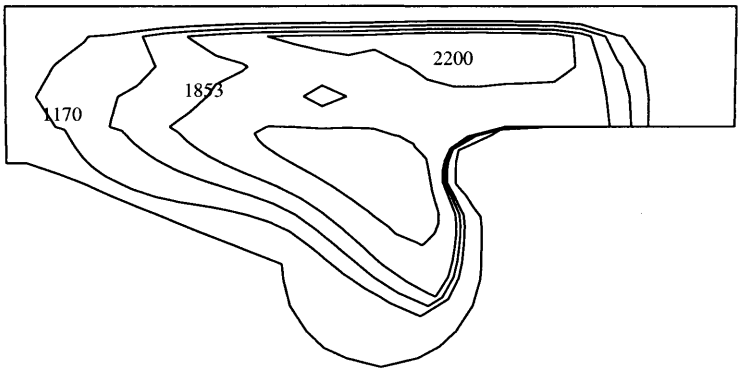

Contours of temperature (K)

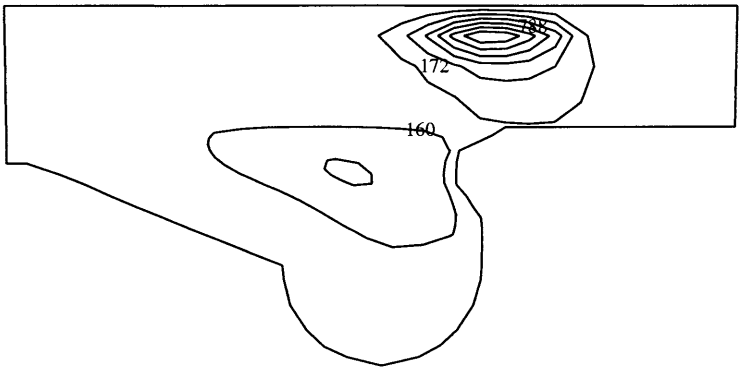

Contours of excess NO mole fraction (ppm)

Figure 5-6: Fuel Mass Fraction, Temperature and Excess NO mole fraction contours at a crank angle of 23 degrees -Run4.

5.2 Comparison of Experimental And Computed NO Exhaust Concentrations

Figure 5-7 shows the predicted and experimental values of exhaust NO concentrations for the four cases. The graph shown in the figure illustrates the relative contributions of the flame sheet and cell averaged NO formation routes to the total NO concentration in the charge. As can be seen in the plot (and as mentioned in the preceding chapter), the excess NO concentrations are typically an order of magnitude higher than those obtained by the consideration of cell averaged temperatures and species concentrations alone. It can also be seen in this figure that the agreement between the predictions and the experimental values is significantly improved by the addition of the flame sheet NO formation mechanism.

It has been typical practice in previous modeling studies to apply a multiplicative calibration factor to the Zeldovich formation rates in order to improve the agreement between experimental and modeling results of exhaust NO concentrations. Factors with values as high as 80 have been used [10] and as can be seen in Table 5.2, this is fairly consistent with the calibration factor that would be needed if bulk NO formation rates alone had been considered in this study. Table 5.2 also gives the ratio of the experimental and predicted values of exhaust NO concentrations obtained which is approximately 2.2 on the average. It is lower for the baseline case and higher for the latter cases. The change in the value of this ratio from case to case might indicate that the predicted gas temperatures are higher for the first case than subsequent cases when compared to the temperatures that obtain in the physical system at the corresponding operating conditions, and a comparison of the heat release rate curves for the four runs might lend credence to this supposition.

The effect of variations in the operating variables is shown more directly for both the predictions and experimental results in Figure 5-8. Though the magnitudes are incorrect, the flame sheet submodel predicts the correct trends in the variation of exhaust NO concentrations with changes in engine speed, injection timing and the recirculation of exhaust gases as can be seen in this figure.

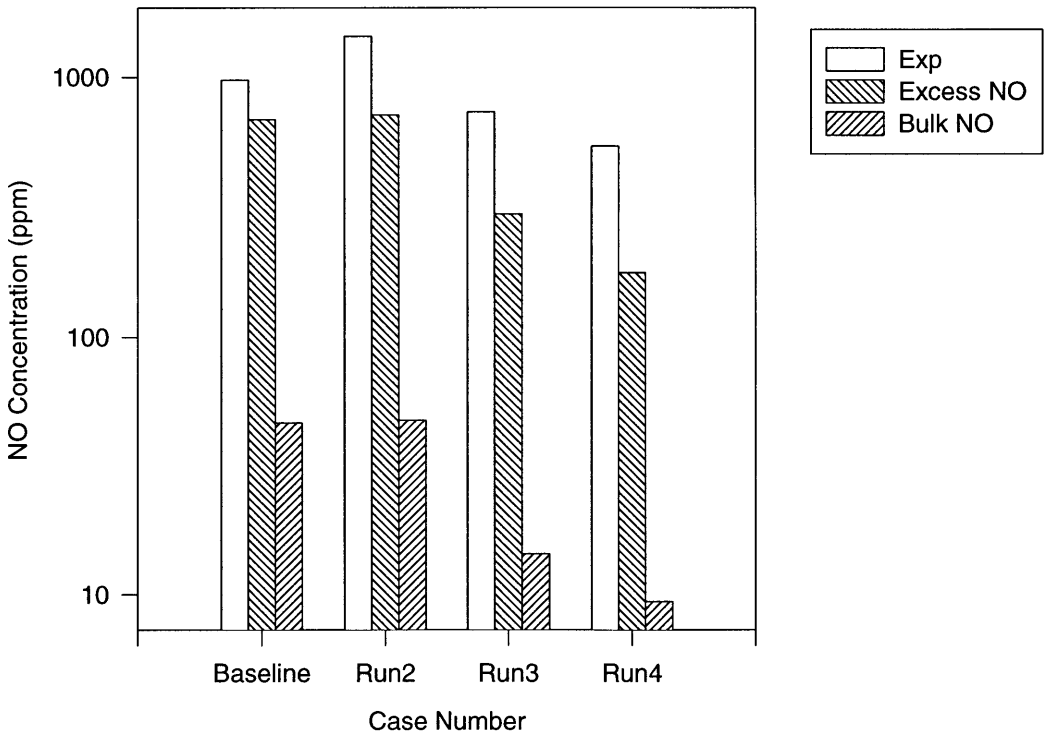

Figure 5-7: Predicted vs Experimental Values of Exhaust NO Concentration

Case Number	Experiment/Predicted	
	Bulk Only	Bulk+FlameSheet
Baseline	21	1.42
Run1	30	2.01
Run2	51	2.46
Run3	58	3.06

Table 5.2: Ratio of Predicted and Experimental Values of Exhaust NO concentration; Using (1)Cell Averaged Values Only and (2) Adding the Flame Sheet Contributions

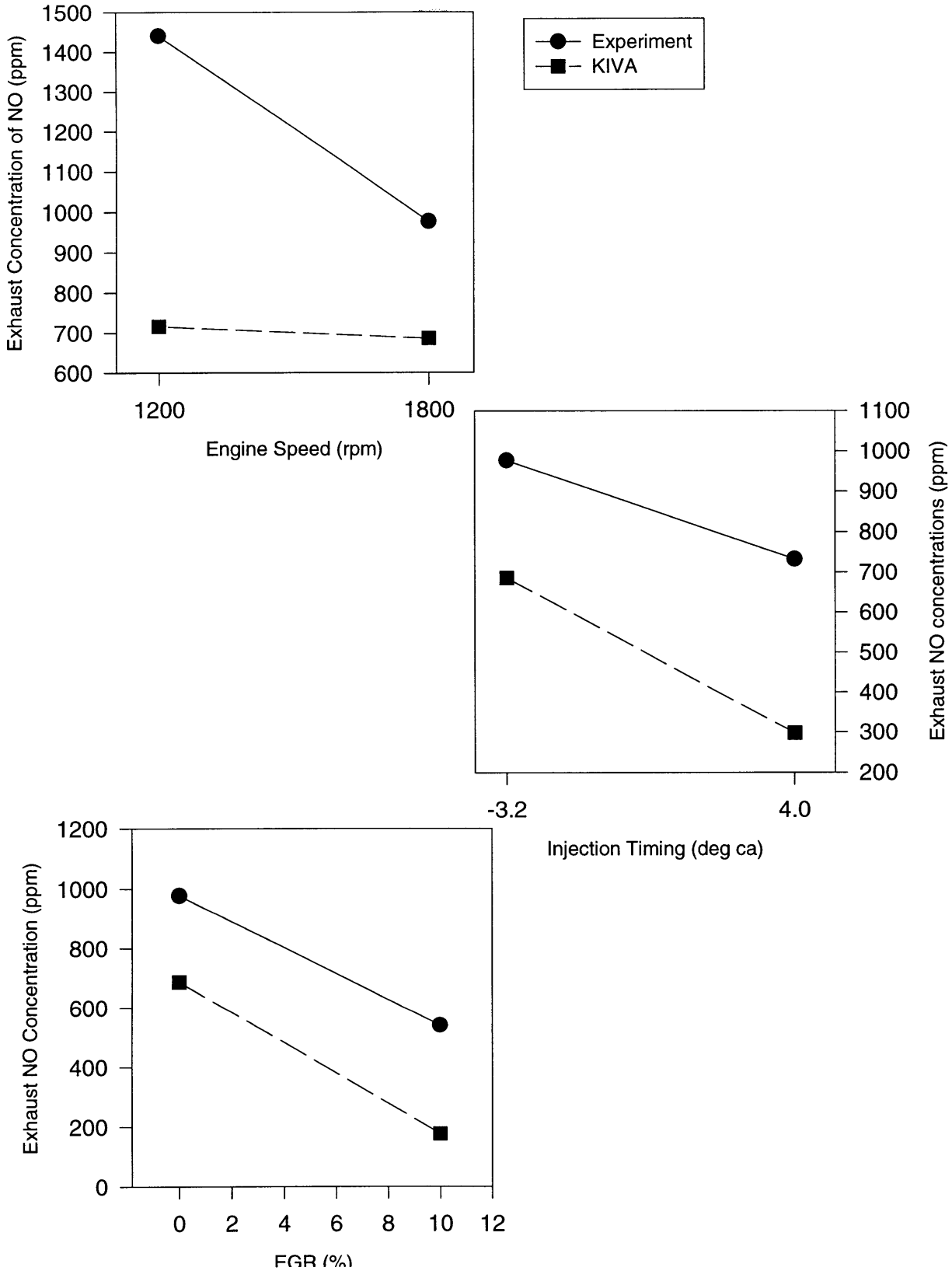

Figure 5-8: Variation of Exhaust *NO* Concentrations with Parameter Variations

5.3 Possible Routes of Additional NO Formation

Differences in the predicted and experimental values of exhaust NO concentrations presented in the preceding section suggest that other mechanisms of NO formation should be explored and their relative significance quantified. Two possible routes of additional NO formation are the prompt mechanism and the higher temperatures associated with the products of combustion.

The prompt NO mechanism involves the formation of NO via the reduction of molecular nitrogen according to the following reaction:

$$CH + N_2 \rightleftharpoons HCN + N \tag{5.1}$$

HCN produced in the above reaction is subsequently oxidized to form NO and N_2. Several experiments have been performed to characterize the formation of NO by this mechanism [32] and it is generally believed that the relative contributions of prompt NO are small in high-temperature, fuel-lean systems because the reactions involved are not as endothermic as those associated the Zeldovich mechanism and because of the necessity of the presence of hydrocarbon fragments for the reactions to proceed.

Dupont etal[33] determined a governing equation for the rate of prompt NO formation of the form

$$\frac{d[NO]_{pr}}{dt} = fAT^n[O_2][N_2][Fuel]exp(-E_a/RT) \tag{5.2}$$

where f is a correction factor for fuel concentration and fuel type given by the expression

$$f = 4.75 + 8.10 \times 10^{-2} n_c - 23.2\phi + 32\phi^2 - 12.2\phi^3 \tag{5.3}$$

n_c in the above equation is the number of carbon atoms per molecule of fuel and ϕ is the fuel equivalence ratio. Suggested values of activation energy for equation(5.2) are as follows:

$$E_a = 178KJ/mol; \quad T < 1920K \tag{5.4}$$

$$E_a = 303KJ/mol; \quad T > 1920 \tag{5.5}$$

The pre-exponential term A was given as $1.2 \times 10^7 (RT/P)^2$ for fuel lean flames.

The above expressions were used to obtain an estimate of the prompt NO formation for the four cases described previously. Cell averaged values of ϕ and fuel concentrations in the rich regions were used in the computations. The validity of rate equation under diesel engine combustion conditions might be questionable, but the results shown in Figure 5-9 confirm expectations that the contributions of the prompt mechanism to overall NO concentrations is small. It is also interesting to note that the relative significance of prompt NO increases as cylinder temperatures decrease as anticipated.

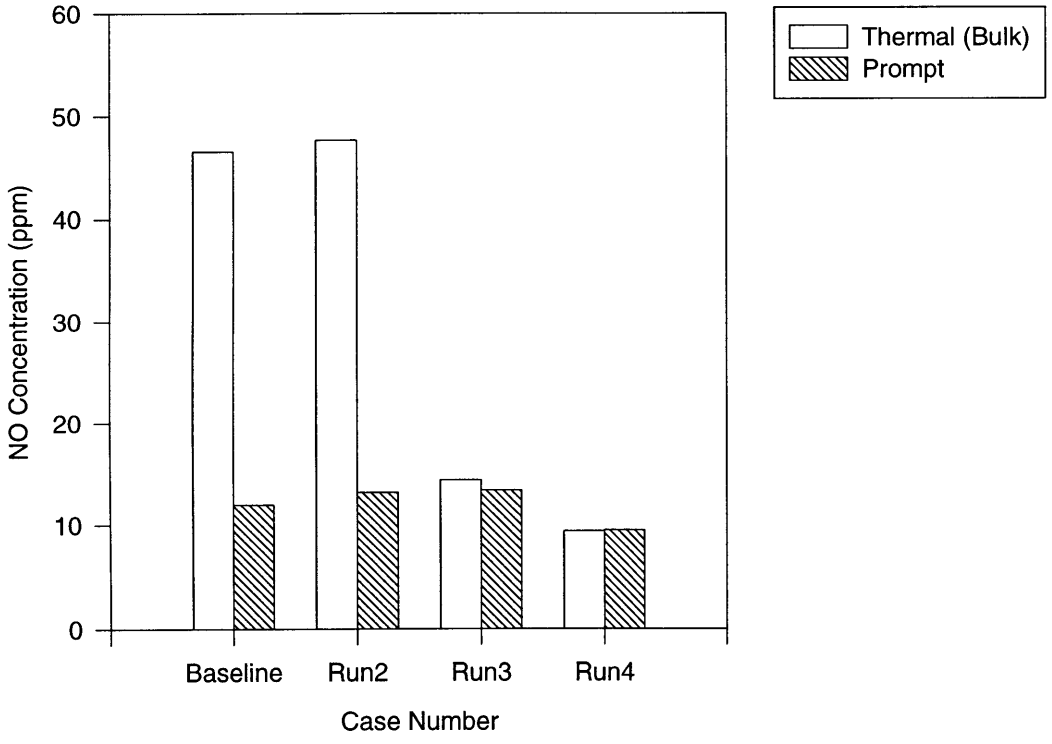

Figure 5-9: Relative Contribution of Prompt NO Mechanism

Faster rates of NO formation might also be obtained if the higher temperatures of the combustion products are taken into consideration. The current model of heat release in the KIVAII code assumes that the heat of combustion released at fuel consumption is instantaneously mixed in with the contents of the computational cell, thus providing a cell averaged temperature. The rate of mixing with the cell contents is, however, finite in reality and there should exist a period of time when the elevated temperatures in the products of combustion results in higher rates of formation of NO. The relative contributions of this mechanism becomes more significant with the number of computational cells having a mixture of burned and unburned gases. Defining R as the ratio of the mass of products to the sum of the mass of air and product species in the cell, the number of cells having values of R within certain ranges were determined for different crank angles. Figure 5-10 is a plot of the results that were obtained; the numbers on the abscissa represent the range of values contained by the preceding number and itself, i.e 0.2 represents the range 0.1-0.2. As can be seen in this figure, there is a significant degree of co-existence of the burned gas with the unburned charge. The NO concentrations that would result from the consideration of the unmixed burned gas temperatures were however not determined in the course of this study.

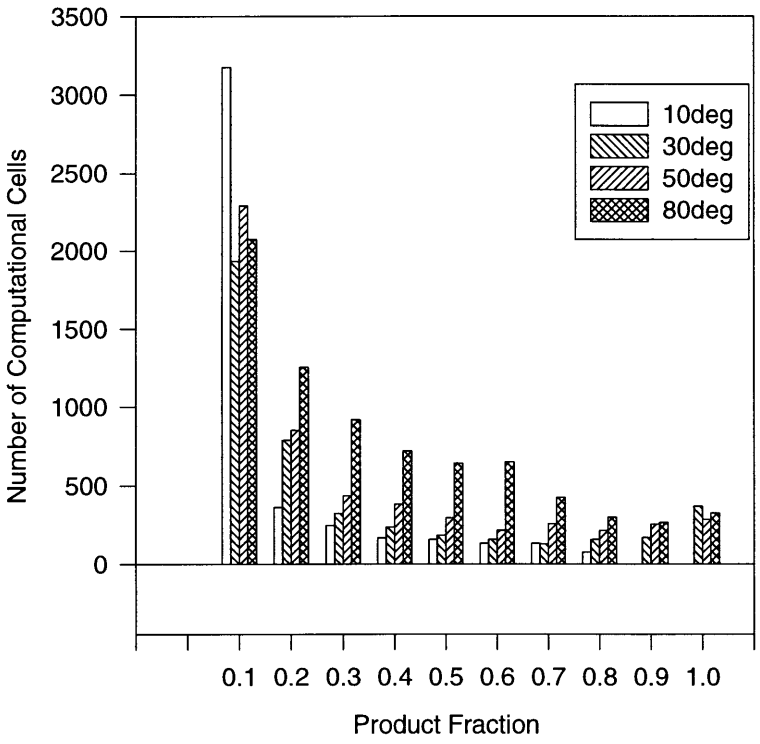

Figure 5-10: Histogram of the Number of Computational Cells Having Different Product Species Mass Fractions for Different Crank Angle Degrees

Chapter 6

CONCLUSIONS

The objectives of this study could be summarized as follows: the development of a model of combustion and NO formation in a flame sheet; the subsequent formulation of a flame sheet library as a combustion submodel for the KIVAII code; the implementation and testing of the model and the demonstration of trends in NO formation rates with engine operating characteristics using modeling results.

This research effort was largely successful in achieving these goals. A model of the combustion process in flame sheets was formulated. This model allowed for the determination of temperatures and species concentration profiles within the flame sheet. With this information, the formation rates of NO in the reaction sheet were subsequently determined.

Variations in the model inputs provided information on the behavior of the rates of fuel consumption and NO formation with changes in input parameters. The knowledge developed in this parametric study enabled the formulation of a flame sheet library appropriate for use in the KIVAII code. The model parts of this library were demonstrated to capture the essential trends in species formation and destruction rates observed in the results of the flame sheet computations. At the same time, however, the formulation chosen for this library was such as would add little complexity to the structure of the KIVAII code. Thus, with this approach, significantly greater detail was added to the modeling procedure while incurring minimal penalty in model performance.

The flame sheet library was successfully incorporated into the KIVA code as a combustion submodel. Testing of the model was performed on the basis of experimental data obtained from a Cummins N14 engine operated at four different conditions. Comparison of the modeling and experimental results of heat release rates and cylinder pressure traces indicated good model performance in the predictions of the progress of combustion for the four cases. Examination of the model predictions also highlighted the importance of the role of the fuel spray in the enhancement of the mixing of fuel and air species and hence on the promotion of the combustion process.

NO formation rates in the flame sheet were found to be at least an order of magnitude greater than that formed by consideration of cell averaged temperatures and species concentrations alone. The model predictions were compared with experimentally determined exhaust concentrations of NO and agreement between experiment and model results were significantly improved with the added consideration of flame sheet contributions. In particular, the ratio of the experimental to predicted values of NO concentration in the exhaust was reduced from an average value of 40 to 2.2 when flame sheet contributions were considered. This result underscores the importance of subgrid effects on the accurate determination of NO formation rates during combustion. Other possible mechanisms of additional NO formation were also considered. The prompt NO mechanism is a possible route, but it was demonstrated that the relative contributions of prompt NO is small.

Possibilities of further work along these lines lie in the accurate determination of in-cylinder temperatures during the combustion process. As mentioned in the body of this thesis, the sensitivity of NO formation rates to small changes in temperature makes the accurate determination of the temperature field imperative. Experimental verification of predicted temperatures will remove a significant uncertainty in the modeling of NO formation rates.

Furthermore, the possibility of increased formation rates resulting from higher temperatures of the product gases prior to mixing-in with the rest of the charge was also suggested in the body of this thesis. This is another subgrid effect that is at yet not captured by the KIVAII code. A model could be created which would

incorporate this effect and its relative contributions to overall NO formation levels could be quantified.

Appendix A

Determination of gas properties

In solving the flame sheet equations, gas properties were computed for each grid point on the basis of temperature, pressure and species mass fractions. Thus the functional dependence of the properties on these variables had to be determined.

The c_p's for the different species can be written as follows[34]:

$$N_2 : c_p = 3.34 + 5.88 \times 10^{-2} \left(\frac{T}{100}\right) + 5.86 \times 10^{-5} \left(\frac{T}{100}\right)^2 - 2.63 \times 10^{-5} \left(\frac{T}{100}\right)^3 \quad \text{(A.1)}$$

$$H_2O : c_p = 3.74 + 1.13 \times 10^{-1} \left(\frac{T}{100}\right) + 1.49 \times 10^{-3} \left(\frac{T}{100}\right)^2 - 7.27 \times 10^{-5} \left(\frac{T}{100}\right)^3 \quad \text{(A.2)}$$

$$CO_2 : c_p = 3.1 + 5.46 \times 10^{-1} \left(\frac{T}{100}\right) - 2.37 \times 10^{-2} \left(\frac{T}{100}\right)^2 + 3.46 \times 10^{-4} \left(\frac{T}{100}\right)^3 \quad \text{(A.3)}$$

air: $$c_p = 3.312 + 7.31 \times 10^{-2} \left(\frac{T}{100}\right) - 1.085 \times 10^{-3} \left(\frac{T}{100}\right)^2 \quad \text{(A.4)}$$

fuel (dodecane): $$c_p = 173.43 + 1.69 \times 10^3 \ln \left(\frac{T}{100}\right) \quad \text{(A.5)}$$

Temperature in the above equations is in Kelvin units while the specific heats are in $J/kg/K$. Detailed information on the properties of complex fuels like diesel is generally unavailable and those of simpler species have to be used as a substitute. Thus the specific heat of dodecane was used in equation (A.5) above. The specific heat of the products is obtained from the sum of its constituents in stoichiometric

proportions i.e

$$c_{p_{prod}} = 0.193c_{p_{CO_2}} + 0.058c_{p_{H_2O}} + 0.72c_{p_{N_2}} \tag{A.6}$$

The species enthalpies (in J/kg) were written as functions of temperature as follows(again using dodecane as fuel):

$$CO_2: \quad \frac{R}{M}\left[3.1T + 2.7 \times 10^{-3}T^2 - 7.9 \times 10^{-7}T^3 + 8.7 \times 10^{-11}T^4\right] \tag{A.7}$$

$$H_2O: \quad \frac{R}{M}\left[3.74T + 5.66 \times 10^{-4}T^2 + 4.95 \times 10^{-8}T^3 - 1.82 \times 10^{-11}T^4\right] \tag{A.8}$$

$$N_2: \quad \frac{R}{M}\left[3.34T + 2.94 \times 10^{-4}T^2 + 1.95 \times 10^{-9}T^3 - 6.6 \times 10^{-12}T^4\right] \tag{A.9}$$

$$\text{air}: \quad \frac{R}{M}\left[3.3T + 7.3 \times 10^{-4}\frac{T^2}{2} - 1.1 \times 10^{-7}\frac{T^3}{3}\right] \tag{A.10}$$

$$\text{fuel}: \quad 3.14 \times 10^5 - 9.65 \times 10^3 T + 1.69 \times 10^3 T \ln T \tag{A.11}$$

R is the universal gas constant ($8314J/kmol/K$). T is in Kelvin. Thermal conductivities of individual species were also written in a similar fashion[34]:

$$\text{air}: \lambda = 6.5 \times 10^{-3} + 7.4 \times 10^{-5}\text{T} - 2.3 \times 10^{-8}\text{T}^2 + 7.7 \times 10^{-12}\text{T}^3 \tag{A.12}$$

$$N_2: \lambda = 6.8 \times 10^{-3} + 7.2 \times 10^{-5}T - 2.3 \times 10^{-8}T^2 + 7.8 \times 10^{-12}T^3 \tag{A.13}$$

$$CO_2: \lambda = -4.6 \times 10^{-3} + 8.7 \times 10^{-5}T - 2.7 \times 10^{-8}T^2 + 8.2 \times 10^{-12}T^3 \tag{A.14}$$

$$H_2O: \lambda = -6.9 \times 10^{-3} + 8.7 \times 10^{-5}T - 8.7 \times 10^{-10}T^2 + 6.4 \times 10^{-12}T^3 \tag{A.15}$$

T is in Kelvin and λ is in $W/m/K$. Again, the thermal conductivity of diesel is not known and the following expression (for Benzene) was used as a substitute:

$$\lambda = 0.0226\left(\frac{T}{433}\right)^{1.786} \tag{A.16}$$

Finally, the thermal conductivity of products was obtained by calculating the weighted average of the conductivity of its constituents. This is not rigorously correct, but it was noted that the values of thermal conductivity did not vary greatly for different species and hence the real system should be well approximated by the average values.

The binary diffusivity is known to have the following relational dependence[35]:

$$D_{ab} = D_{ab_{ref}} \frac{T/T_{ref}}{P/P_{ref}} \tag{A.17}$$

$D_{ab_{ref}}$ for air in products was chosen as $1.42 \times 10^{-5}\text{m}^2/\text{sec}$ at a T_{ref} of 276.2K and a P_{ref} of 1 atm corresponding to the binary diffusion of air in CO_2 for want of information on more appropriate values. For the fuel side of the flame sheet a value of $1.02 \times 10^{-5}\text{m}^2/\text{sec}$ (corresponding to the binary diffusion co-efficient of nitrogen in benzene) was used. T_{ref} and P_{ref} in this case were 311.3K and 1 atm respectively.

References

[1] S.H Mansouri, J.B Heywood, and K Radhakrishnan. Divided-chamber diesel engine, part 1: A cycle-simulation which predicts performance and emissions. SAE Technical Paper 820273.

[2] B Xiaoping, H Shu, Z Dai, S Yin, and C Duan. A multi-zone model for prediction of DI diesel engine combustion and soot emission. SAE Technical Paper 941900.

[3] A.J Brown and J.B Heywood. A fundamentally based stochastic mixing model for predicting NO and soot emissions from direct-injection diesel engines. *Calculations of Turbulent Reactive Flows, Winter Annual Meeting of the American Society of Mechanical Engineers*, 81:293–312, 1986.

[4] M Ikegami and Masahiro S. A stochastic model of an unsteady turbulent diffusion flame in a confined space. Bulletin of the JSME Vol.23, No. 186, 1980.

[5] W.T Lyn. Study of burning rate and nature of combustion in diesel engines. *9th Symposium (International) on Combustion*, pages 1069–1082, 1962.

[6] Heywood. *Internal Combustion Engine Fundamentals*, chapter 10. McGraw-Hill Publishers, 1988.

[7] T. Kamimoto and H. Kobayashi. Combustion processes in diesel engines. *Prog. in Energy and Combustion Science*, pages 163–189, 1991.

[8] T. Kamimoto, Y.J. Chang, and H. Kobayashi. Rate of heat release and its prediction of a diesel flame in a rapid compression machine. SAE Technical Paper 841076.

[9] Wolf Bauer. A three dimensional diesel combustion model. Master's thesis, Technische Universitat Karlsruhe, 1992.

[10] R.D. Reitz and C.J. Rutland. Development and testing of diesel engine CFD models. *Prog. in Energy and Combustion Science*, pages 173–196, 1996.

[11] D M. A Gonzales, Z.W. Lian, and R.D. Reitz. Modeling of diesel engine spray vaporization and combustion. SAE Technical Paper 920579.

[12] C.J. Rutland et al. Towards predictive modeling of diesel engine intake flow, combustion and emissions. SAE Technical Paper 941897.

[13] G.F. Carrier, F.E. Fendell, and F.E. Marble. The effect of strain rate on diffusion flames. *SIAM Journal of Applied Mathematics*, 28:463–500, 1975.

[14] N. Peters. Laminar flamelet concepts in turbulent combustion. *21st Symposium (International) on Combustion*, pages 1231–1250, 1986.

[15] W.K. Cheng. Calculation of turbulent diffusion flame using a coherent flame sheet model. *AIAA*, 83-1322, 1983.

[16] B. Dillies, K. Marx, and C. Dec, J.and.Espey. Diesel engine combustion modeling using the coherent flame model in Kiva-II. SAE Technical Paper 930074.

[17] D. Veynante, F. Lacal, and S.M. Candal. A new flamelet combustion model combining premixed and non-premixed turbulent flames. AIAA paper 89-0487, 1989.

[18] R.W. Bilger. The structure of turbulent non-premixed flames. *The Twenty Second Sysposium (International) on Combustion*, page 1231, 1986.

[19] M.A. Patterson, S.-C. Kong, G.J. Hampson, and R.D. Reitz. Modeling the effects of fuel injection characteristics on diesel engine soot and NO_x emissions.

[20] C.F. Edwards, D.L. Siebers, and D.H Hoskin. A study of the autoignition process of a diesel spray via high speed visualization. SAE Technical Paper 920108.

[21] B.F. Magnussen and B.H. Hjertager. On mathematical modeling of turbulent combustion with special emphasis on soot formation and combustion. *16th Symposium (International) on Combustion*, pages 719–729, 1976.

[22] M.P. Musculus and C.J. Rutland. An application of the coherent flamelet model to diesel engine combustion. SAE Technical Paper 950281.

[23] H.G. Im, C.K. Law, J.S. Sim, and F.A. Williams. Response of counterflow diffusion flames to oscillating strain rates. *Combustion and Flame*, pages 21–30, 1995.

[24] A.F. Ghoniem, M.C. Soteriou, and O.M. Knio. Effect of steady and periodic strain on unsteady flamelet combustion. *24th Symposium (International) on Combustion*, 1992.

[25] Heywood. *Internal Combustion Engine Fundamentals*, chapter 9. McGraw-Hill Publishers, 1988.

[26] J.A. Miller and C.T. Bowman. Mechanism and modeling of nitrogen chemistry in combustion. *Prog. in Energy and Combustion Science*, pages 287–338, 1989.

[27] R.S. Turns. Understanding NO_x formation in nonpremixed flames: Experiment and modeling. *Prog. in Energy and Combustion Science*, pages 361–385, 1995.

[28] Heywood. *Internal Combustion Engine Fundamentals*, chapter 11. McGraw-Hill Publishers, 1988.

[29] D.A. Anderson, J.C. Tannehill, and R.H Pletcher. *Computational Fluid Mechanics and Heat Transfer.* Hemisphere Publishing Corporation, 1984.

[30] C. Hirsch. *Numerical Computation of Internal and External Flows.* John Wiley and Sons, 1988.

[31] A.A. Amsden, P.J. O'Rouke, and T.D Butler. KIVA-II: A computer program for chemically reactive flows with spray. Report LA-11560-MS, Los Alamos National Laboratory, 1989.

[32] F. Bachmaier, K.H. Eberius, and Th. Just. The formation of nitric oxide and the detection of HCN in premixed hydrocarbon-air flames at 1 atmosphere. *Combustion Science and Technology*, 1973.

[33] V. Dupont, M. Pourkashanian, and A. Williams. Modeling of process heaters fired by natural gas. *Journal of the Institute of Fuel*, 1992.

[34] J.H Lienhard. *A Heat Transfer Textbook.* Prentice-Hall Inc., 1987.

[35] R.C. Reid, J.M. Prausnitz, and T.K Sherwood. *Properties of Gases and Liquids.* McGraw-Hill, 1977.